May 2021

Generation and Manipulation of Higher Order Fractional and Integer Bessel Gaussian Beams

Wenzhe Li
Clemson University, WENZHEL@G.CLEMSON.EDU

GENERATION AND MANIPULATION OF HIGHER ORDER FRACTIONAL AND INTEGER BESSEL GAUSSIAN BEAMS

A Dissertation
Presented to
the Graduate School of
Clemson University

In Partial Fulfillment
of the Requirements for the Degree
Doctor of Philosophy
Photonics Science and Technology

---

by
Wenzhe Li
May 2021

Accepted by:
Dr. Eric G. Johnson, Committee Chair
Dr. Richard J. Watkins
Dr. Hai Xiao
Dr. Lin Zhu

ABSTRACT

Optical orbital angular momentum (OAM) describes orbiting photons, swirling local wave vectors, or spiraling phase distribution depending on what theory we use to explain light. If we consider light as a propagating electromagnetic wave, then light has the freedoms of frequency, magnitude, phase, and polarization. For a monochromatic light, expanding the later three freedoms spatiotemporally, numerous optical modes are solved from Maxwell's equations and boundary conditions. OAM mode study starts from integer charge because it is in the integer form of the fundamental phase singularity structure. Fractional OAM mode is the Fourier series of integer OAM modes. The average OAM does not conserve along with propagation for the traditional fractional OAM modes. We propose a new asymmetric fractional Bessel Gaussian mode providing the average OAM conserving along with the propagation.

To better understand the fractional OAM mode or integer OAM mode combination, we study the novel concentric vortex optics. The analytical propagation expression of the concentric vortex beam is derived and analyzed. The concentric vortex beam is essentially the OAM spectrum, with only two integer OAM components. The spectrum coefficiencies are real numbers and approximately power equalized in general cases. The concentric vortex beam is the coherent combination of incomplete Kummer beams. As the inner aperture tuning large, the beam evolves into the Kummer beam with the inner charge number. The aperture decreases, the outer charges Kummer beam dominates.

The proposed asymmetric fractional Bessel Gaussian beam's Fourier transform is azimuthal Gaussian perfect vortex. We use log-polar coordinate mapping diffractive optics

to transform the elliptical Gaussian beam into the desired azimuthal Gaussian perfect vortex beam. The generated asymmetric fractional Bessel Gaussian beam is systematically compared with Kotlyar's asymmetric Bessel Gaussian beam. It's found that the proposed beam has a narrower OAM spectrum, preserving average fractional OAM. Furthermore, the log-polar transform's inherent output lateral shifting problem is addressed for the first time to our knowledge. An improved log-polar design is proposed, and we use five critical metrics to show the new log-polar generated asymmetric Bessel Gaussian beam's quality is much improved.

The manipulation of the high order asymmetric fractional Bessel Gaussian beam is critical to applications scaling from communication, sensing, filamentation, to micromanipulation. We propose and demonstrate acousto-optical deflector (AOD) HOBBIT (Higher Order Bessel Beams Integrated in Time) system. The system can continuously tune the OAM modes on the order of 400 kHz. This speed beats the fastest spatial light modulator (SLM), and even better, the proposed system could work for high power applications.

DEDICATION

To my wife, parents, grandparents, and my dear daughter.

ACKNOWLEDGMENTS

I would like to thank my advisor Dr. Eric Johnson, for the knowledge he teaches me, the research opportunity he offers me, the advice he suggests to me, the fabulous photonics world he opens for me, the path he leads me, and the great patience he has with me. This dissertation cannot be complete without your advice and help.

I want to thank my committee members Dr. Richard Watkins, Dr. Hai Xiao, and Dr. Lin Zhu, for their valuable time and advice.

I would like to thank Dr. Keith J. Mill for his help in the lab experiment and inspiring discussions. I would like to thank Bill Delaney for his help in cleanroom fabrication. I want to thank Dr. Aaron Pung, Dr. Yuan Li, Dr. Indumathi Raghu Srimathi, Kunjian Dai, Caitie O'Donnell, Justin Free, and all the other Micro-Photonics Laboratory researchers that I have come across the seven years of research life. I want to thank Dr. Kaitlyn Morgan, who has the most overlapping doctorial journey with me in this group.

Finally, I want to thank my wife, Dr. Liwei Hua, for her love, support, and sacrifice. I want to thank my parents, in-laws, and grandparents. I was supposed to go back to see you, grandma. I miss you.

TABLE OF CONTENTS

Page

TITLE PAGE i

ABSTRACT ii

DEDICATION iv

ACKNOWLEDGMENTS v

LIST OF TABLES ix

LIST OF FIGURES x

LIST OF ACRONYMS xv

CHAPTER

I. INTRODUCTION 1

1.1 General overview 1
1.2 Diffractive optics 2
1.3 Log-polar optics and asymmetric fractional Bessel Gaussian beam 3
1.4 Motivation and peer works 4
1.5 Dissertation outline 4

II. CONCENTRIC SPIRAL PHASE PLATE 8

2.1 Introduction 8
2.2 Multiple harmonic binary diffractive SPP 10
2.3 Gaussian beam through an SPP 15
2.4 Diffraction theory of multiple harmonic concentric SPP 17
2.5 Gouy phase caused rotation 20
2.6 Device fabrication and experimental characterization 21
2.7 Discussion 24
2.8 Conclusion 26

III. FRACTIONAL OAM AND ASYMMETRIC BESSEL GAUSS BEAM 29

3.1 Introduction 29

Table of Contents (Continued)

Page

3.2 Plane-wave go through SPP to generate fractional OAM 31
3.3 Gaussian go through SPP to generate fractional OAM 34
3.4 Total singularity strength 36
3.5 OAM spectrum and asymmetric fractional Bessel Gaussian beam . 41
3.6 Comparison of the asymmetric Bessel Gaussian beams 46
3.7 Contribution summary 56

IV. NEW LOG-POLAR DESIGN 58

4.1 Introduction 58
4.2 General optical geometric transformation 59
4.3 Paraxial optical log-polar geometric transformation 62
4.4 Conventional log-polar design's dilemma and five evaluation metrics 66
4 5 Non-paraxial log-polar transform and the new design 73
4.6 Contribution summary 82

V. COLLIMATOR/FIBER ARRAY HOBBIT 83

5.1 Introduction 83
5.2 1550 nm fiber array HOBBIT 86
5.3 Collimator array higher-order fractional HOBBIT generation 94
5.4 Contribution summary 95

VI. AOD HOBBIT SYSTEM 97

6.1 Introduction 97
6.2 Method 99
6.3 Diffractive phase-only optics 109
6.4 Experimental setup and results 110
6.5 Conclusion 114
6.6 Contribution summary 115

VII. CONCLUSION AND FUTURE WORK 116

7.1 Conclusion 116
7.2 Future work 119
7.3 Major contributions 120

APPENDICES 123

Table of Contents (Continued)

Page

A: PUBLICATION LIST 124

REFERENCES 130

LIST OF TABLES

Table Page

4.1 Five metrics of old log-polar optics design 81

4.2 Five metrics of new log-polar optics design 81

LIST OF FIGURES

Figure Page

2.1 A concentric SPP diffracts a Gaussian beam into a petal-like pattern..... 8

2.2 A 16 levels charge 2 SPP's phase profile. The $\alpha 2\pi$ phase is corresponding with an arbitrary wavelength..... 11

2.3 The $N = 16$ levels $\left|m_{\lambda_0}\right| = 2$ SPPs' wavelength-dependent diffraction efficiency $\left|A_n\right|^2$.(a) The first four harmonic charge 2, 4, 6, 8, (b) the corresponding 16 levels binary SPP. 13

2.4 The simulated phase profile of multiple harmonic concentric SPP, the inner and outer SPP's radius are ρ_{in} and ρ_{out}, respectively. 14

2.5 Far-field intensity of concentric SPP beam with charge $m_{in} = 1$, $m_{out} = -2$ (a) analytical expression and (b) RS propagation method 20

2.6 Microscope image of the fabricated multiple harmonic concentric SPP optic. 22

2.7 The experimental setup to multiplex the 2090 nm and 1064 nm lasers through a single concentric vortex phase plate. The imaging lens helps the infrared camera catch the diffracted patterns at different z location after the Fourier lens 22

2.8 The simulated and experimental petal-like patterns of 2090 nm and 1064 nm at 107 mm, 157 mm, 209 mm, 259 mm, and 308 mm after the Fourier lens. 24

2.9 The simulated multi-harmonic lens (left column), concentric vortex (central column), and the combination phase (right column). Phase profile for 2090 nm (a) lens, (b) concentric vortex with $m_{in} = 1$, $m_{out} = -2$, and (c) the combination of (a) and (b). Phase profile for 1064 nm (d) lens, (e) concentric vortex with $m_{in} = 2$, $m_{out} = -4$, and (f) the combination of (d) and (e). 25

2.10 The iso-surface of the intensity profile in 3-dimensions of both the 2090 nm beam and the 1064 nm beam, using the phase profile in Fig. 9 (c) and (f), respectively..... 26

List of Figures (Continued)

Figure Page

3.1 A fractional vortex plane wave and fractional vortex Gaussian beams' average OAM are compared with the linear relationship. 40

3.2 Azimuthal Gaussian ring beams' (a) intensity and (b) fractional OAM phase. The red arrow indicates the azimuthal phase discontinuity. 42

3.3 Average OAM of vortex plane wave (red dash line), vortex HyGG (yellow dash line), and asymmetric Bessel Gaussian beam (solid purple line). 45

3.4 (a), (d), (g) Intensity, (b), (e), (h) phase, and (c), (f), (i) normalized OAM spectrum coefficients from the Eq. 3.33 $U_{\mathrm{aBG\_K}}\left(r,\theta,z=0;c\right)$ at n = 3, and different asymmetric degree c: (a), (b), (c) 0.1; (d), (e), (f).1; and (g), (h), (i) 10. 49

3.5 (a), (d), (g), (j), (m) Intensity, (b), (e), (h), (k), (n) phase, and (c), (f), (i), (l), (o) normalized OAM spectrum coefficients from the Eq. 3.35 $U_{\mathrm{aBG\_GR}}\left(r,\theta,z=0;\beta\right)$ at n = 3, and different asymmetric degree β : (a), (b), (c) 2; (d), (e), (f).1; (g), (h), (i) 0.75; (j), (k), (l) 0.65, and (m), (n), (o) 0.5. 51

3.6 (a), (c), (e) Intensity, and (b), (d), (f) phase, from the Eq. 3.33 $U_{\mathrm{aBG\_K}}\left(r,\theta,z=0;c=1\right)$ at n = 3, and different degree of perfectness $\frac{k_{\mathrm{t}}w_{\mathrm{G}}}{2}$: (a), (b), 0.5; (c), (d) 5; and (e), (f) 10. 53

3.7 (a), (c), (e) Intensity, and (b), (d), (f) phase, from the Eq. 3.33 $U_{\mathrm{aBG\_GR}}\left(r,\theta,z=0;\beta=1\right)$ at n = 3, and different degree of perfectness $\frac{k_{\mathrm{t}}w_{\mathrm{G}}}{2}$: (a), (b), 0.5; (c), (d) 5; and (e), (f) 10. 54

3.8 OAM spectrum of $U_{\mathrm{aBG\_GR}}\left(r,\theta,z;\beta=0.5\right)$ at (a) m = 3, (b) m = 3.3, (c) 3.5, (d) 3.9, and (e) 4. 55

List of Figures (Continued)

Figure Page

4.1 The log-polar coordinates mapping from (x,y) to (u,v) unwraps a ring shape into a line, from (u,v) to (x,y) wraps a line shape into a ring.....63

4.2 The optical log-polar wrapping transformation setup from (u,v) to (x,y), the red arrow indicates the Fourier lens location.....65

4.3 The modified setup of optical log-polar wrapping transformation from (u,v) to (x,y), the red arrow indicates the Fourier lens location.....66

4.4 Ideal log-polar wrapping process.....67

4.5 The wrapped ring shift away from the phase corrector's center. (a) m =0 no shift, (b) m = 1.3 bare shift, (c) m = 10.6 obvious shift, (d) m = 30 very large shift.....68

4.6 The far-field asymmetric Bessel Gaussian beam's symmetry comparison. (a) traditional log-polar transform result, m = 4 peak intensity location is high above the x-axis, (b) same charge number, lateral shift suppressed design's peak intensity location lands on approximately the x-axis 71

4.7 Comparing m = 10 shifted ring (green color) and the ideal case zero shift ring (purple color) 72

4.8 The far-field of m = 10 shifted ring (a) intensity, (b) phase, ideal case no shift ring (c) intensity, and (d) phase.....72

4.9 The log-polar OAM modes generation process and the corresponding parameters 74

4.10 Use numerical differences to approximate the partial derivatives.....77

4.11 Input Gaussian beam's intensity and the overlapped wrapper's phase (a) and the corresponding azimuthal Gaussian perfect vortex beam's intensity and the overlapped unwrapper's phase (b).....79

4.12 Comparing two versions of log-polar optics design's

List of Figures (Continued)

Figure Page

far-field intensity under different integer charge numbers 81

5.1 Two practical log-polar OAM mode generation methods
(a) fiber/collimator array; (b) acousto-optic deflector 85

5.2 Diagram of single-lens Fourier transform pair of
lateral shift and linear phase 86

5.3 Diagram of line-generation and log-polar transformation.
Φ_1 – wrapper, Φ_2 – phase corrector, L_2 – Fourier lens with f=154 mm.
Inset (a), line profile on the wrapper inset
(b), ring profile on the phase corrector 88

5.4 The interference OAM mode detection system.
(a) setup, (b) electrical decode system, and
(c) resulting interference pattern and detector aperture (red circle) 90

5.5 The comparison of transmitted sinusoidal signal and
the recovered signal 91

5.6 Comparing the depth of focus measurement of Gaussian beam and
asymmetric fractional Bessel Gaussian beam 93

5.7 The setup of two collimators HOBBIT beam generation 94

5.8 The generated charge ±2 asymmetric Bessel Gaussian beams 94

6.1 (a) The proposed AOD concept,
(b) illustration of the beam profiles at the AOD,
after the line generator and after the log-polar optics and
(c) the momentum vector diagram 101

6.2 Analytic intensity and phase profiles for m = ±3, ±1.2 and 0 108

6.3 (a) Multiple log-polar device fabrication on a single wafer,
(b) the microscope image of central part of wrapper and
(c) phase corrector, (d) the 130× magnification SEM inspection of
device center of wrapper and (e) phase corrector 107 110

6.4 Diagram of the acousto-optic deflector, line-generator and
log-polar transformation optics 111

List of Figures (Continued)

Figure Page

6.5 Picture of the continuously tunable OAM generation system 112

6.6 Comparison of analytic expression with $\beta = 0.663$ and $\rho_0 = 850$ μm 113

6.7 The simulated and experiment results of BG beams central dark area's radius vary with charge number as well as AOD driving signal's frequency 113

6.8 Experimentally generated and simulated fractional OAM BG beams..... 114

LIST OF ACRONYMS

ALD – Atomic Layer Deposition
AOD – Acousto-Optical Deflector
AR – Anti-Reflection
ASE – Amplified Spontaneous Emission
AWG – Arbitrary Waveform Generator

BG – Bessel Gaussian

DE – Diffraction Efficiency
DMD – Digital Micro-mirror Devices

FWHM – Full Width at Half Maximum

HOBBIT – Higher Order Bessel Beams Integrated in Time
HG – Hermite Gaussian
HyG – Hypergeometric
HyGG – Hypergeometric Gaussian

LASER – Light Amplification by Stimulated Emission of Radiation
LG – Laguerre-Gaussian

MPLC – Multiplane Light Conversion

OAM – Orbital Angular Momentum

RF – Radio Frequency
RS – Rayleigh-Sommerfeld

SA – Simulated Annealing
SDM – Space-Division Multiplexing
SEM – Scanning Electron Microscope
SHG – Second Harmonic Generation
SLM – Spatial Light Modulator
SPP – Spiral Phase Plate

TeO_2 – Tellurium Dioxide

UPMC – Unitary Programmable Mode Converter

CHAPTER ONE

INTRODUCTION

1.1 General overview

The orbital angular momentum (OAM) is a fundamental phenomenon in nature. It exists everywhere in daily life and research topics, from flushing toilets and laundry machine whirlpool to dolphin bubble ring to hurricane eye hydrodynamic vortices to spiral galaxies orbiting black holes to quantum vortices. In 1992, Allen first brought the optical OAM concept [1]. The study of the optical OAM has thrived for 28 years, and the researchers' passion has never faded. Analog to the chicken or the egg causality dilemma, the OAM and singularity are always the inherently connected twin phenomena. Similar to fundamental particle's quantization, the singularity is always quantized. Then if the singularity is quantized, what does fractional OAM mean?

Berry opened the fractional charge OAM topic in 2004 [2]. He analyzed the fundamental fractional charge spiral phase structure using the Fourier series expansion method. The conclusion was the fractional OAM structure is the linear combination of integer OAMs. The beam propagation process will smooth the initial phase discontinuity. This phenomenon is also proved by following fractional OAM researches [3-8]. One can consider phase discontinuity, especially for the half-integer case, as a tight chain of singularities extending from the center of the spiral phase profile to infinity along the radial coordinate direction. But it is not a stable status. Once the beam propagates in space or the electromagnetic field oscillates with time, the singularity chain will break into several individual isolated singularities. And this phenomenon is a perfect physical demonstration

of the mathematical "Hilbert Hotel" mechanism [4]. The Kármán vortex street is a helpful analog and visualization of the breaking singularity chain phenomenon.

This dissertation will focus on the generation and manipulation of a fractional OAM mode, namely higher-order Bessel Gaussian beams. It will show the details from analytical theory development to phase-only diffractive optics' design, fabrication, optimization, to experimental verification of the beam's generation and manipulation. This research can find its benefit in a thorough understanding of the fractional OAM modes and asymmetric Bessel Gaussian beam, spatial division multiplexing communication, environment probing, high power OAM mode propagation, filamentation generation and control, optical tweezer, particle manipulation, and laser-matter interaction studies.

1.2 Diffractive optics

We use diffractive passive phase front modulators, namely diffractive optics, to generate the higher-order fractional Bessel Gaussian beam. The diffractive optics have been extensively introduced by peer works [9-11]. In this research, we apply a collimated Gaussian beam to go through the diffractive optic. Then the 1st diffraction order output is the desired modulated beam. The diffractive optic is the thinner version of the refractive optic. Thanks to the periodic property of the electromagnetic field's phase, any large value phase manipulation could be reduced to a single [-π, π] zone. We use the binary lithography method to fabricate the diffractive optics. After four rounds of binary pattern print and etching, a sixteen steps phase stair shape is fabricated. The first-order diffraction efficiency is determined by the stair numbers. The sixteen steps phase profile's first-order diffraction efficiency is about 98%.

1.3 Log-polar optics and asymmetric fractional Bessel Gaussian beam

As early as 1974, Bryngdahl [12,13] has developed a geometrical transformations method, which is also known as coordinate transformation [14] or coordinate mapping in the later relevant researches. The geometric transformations were first studied to process images, such as image registration, mapping, and object recognition. In 1983, the log-polar transformation was brought out to realize the scale and rotation invariant correlation [15]. Modern log-polar transform optics was used to map the OAM beam's spiral phase/momentum to linear phase/momentum, then sort the OAM modes through a simple Fourier transform [16]. In 2013, Mirhosseini and co-workers cascaded fan-out optics after the log-polar elements to increase the mode sorter's separation efficiency [17]. In 2017, Wan and the co-workers used the same fan-out idea but integrated the fan-out phase and log-polar phase to reduce the total number of the phase elements [18]. Since 2017, Ruffato and co-workers have made endeavors to improve the miniaturization and alignment simplicity [19-21]. In 2019, Ruffato redesigned the log-polar elements to expand the paraxial transformation to the non-paraxial region [22].

The log-polar optical geometric coordinate transform is the technique that we use to generate the asymmetric Bessel Gaussian beam, a linear combination of Bessel Gaussian beams. Bessel Gaussian beam has non-diffraction, self-healing properties. But the well-known asymmetric Bessel Gaussian beam was presented by Kotlyar in 2014 [23]. These two groups of beams have a connection but fundamentally different. The detail will be addressed in Chapter 3.

The log-polar transform optics generating OAM mode has an inherent error, which will affect the generated OAM modes' quality. We first time, to our knowledge, pointed out and analyzed the reason and the solution of the error. The detail will be presented in Chapter 4.

1.4 Motivation and peer works

In 2004, M. Berry's famous paper has first time evaluated the fractional charged plane wave's average OAM (total singularity strength in the original paper), then numerically resolved the integration formula, concluded from the numerical result a simple, elegant form [2]. For a Gaussian beam carrying fractional OAM, the average OAM has been investigated from the quantum perspective [24] and the diffraction theory [25]. But to date, for either case, the fractional average charge number always deviates away from the initial SPP's charge number. That means the average OAM conservation law has been challenged. We have proposed the new asymmetric fractional pseudo perfect vortex beam to fit in the blank. The Fourier transform of the proposed beam is an asymmetric fractional Bessel Gaussian beam. Which average fractional charge number always keeps around the initial designed fractional charge, much smaller deviation comparing state of the art fractional OAM modes. The OAM spectrum, the unique property, and the propagation expression of the proposed asymmetric fractional Bessel Gaussian beam are all delivered in Chapters 3, 5, and 6.

1.5 Dissertation outline

The dissertation outline is as follows. Chapter 1 introduce the background, relevant concept, motivation, peer work, and the outline of the dissertation.

Chapter 2 presents the advanced integer OAM modes, namely concentric vortices. The multi-harmonic design of the concentric vortices is analyzed and demonstrated. We derived the modulated beam's Fresnel propagation expression for the first time to our knowledge. The unique property of the generated beam is discussed in detail. The lobe pattern rotates with the Gouy phase variation along the propagation process.

Chapter 3 discusses the fractional OAM and asymmetric Bessel Gaussian beam topics. Fractional OAM is inherently the coherent combination of integer OAM modes. Therefore, for each specific fractional OAM mode, there is an OAM spectrum to represent the combination. And the fractional OAM mode's spectrum is centered (or power averaged) at a fractional OAM value. Meanwhile, the OAM spectrum and the azimuthal distribution are a Fourier transform pair. Hence, given a uniform azimuthal distributed light field such as Gaussian or Gaussian rings, as long as the OAM spectrum exists, the propagated fractional OAM mode will eventually evolve into an asymmetric azimuthal distribution. The asymmetric Bessel Gaussian beam and the azimuthal Gaussian perfect vortex beam are a Fourier transform pair. They propagate into each other no matter the initial OAM spiral phase is an integer or fractional. Moreover, if the initial OAM spiral phase is a fractional structure, the Fourier transform of which is still centered at the adjacent of the initial fractional OAM setting. We will also compare our azimuthal Gaussian perfect vortex's asymmetric Bessel Gaussian beam with Kotlyar's asymmetric Bessel Gaussian beam in this chapter.

Chapter 4 presents the issue of the log-polar diffractive optics and its improvement. The basic optical coordinate transform theory will be introduced. The traditional log-polar transform design dilemma will be analyzed. Five metrics to evaluate the asymmetric fractional Bessel Gaussian beam's mode quality will be proposed. Finally, a new log-polar design will be delivered in this chapter.

Chapter 5 discusses the Fourier transforming fiber/collimator array method to generate the asymmetric fractional Bessel Gaussian beams. The diffraction limit relationship between the array pitch size and the OAM charge will be proposed for the first time to our knowledge. And two experiment shows the asymmetric fractional Bessel Gaussian beam's generation and control capability.

Chapter 6 delivers the acousto-optical deflector (AOD) based asymmetric fractional Bessel Gaussian beam generation and mode manipulation system. Applying a slight tuning on the AOD's radio frequency signal, the first order deflection's wave vector will change its direction accordingly. And this small change of the beam propagation direction is mapped into OAM mode change by the log-polar coordinate transform optics. Consequently, the generated asymmetric Bessel Gaussian beam's charge number is tunable. Due to the radio frequency tuning is continuous, the resulting OAM charge number could take any fractional value. The only limitation is the frequency signal's resolution. With this capability, the OAM spectrum, OAM's first time variation (torque or force: the first time derivative of the momentum [26, 27]), or even higher time derivative of the momentum could be easily coded and applied in our system.

Chapter 7 offers the conclusion, future work, and main contributions of this research.

CHAPTER TWO

CONCENTRIC SPIRAL PHASE PLATE

2.1 Introduction

Space-division multiplexing (SDM) is an effective method to increase the data capacity of optical communication links. Orbital angular momentum (OAM) modes are a series of orthogonal spatial modes due to the optical vortex beam's helical phase front [28]. Given OAM's unique advantage of handedness and self-healing property [29-32], OAM beams are preferred with SDM [33, 34]. The far-field intensity distribution of an OAM beam is a donut-shaped pattern with phase singularity in the center. It is found that the far-field intensity distribution of two coherently combined OAM beams with opposite charge number is an azimuthally arranged petal-like pattern. The concentric SPP spiral phase plate (SPP) has a unique design: placing two different charge number vortices with opposite signs in a collinear architecture. Providing Gouy phase difference of different OAM modes, the petal-like pattern rotates with propagation. The basic concentric SPP concept is shown in Fig. 2.1.

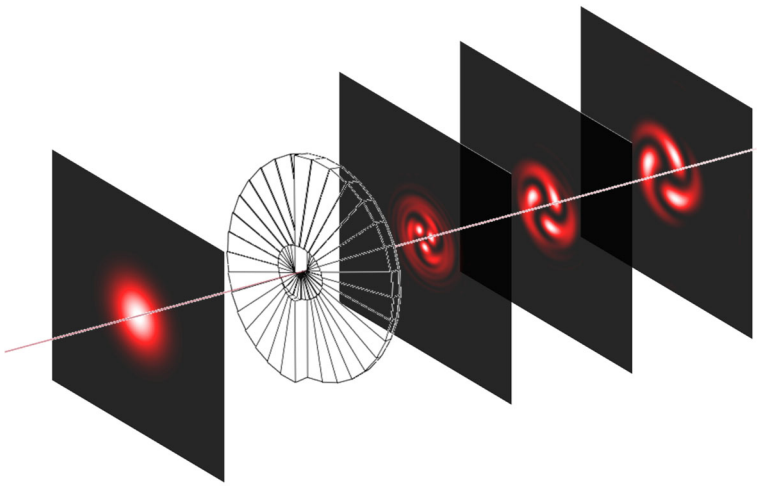

Fig. 2.1. A concentric SPP diffracts a Gaussian beam into a petal-like pattern.

Vijayakumar and his colleagues have derived the multilevel OAM holograms' OAM spectrum [35]. The multilevel OAM holograms have the same phase distribution as binary diffractive SPP. But the OAM spectrum of OAM holograms with multiple phase discontinuity is still an open question. And the multiple harmonic property of the binary OAM holograms is a valuable topic to develop. The concentric SPP is a valuable design because its helical filamentation [36-38], underwater communication [39], and laser mode amplification applications [40] have been demonstrated. Given this, introducing double axicon phases to a coherent combination of ±1 OAM modes, a filamentation control application [36-38] has been studied. Concentric SPP optics can similarly realize the filament control [36-38] but only by utilizing one diffractive optic rather than four. By dynamically moving the peak intensity location, micromanipulation could be realized through the use of concentric SPP optics. The multiple harmonic wavelength design is motivated by the applications of filamentation and directed energy. The multiple harmonic concentric SPP optics realize a single optic for OAM mode modulation for multiple wavelengths. Compared with traditional individual wavelength OAM mode modulation, this method reduces the number of optics and improves power efficiency, which is very important for high power applications.

In this chapter, we analyzed the general form of multiple harmonic binary diffractive SPP's OAM spectrum. The Fresnel propagation of Gaussian beam go through concentric SPP is derived base on the Bessel function's power series expansion and the incomplete gamma function's integration expression. 2090 nm and 1064 nm are selected

for their use as two essential transmission wavelengths in the atmospheric window, though any harmonic pair could be used. A 1064 nm laser source and 2090 nm laser source are multiplexed and allowed to pass through a single concentric SPP, which is modulo 2π diffractive design for 2090 nm and modulo 4π design for 1064 nm. Analytic expression and experimental results show that both wavelengths produce petal-like patterns in the far-field after propagating through the concentric SPP. These petal-like patterns rotate about the propagation axis before, during, and after the back Fourier plane of a Fourier lens.

2.2 Multiple harmonic binary diffractive SPP

The concentric SPP is designed as the radial combination of two binary diffractive SPPs. In this sense, the binary diffractive SPP is the fundamental element of concentric SPPs. We are trying to explore the multiple harmonic property of the binary diffractive SPP by analyzing the OAM spectrum. Considering the diffractive index difference, the fraction of 2π phase delay of two wavelengths is given by [41]

$$\alpha = \frac{\lambda_0 \left(n_\lambda - 1\right)}{\lambda \left(n_{\lambda_0} - 1\right)}, \tag{2.1}$$

where λ_0 and λ are the 1st harmonic wavelength and an arbitrary wavelength, respectively; n_{λ_0} and n_λ are the refractive indices of wavelength λ_0 and λ, respectively. The charge number of the identical SPP for wavelength λ is given by

$$m_\lambda = \alpha m_{\lambda_0}, \tag{2.2}$$

where m_{λ_0} is the charge number of the SPP for the 1st harmonic wavelength λ_0. Figure 2.2 is a typical binary diffractive SPP phase distribution with the 1st harmonic charge number 2.

Fig. 2.2 A 16 levels charge 2 SPP's phase profile. The $\alpha 2\pi$ phase is corresponding with an arbitrary wavelength.

The diffractive designs compress phase over 2π into the [0, 2π) range to make the element extremely thin. In other words, over 2π phase in a singular optic forces branch cuts because there is a compressed representation of the desired domain into a physical 2π domain on the optic space. The faster the phase gradient, the more the phase branch cuts. For a more general description, the total number of phase branch cuts is the same as $\left|m_{\lambda_0}\right|$, the total number of step levels from the lowest to the highest as *N*. When the wavelength walks off from the harmonic wavelengths, the α parameter, Eq. (2.1), will be fractional. Consequently, the charge number will be fractional. The OAM spectrum could be represented by the Fourier series of the fractional OAM phase [2, 4, 35, 42]. For a general light field represented by a separable function $U(\rho,\phi)=\mathrm{P}(\rho)\Psi(\phi)$, the Fourier series of the azimuthal component $\Psi(\phi)$ is

$$\Psi(\phi) = \sum_{n=-\infty}^{\infty} A_n \exp(\mathrm{j}n\phi), \tag{2.3}$$

where ρ and ϕ are the polar coordinates, n is the OAM order taking integer values, the Fourier series coefficients are

$$A_n = \frac{1}{2\pi}\int_0^{2\pi} \Psi(\phi)\exp(-\mathrm{j}n\phi)\,\mathrm{d}\phi. \tag{2.4}$$

The combination of integer OAM modes could represent any arbitrary azimuthal phase. And the relationship $\sum_n |A_n|^2 = 1$ should always hold due to the power conservation reason. The phase branch cut is not a problem for harmonic wavelengths because of the optical phase's periodic property. But the phase discontinuity will be a real phase gap for other wavelengths walking off from the harmonic wavelengths. The one branch cut smooth diffractive OAM phase's Fourier series has been given by [2, 4]. For arbitrary integer branch cut binary diffractive SPP, suppose the phase delay is evenly distributed among the steps, the n^{th} order Fourier series coefficients are given by

$$A_n\left(\left|m_{\lambda_0}\right|\right) = \begin{cases} \mathrm{j}\exp\left(\mathrm{j}\dfrac{\mathrm{sign}\left(m_{\lambda_0}\right)\alpha\pi}{N}\right)\exp\left[\mathrm{j}\dfrac{\pi\left(m_\lambda - n\right)}{\left|m_{\lambda_0}\right|}\right]\cdot\mathrm{sinc}\left(\dfrac{k}{N}\right)\dfrac{\mathrm{sinc}\left(\dfrac{m_\lambda - n}{\left|m_{\lambda_0}\right|}\right)}{\mathrm{sinc}\left(\dfrac{m_\lambda - n}{\left|m_{\lambda_0}\right| N}\right)}, \\ \qquad\qquad n = k\left|m_{\lambda_0}\right|,\ k \text{ is an integer}; \\ 0, \text{ others}. \end{cases} \tag{2.5}$$

The normalized power ratio $|A_n|^2$ represents the n^{th} order OAM mode's diffractive efficiency. Given a fixed total level number $N = 16$, the phase discontinuity number $\left|m_{\lambda_0}\right| = 2$, and the first harmonic wavelength 2090 nm, the wavelength-dependent diffractive

efficiency plot is shown in Fig. 2.3. There are two sets of harmonics, the wavelength harmonic and the OAM mode harmonic. The power continuously decays along the wavelength axis in the sinc-squared function, but the power only exists in the harmonic OAM modes. The nonharmonic OAM modes are empty. In Fig. 2.3, the power only exists in the even OAM modes.

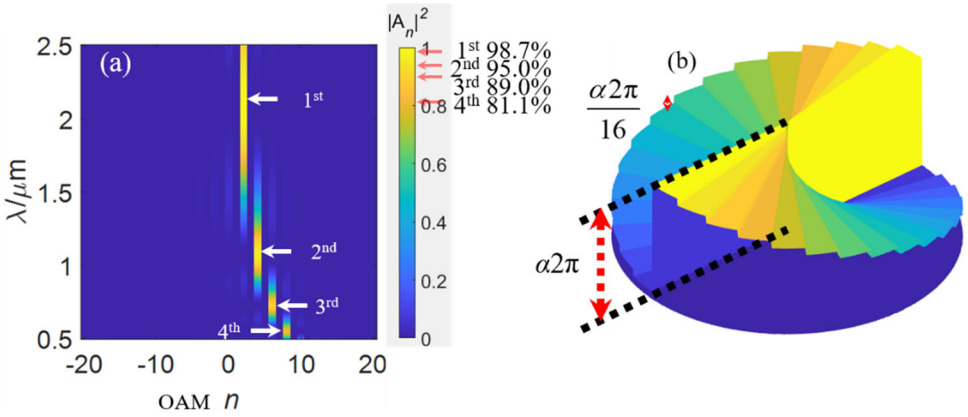

Fig. 2.3. The $N = 16$ levels $\left|m_{\lambda_0}\right| = 2$ SPPs' wavelength-dependent diffraction efficiency $\left|A_n\right|^2$. (a) The first four harmonic charge 2, 4, 6, 8, (b) the corresponding 16 levels binary SPP.

The multiple harmonic binary diffractive SPP is the fundamental element of concentric SPPs. We define the 1st harmonic order wavelength as 2090 nm and the 2nd harmonic order wavelength as 1064 nm in our design. The inner SPP's 1st harmonic charge number $m_{\text{in\_}\lambda_0} = m_{\text{in\_2090}} = 1$, and the outer SPP's 1st harmonic charge number $m_{\text{out\_}\lambda_0} = m_{\text{out\_2090}} = -2$, the inner SPP's radius $\rho_{\text{in}} = 0.625$ mm, the outside boundary's radius $\rho_{\text{out}} = 2.5$ mm, and the total level number is $N = 16$. Applying Eq. (2.2), the same

concentric SPP works for harmonic wavelength 1064 nm, and the charge numbers are $m_{\text{in\_}\lambda} = m_{\text{in\_1064}} = 2,\ m_{\text{out\_}\lambda} = m_{\text{out\_1064}} = -4$. The simulated phase profile and the final optic microscope image are shown in Fig. 2.4.

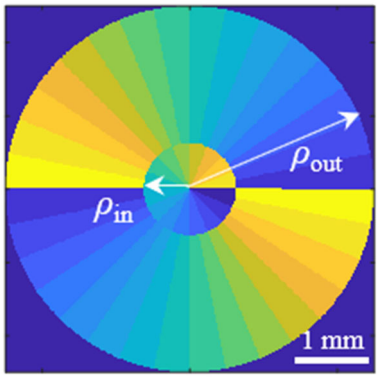

Fig. 2.4. The simulated phase profile of multiple harmonic concentric SPP, the inner and outer SPP's radius are ρ_{in} and ρ_{out}, respectively.

As Fig. 2.4 illustrated, the concentric optic's transmittance phase function is given by

$$\tau(\rho,\phi) = \text{circ}(\rho/\rho_{\text{in}}) \sum_{n=-\infty}^{\infty} A_n(1)\exp(\text{j}n\phi) + \left[\text{circ}(\rho/\rho_{\text{out}}) - \text{circ}(\rho/\rho_{\text{in}})\right] \cdot \sum_{n=-\infty}^{\infty} A_n(2)\exp(\text{j}n\phi) \tag{2.6}$$

where ρ and ϕ are the polar coordinates, j is the imaginary unit, ρ_{in} and ρ_{out} are the radius of the inner and outer vortex phase plate. There is $|m_{\lambda_0}| = 1$ branch cut for the inner SPP phase, and $|m_{\lambda_0}| = 2$ branch cuts for the outer SPP phase. The phase expressions

$\sum_{n=-\infty}^{\infty} A_n(1)\exp(jn\phi)$ and $\sum_{n=-\infty}^{\infty} A_n(2)\exp(jn\phi)$ are representing the binary SPP phase of inner and outer SPP. According to Eq. (2.5), the Fourier coefficients are expressed as

$$A_n(1) = \mathrm{j}\exp\left(\mathrm{j}\frac{\pi m_{\mathrm{in}\_\lambda}}{N}\right)\exp\left[\mathrm{j}\pi\left(m_{\mathrm{in}\_\lambda}-n\right)\right]\mathrm{sinc}\left(\frac{n}{N}\right)\cdot\frac{\mathrm{sinc}\left(m_{\mathrm{in}\_\lambda}-n\right)}{\mathrm{sinc}\left(\frac{m_{\mathrm{in}\_\lambda}-n}{N}\right)}, \tag{2.7}$$

$$A_n(2) = \begin{cases} \mathrm{j}\exp\left(\mathrm{j}\frac{\pi m_{\mathrm{out}\_\lambda}}{2N}\right)\exp\left[\mathrm{j}\frac{\pi\left(m_{\mathrm{out}\_\lambda}-n\right)}{2}\right]\cdot\mathrm{sinc}\left(\frac{n}{2N}\right)\frac{\mathrm{sinc}\left(\frac{m_{\mathrm{out}\_\lambda}-n}{2}\right)}{\mathrm{sinc}\left(\frac{m_{\mathrm{out}\_\lambda}-n}{2N}\right)}, \\ \qquad\qquad n \text{ is an even integer}, \\ 0, \text{ others}. \end{cases} \tag{2.8}$$

where $m_{\mathrm{in}\_\lambda} = \alpha m_{\mathrm{in}\_\lambda_0}$ and $m_{\mathrm{out}\_\lambda} = \alpha m_{\mathrm{out}\_\lambda_0}$ are the charge numbers of the inner and outer vortex phase for input wavelength λ. Applying Eqs. (2.6)-(2.8) into the Fresnel transform, the diffraction of the concentric SPP is derived in the next section.

2.3 Gaussian beam through an SPP

The diffraction of the Gaussian beam by the vortex phase SPP has been well-studied, and the generated beam is considered as a hypergeometric Gaussian or Kummer beam [1, 43-45]. The diffraction of plane waves by finite-radius SPPs with integer and the fractional topological charge has been derived by [46, 47]. From the perspective of a truncated Gaussian beam's diffraction, the aperture effect has been studied by [48, 49]. To the best of the authors' knowledge, the diffraction of Gaussian beams by the finite apertured vortex SPP is still an open question to be answered. Considering scalar paraxial diffraction of a collimated Gaussian beam passing through the regular vortex SPP with the finite radius of ρ_{SPP}, the resulting vector complex field is given by

$$\vec{U}_{\mathrm{G}}\left(\rho,\phi\right)=U_{\mathrm{G}}\left(\rho,\phi\right)\cdot\hat{y}=\exp\left[-\rho^{2}\left(\frac{1}{w^{2}}+\frac{\mathrm{j}\pi}{\lambda R}\right)\right]\exp\left(\mathrm{j}m\phi\right)\mathrm{circ}\left(\frac{\rho}{\rho_{\mathrm{SPP}}}\right)\cdot\hat{y},\quad(2.9)$$

where $\hat{y}$ defines the vertical polarization state, w and R are the radius and the radius of curvature of the Gaussian beam, respectively, and m is the charge number of the vortex phase.

The Fresnel transform of the modulated Gaussian $U_{\mathrm{G}}\left(\rho,\phi\right)$ in polar coordinates is given by

$$\begin{aligned}U_{\mathrm{Fresnel}}\left(r,\theta,z\right)=&\frac{\exp\left(\dfrac{\mathrm{j}2\pi z}{\lambda}+\dfrac{\mathrm{j}\pi}{\lambda z}r^{2}\right)}{\mathrm{j}\lambda z}\int_{0}^{2\pi}\int_{0}^{\rho_{\mathrm{SPP}}}\exp\left\{-\rho^{2}\left[\frac{1}{w^{2}}-\frac{\mathrm{j}\pi}{\lambda}\left(\frac{1}{z}-\frac{1}{R}\right)\right]\right\}\\&\cdot\exp\left[\mathrm{j}m\phi-\mathrm{j}\frac{2\pi}{\lambda z}\rho r\cos\left(\theta-\phi\right)\right]\rho\mathrm{d}\rho\mathrm{d}\phi,\end{aligned}\quad(2.10)$$

where r and θ are the polar coordinates of the transformed field, and z is propagation distance. According to the general two-dimensional polar coordinate Fourier transforms integration method in [50], Eq. (2.6) will reduce to

$$\begin{aligned}U_{\mathrm{Fresnel}}\left(r,\theta,z\right)=&\frac{2\pi}{\mathrm{j}\lambda z}\exp\left(\mathrm{j}\frac{2\pi z}{\lambda}+\mathrm{j}\frac{\pi}{\lambda z}r^{2}+\mathrm{j}m\theta\right)\\&\cdot\int_{0}^{\rho_{\mathrm{SPP}}}\exp\left\{-\rho^{2}\left[\frac{1}{w^{2}}-\frac{\mathrm{j}\pi}{\lambda}\left(\frac{1}{z}-\frac{1}{R}\right)\right]\right\}J_{m}\left(\frac{2\pi}{\lambda z}r\rho\right)\rho\mathrm{d}\rho.\end{aligned}\quad(2.11)$$

From here, refer to the power series expansion of n-th order Bessel function of the first kind

$$J_{n}\left(x\right)=\sum_{k=0}^{\infty}\frac{\left(-1\right)^{k}}{k!\left(n+k\right)!}\left(\frac{x}{2}\right)^{n+2k},\quad(2.12)$$

and the integral solution 3.381.8 from [51]

$$\int_0^u x^m \exp\left(-bx^n\right)\mathrm{d}x = \frac{\gamma\left(v, bu^n\right)}{nb^v},\ v = \frac{m+1}{n}, \left[u>0, \mathrm{Re}\,v>0, \mathrm{Re}\,n>0, \mathrm{Re}\,b>0\right], \quad (2.13)$$

where $\gamma(\cdot,\cdot)$ is the lower incomplete gamma function, Eq. (2.7) is solved

$$\begin{aligned} U_{\text{Fresnel}}(r,\theta,z) = \frac{\pi}{\mathrm{j}\lambda z}\exp\left(\mathrm{j}\frac{2\pi z}{\lambda} + \mathrm{j}\frac{\pi}{\lambda z}r^2 + \mathrm{j}m\theta\right)\beta^{-\frac{m+2}{2}}\left(\frac{\pi r}{\lambda z}\right)^m \\ \cdot\sum_{k=0}^{\infty}\frac{(-1)^k\beta^{-k}}{k!(m+k)!}\left(\frac{\pi r}{\lambda z}\right)^{2k}\gamma\left(\frac{m}{2}+k+1, \beta{\rho_{\text{SPP}}}^2\right), \end{aligned} \quad (2.14)$$

where $\beta = \frac{1}{w^2} - \frac{\mathrm{j}\pi}{\lambda}\left(\frac{1}{z}-\frac{1}{R}\right)$. At $z = R$ (for a collimated beam, $R\to\infty, R \gg z_0$, $z_0 = \frac{\pi w^2}{\lambda}$ is the Rayleigh range), $\beta = \frac{1}{w^2}$, from Eq. (2.10) the Fraunhofer diffraction of the modulated Gaussian by SPP is

$$\begin{aligned} U_{\text{Fraunhofer}}(r,\theta,z\to\infty) = \frac{\pi w^2}{\mathrm{j}\lambda z}\exp\left(\mathrm{j}\frac{2\pi z}{\lambda} + \mathrm{j}\frac{\pi}{\lambda z}r^2 + \mathrm{j}m\theta\right)\left(\frac{\pi r w}{\lambda z}\right)^m \\ \cdot\sum_{k=0}^{\infty}\frac{(-1)^k}{k!(m+k)!}\left(\frac{\pi r w}{\lambda z}\right)^{2k}\gamma\left(\frac{m}{2}+k+1, \sigma^2\right), \end{aligned} \quad (2.15)$$

The truncation parameter $\sigma = \frac{\rho_{\text{SPP}}}{w}$ determines the aperture effect. At $\rho_{\text{SPP}}\to 0$, the $\sigma\to 0$, the aperture closes, and the beam will be stopped. At $\rho_{\text{SPP}}\to\infty, \rho_{\text{SPP}} \gg w$, the $\sigma\to\infty$, then the lower incomplete gamma function turns into gamma function, the Eq. (2.11) turns into a hypergeometric Gaussian or Kummer beam[47].

2.4 Diffraction theory of multiple harmonic concentric SPP

The diffraction of Gaussian beams by the concentric SPP phase plate is essentially the interference of hypergeometric Gaussian beams with an aperture effect. Considering

scalar paraxial diffraction of a collimated Gaussian beam passing through the concentric SPP, the resulting vector complex field is given by

$$\vec{U}_{\mathrm{G}}\left(\rho,\phi\right)=\exp\left[-\rho^{2}\left(\frac{1}{w^{2}}+\frac{\mathrm{j}\pi}{\lambda R}\right)\right]\tau(\rho,\phi)\cdot\hat{y}=\left[U_{\mathrm{G1}}\left(\rho,\phi\right)+U_{\mathrm{G2}}\left(\rho,\phi\right)\right]\cdot\hat{y}, \tag{2.16}$$

$$U_{\mathrm{G1}}\left(\rho,\phi\right)=\exp\left[-\rho^{2}\left(\frac{1}{w^{2}}+\frac{\mathrm{j}\pi}{\lambda R}\right)\right]\mathrm{circ}\left(\frac{\rho}{\rho_{\mathrm{in}}}\right)\sum_{n=-\infty}^{\infty}A_{n\_\mathrm{in}}\exp\left(\mathrm{j}n\phi\right), \tag{2.17}$$

$$U_{\mathrm{G2}}\left(\rho,\phi\right)=\exp\left[-\rho^{2}\left(\frac{1}{w^{2}}+\frac{\mathrm{j}\pi}{\lambda R}\right)\right]\left[\mathrm{circ}\left(\frac{\rho}{\rho_{\mathrm{out}}}\right)-\mathrm{circ}\left(\frac{\rho}{\rho_{\mathrm{in}}}\right)\right]\sum_{n=-\infty}^{\infty}A_{n\_\mathrm{out}}\exp\left(\mathrm{j}n\phi\right), \tag{2.18}$$

where w and R are the radius and the radius of curvature of the Gaussian beam, respectively, the U_{G1} and U_{G2} are the collimated Gaussian beam modulated by inner and outer vortex SPP, respectively. The Gaussian beam diameter has been chosen as approximately 2.7 mm (approximately 35% of the Gaussian power passes through the inner SPP), which is much larger than the inner disc's 1.25 mm diameter, and all the power has been contained in the $2\times\rho_{\mathrm{out}}=5$ mm range. Then, the outside aperture effect is neglectable for the input beam, and Eq. (2.14) will reduce to a simpler form

$$U_{\mathrm{G2}}\left(\rho,\phi\right)=\exp\left[-\rho^{2}\left(\frac{1}{w^{2}}+\frac{\mathrm{j}\pi}{\lambda R}\right)\right]\left[1-\mathrm{circ}\left(\frac{\rho}{\rho_{\mathrm{in}}}\right)\right]\sum_{n=-\infty}^{\infty}A_{n\_\mathrm{out}}\exp\left(\mathrm{j}n\phi\right). \tag{2.19}$$

The Fresnel transform of the modulated Gaussian $U_{\mathrm{G1}}\left(\rho,\phi\right)$ in polar coordinates is solved as

$$U_1(r,\theta,z)=\frac{\pi}{\mathrm{j}\lambda z}\exp\left(\mathrm{j}\frac{2\pi z}{\lambda}+\mathrm{j}\frac{\pi}{\lambda z}r^2\right)\cdot \sum_{n=-\infty}^{\infty}\left[\begin{array}{l} A_{n\_\mathrm{in}}\exp(\mathrm{j}n\theta)\beta^{-\frac{n+2}{2}}\left(\frac{\pi r}{\lambda z}\right)^n \\ \cdot\sum_{k=0}^{\infty}\frac{(-1)^k\beta^{-k}}{k!(n+k)!}\left(\frac{\pi r}{\lambda z}\right)^{2k}\gamma\left(\frac{n}{2}+k+1,\beta\rho_{\mathrm{in}}{}^2\right)\end{array}\right], \tag{2.20}$$

where $\beta=\frac{1}{w^2}-\frac{\mathrm{j}\pi}{\lambda}\left(\frac{1}{z}-\frac{1}{R}\right)$, $\gamma(\cdot,\cdot)$ is the lower incomplete gamma function. Similar to Eq. (2.16), the Fresnel transform of the $U_{\mathrm{G2}}(\rho,\phi)$ in the polar coordinate is given by

$$U_2(r,\theta,z)=\frac{\pi}{\mathrm{j}\lambda z}\exp\left(\mathrm{j}\frac{2\pi z}{\lambda}+\mathrm{j}\frac{\pi}{\lambda z}r^2\right)\cdot \sum_{n=-\infty}^{\infty}\left[\begin{array}{l} A_{n\_\mathrm{out}}\exp(\mathrm{j}n\theta)\beta^{-\frac{n+2}{2}}\left(\frac{\pi r}{\lambda z}\right)^n \\ \cdot\sum_{k=0}^{\infty}\frac{(-1)^k\beta^{-k}}{k!(n+k)!}\left(\frac{\pi r}{\lambda z}\right)^{2k}\Gamma\left(\frac{n}{2}+k+1,\beta\rho_{\mathrm{in}}{}^2\right)\end{array}\right], \tag{2.21}$$

where $\Gamma(\cdot,\cdot)$ is the upper incomplete gamma function. The final scalar and vector forms Fresnel transform of the input Gaussian $U_{\mathrm{G}}(\rho,\phi)$ in polar coordinate are

$$\vec{U}_{\mathrm{Fresnel}}(r,\theta,z)=U_{\mathrm{Fresnel}}(r,\theta,z)\cdot\hat{y}=\left[U_1(r,\theta,z)+U_2(r,\theta,z)\right]\cdot\hat{y}. \tag{2.22}$$

where $\hat{y}$ defines the vertical polarization state. The derivation details are included in the appendix, within which the Bessel function's power series and the incomplete gamma function's integration forms are applied. This method could help with the circular apertured OAM mode's diffraction analysis. To confirm the fidelity of the analytical expression of Eq. (2.22), the single-lens (f = 200 mm) Fourier transform of concentric SPP beam (m_{in} = 1, $m_{\mathrm{out}}=-2$) has been plotted using both the analytical expression derived above and the

Rayleigh-Sommerfeld (RS) diffraction propagation simulation method. As Fig. 2.5 shows, the far-field intensity is compared. The resulting complex field's complex correlation coefficient is computed as 99%.

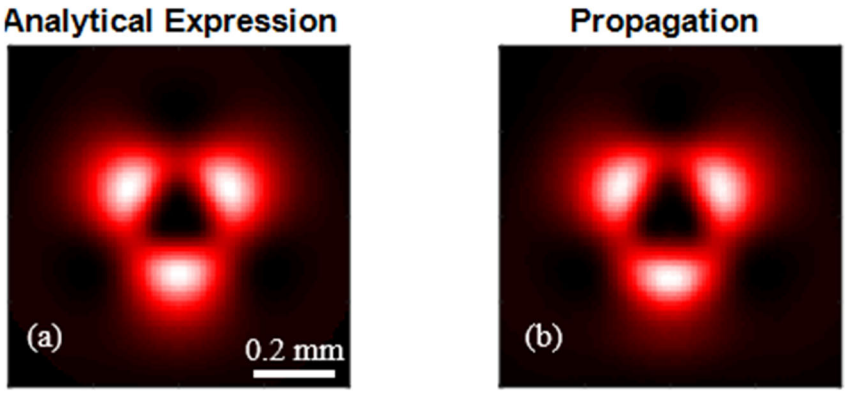

Fig. 2.5. Far-field intensity of concentric SPP beam with charge $m_{in} = 1$, $m_{out} = -2$ (a) analytical expression and (b) RS propagation method.

2.5 Gouy phase caused rotation

The interference between the two OAM states produces periodic interference fringes of constructive and destructive interference in the azimuthal direction, producing petal-like lobes in the intensity profile. The resulting peak intensity (bright lobes) or vortices (dark region) are evenly distributed. The distribution angle and the rotation of the peak and null intensity follow the same trend. The distribution angle can be expressed by [52]

$$\phi_n = \frac{\delta + n\pi + \alpha\left(\left|m_{\text{in}\_\lambda_0}\right| - \left|m_{\text{out}\_\lambda_0}\right|\right)\xi_\lambda}{\alpha\left(m_{\text{in}\_\lambda_0} - m_{\text{out}\_\lambda_0}\right)}, \tag{2.23}$$

where δ is the phase difference between the inner and outer OAM beams, $n = 1, \cdots, |m_{\text{in}} - m_{\text{out}}|$ is the number of the bright petals, and $\xi = \arctan\left(\frac{z}{z_0}\right)$ is the Gouy phase of Gaussian beam, $z_0 = \frac{\pi w^2}{\lambda}$ is the Rayleigh range. As the beam propagates, the azimuthal position of the n petals will rotate due to the Gouy phase change.

$$\frac{\mathrm{d}\phi_n}{\mathrm{d}z} = \frac{\left(\left|\alpha m_{\text{in}\_\lambda_0}\right| - \left|\alpha m_{\text{out}\_\lambda_0}\right|\right)}{\alpha m_{\text{in}\_\lambda_0} - \alpha m_{\text{out}\_\lambda_0}} \frac{\mathrm{d}\xi_\lambda}{\mathrm{d}z} = \frac{\left(\left|m_{\text{in}\_\lambda_0}\right| - \left|m_{\text{out}\_\lambda_0}\right|\right) z_0}{\left(m_{\text{in}\_\lambda_0} - m_{\text{out}\_\lambda_0}\right)\left({z_0}^2 + z^2\right)}. \tag{2.24}$$

The rotation angle of the n^{th} bright petal is [52]

$$\Delta\phi_n = \frac{\left(\left|\alpha m_{\text{in}\_\lambda_0}\right| - \left|\alpha m_{\text{out}\_\lambda_0}\right|\right)}{\left(\alpha m_{\text{in}\_\lambda_0} - \alpha m_{\text{out}\_\lambda_0}\right)} \Delta\xi_\lambda = \frac{\left(\left|m_{\text{in}\_\lambda_0}\right| - \left|m_{\text{out}\_\lambda_0}\right|\right)}{m_{\text{in}\_\lambda_0} - m_{\text{out}\_\lambda_0}} \Delta\xi_\lambda. \tag{2.25}$$

The harmonic wavelength petal-like lobe's rotation is only determined by the harmonic wavelength's Gouy phase change $\Delta\xi_\lambda = \Delta\left[\arctan\left(\frac{z\lambda}{\pi w^2}\right)\right]$. As long the beam propagates multiple Rayleigh range away, the Gouy phase change is approaching π.

2.6 Device fabrication and experimental characterization

We use the binary photolithography method to fabricate the concentric SPP on the fused silica substrate, as shown in Fig. 2.6. The SPP's design wavelength is 2090 nm, 2^4 = 16 phase levels represent the phase ramp from 0 to 2π on 2090 nm. Given the refractive index of fused silica operating at 2090 nm as 1.437, the SPP's step depth is 299 μm. The inner and outer SPP's charge numbers are 1 and -2, respectively. The corresponding diameters are 1.25 mm and 5 mm, respectively.

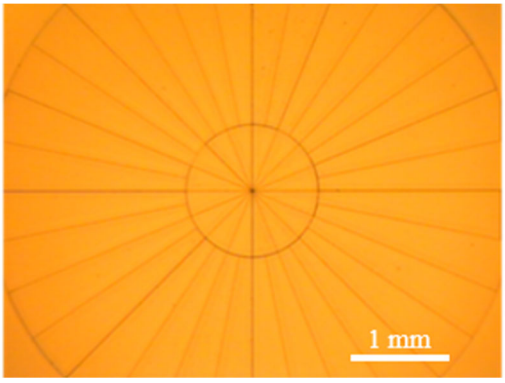

Fig. 2.6. Microscope image of the fabricated multiple harmonic concentric SPP optic.

We designed an experiment to confirm the above theory. The experimental setup is shown in Fig. 2.7. The 2090 nm and 1064 nm lasers were combined by a dichroic mirror to go through the same concentric SPP with designed charge numbers of $m_{in} = 1$, $m_{out} = -2$ for 2090 nm and $m_{in} = 2$, $m_{out} = -4$ for 1064 nm. The inner and outer vortices have diameters of 1.25 mm and 5 mm, respectively. The Fourier lens's focal length is $f = 200$ mm.

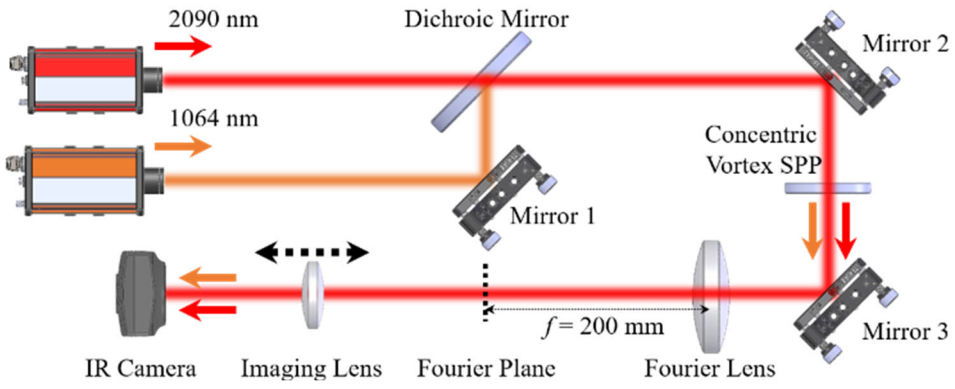

Fig. 2.7. The experimental setup to multiplex the 2090 nm and 1064 nm lasers through a single concentric SPP. The imaging lens helps the infrared camera catch the diffracted patterns at different z location after the Fourier lens.

The Fourier lens is used for the convenient observation of Fraunhofer diffraction patterns. The imaging lens helps image the diffraction patterns after the Fourier lens on the infrared camera. By translating the imaging lens back and forth, the diffracted patterns at different locations after the Fourier lens along the propagation direction are collected by the infrared camera. The focal length of the Fourier lens is 200 mm. The diffraction pattern of the 2090 nm laser after passing through the concentric SPP with topological charge numbers of $m_{\text{in}} = 1,\ m_{\text{out}} = -2$ is a 3-petal pattern, and the 1064 nm counterpart yields a 6-petal pattern. As Fig. 2.8 shows, images of the diffracted patterns located approximately 107 mm, 157 mm, 209 mm, 259 mm, and 308 mm after the Fourier lens have been captured by an infrared camera with the cooperation of the moving imaging lens after the Fourier lens. The mean correlation coefficient between the simulation results of Eq. (2.22) and experimental results have been computed as 92% ± 2%. Both simulation and experimental images are shown in Fig. 2.8. The diffraction patterns rotate $\sim\frac{\pi}{3}$ radians azimuthally while propagating away from the Fourier lens.

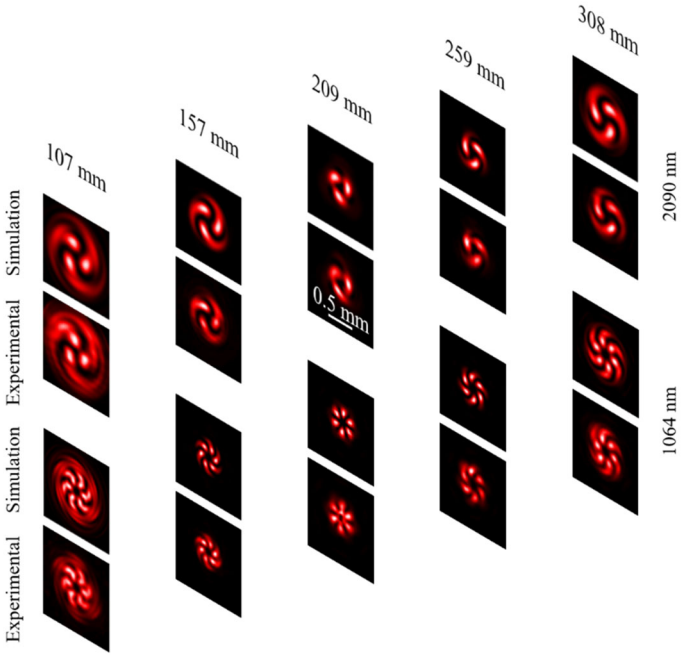

Fig. 2.8. The simulated and experimental petal-like patterns of 2090 nm and 1064 nm at 107 mm, 157 mm, 209 mm, 259 mm, and 308 mm after the Fourier lens.

The images at 209 mm after the Fourier lens are approximately at the focus. As one can tell from the central column frames of Fig. 2.8, the tails of the petals have disappeared at this point because the parabolic phase has evolved into a plane phase. The measured diffraction efficiency of both 1064 nm and 2090 nm is 93% and 94% after compensating for Fresnel losses.

2.7 Discussion

We explored the multi-harmonic diffractive concentric SPP modulating the wavefront of 2090 nm and 1094 nm Gaussian beam in this work. Due to the diffractive optics design's multi-harmonic nature, the same optic works similarly for the 532 nm beam.

The diffraction efficiency $|A_n|^2$ will drop to ~81%, according to Eq. (2.5). In this research, we used a refractive lens to perform a Fourier transform. If we apply the multi-harmonic diffractive lens design, the different harmonic wavelength will see different lens phase, as shown in Fig. 2.9.

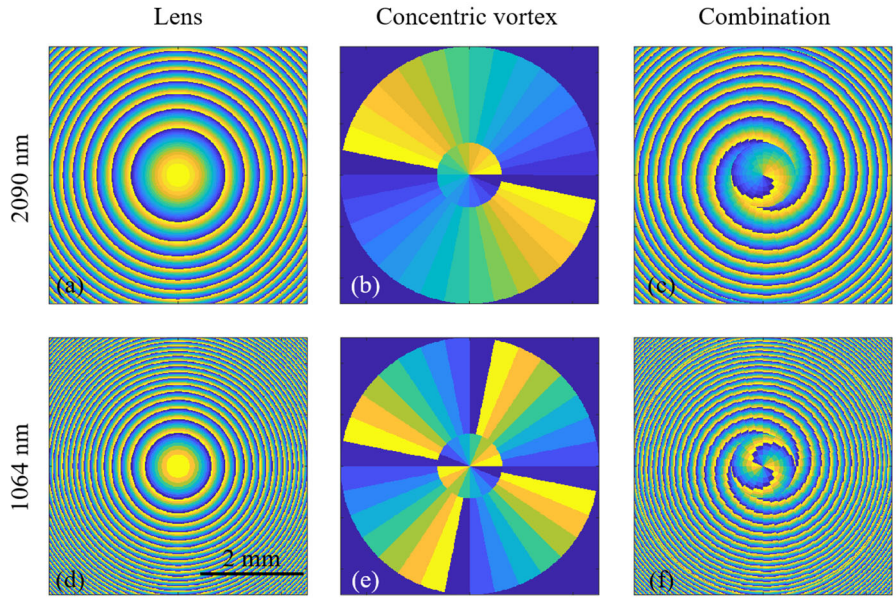

Fig. 2.9. The simulated multi-harmonic lens (left column), concentric vortex (central column), and the combination phase (right column). Phase profile for 2090 nm (a) lens, (b) concentric vortex with $m_{in} = 1$, $m_{out} = -2$, and (c) the combination of (a) and (b). Phase profile for 1064 nm (d) lens, (e) concentric SPP with $m_{in} = 2$, $m_{out} = -4$, and (f) the combination of (d) and (e).

Comparing Fig. 2.9 (a) and (d), it's obvious that the lens' phase profile gradient of the 1064 nm beam is faster than that of the 2090 nm beam. When the 1064 nm beam encounters the same harmonic diffractive lens, the focus will be one half of the 2090 nm

beam's focal length, as shown in Fig. 2.10. The z dimension's unit is the 2090 nm beam's diffractive lens's focal length.

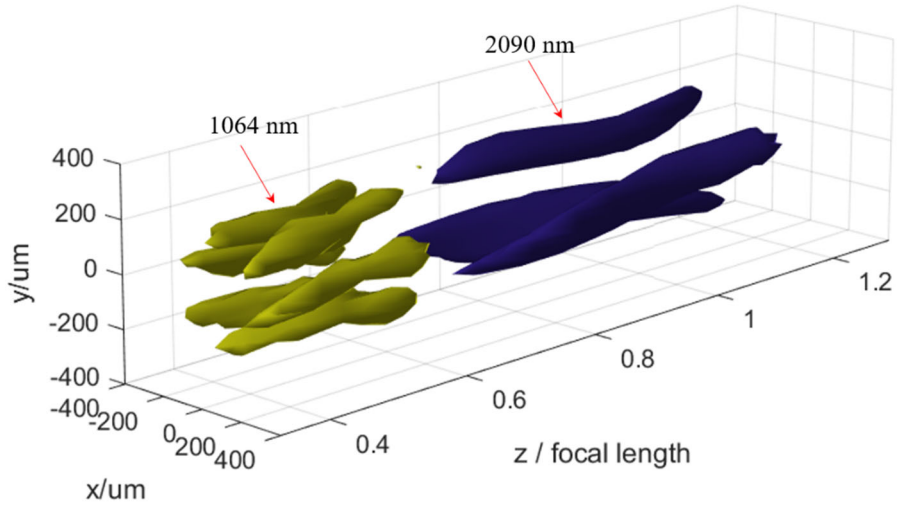

Fig. 2.10. The iso-surface of the intensity profile in 3-dimensions of both the 2090 nm beam and the 1064 nm beam, using the phase profile in Fig. 9 (c) and (f), respectively.

The concentric SPP beam's high peak intensity could be applied to generate helical filament [36]. In this multi-harmonic lens case, the filamentations are cascaded. This could benefit the long-range filamentation generation and control.

2.8 Conclusion

In conclusion, this chapter presented a unique OAM combination element, namely the concentric SPP. The general binary diffractive SPP's OAM spectrum has been derived by using the Fourier series theory. The three essential factors affecting the OAM spectrum are the scaled charge number $m_\lambda = \alpha m_{\lambda_0}$ corresponding with input wavelength λ, the

number of branch cuts $\left|m_{\lambda_0}\right|$, and the number of steps between branch cuts N. The OAM spectrum at harmonic wavelength has the maximized efficiency. The 1st harmonic order is the highest. The branch cut number $\left|m_{\lambda_0}\right|$ determines the empty OAM mode orders. The more the step number N, the tighter the OAM spectrum. The smooth SPP is the special case of binary SPP when $N \to \infty$. There are two sets of harmonics in the binary SPP: wavelength harmonic and OAM harmonic. The diffractive efficiency centers at the harmonic wavelengths and continuously decays in the sinc-squared function. For the OAM harmonic, the diffractive efficiency only exists in the harmonic channels. The nonharmonic channels are all empty. By applying the multiple harmonic design, the concentric SPP's first two diffraction orders' diffraction efficiency has been maximized. Therefore, this single concentric SPP could modulate the spectrally combined laser's OAM mode. The propagation dynamic of a concentric SPP due to the Gouy phase has been analytically well predicted and confirmed by the experiment. The mathematical model of a Gaussian beam modulated by a concentric SPP has been theoretically analyzed and experimentally demonstrated. Both the Fresnel transformation and single-lens Fraunhofer diffraction have been derived. The resulting beam is the interference of hypergeometric Gaussian beams with the aperture effect represented by incomplete gamma functions.

As a proof of concept, an experiment has been performed to demonstrate the simultaneous generation of vortices at two harmonic wavelengths, 2090 nm and 1064 nm, using a single concentric SPP. The diffraction patterns were petal-like intensity distributions in the far-field. The petal-like shapes rotate along the propagation direction after passing through a Fourier lens before, during, and after the focus. The rotation is

caused by the Gouy phase difference of the two OAM modes, and the rotation rate is derived and experimentally confirmed as inversely proportional to the interference fringes. The measured diffraction efficiency of both 1064 nm and 2090 nm is 93% and 94% after compensating for Fresnel losses. In general, the propagation dynamic research provides the insights of multi-harmonic concentric vortex beam, which could find applications in spectral-beam combination's OAM modulation, underwater/free-space communication, laser mode amplification, higher-order concentric vortex beam SHG, particle manipulation, filamentation control, and directed energy.

CHAPTER THREE

FRACTIONAL OAM AND ASYMMETRIC BESSEL GAUSS BEAM

3.1 Introduction

Integer OAM is easy to understand and well-studied. Fractional OAM is a natural extension of the integer OAM concept but still has many debatable topics: Is the fractional OAM exist? What's the nature of fractional OAM? What's the outcoming property that fractional OAM has comparing with integer OAM? What applications can the fractional OAM develop or improve? This chapter will try to answer these questions and give more insight into the fractional OAM topic.

In 2004, Berry studied the fundamental fractional charge spiral phase structure using the Fourier series expansion method [2]. This method is the main contribution to the fractional OAM research, and it is also the most commonly used tool to reveal the relationship between regular integer OAM and fractional OAM [3-7]. More interestingly, the fractional OAM beam is a physical demonstration of the mathematical "Hilbert Hotel" mechanism either in phase singularity [4] or polarization singularity [5]. Fractional OAM modes are also referred to as non-integer [3], continuous [53], successive [53], and rational [54] modes. It is an exciting aspect of study primarily because it is almost impossible to generate an entirely pure integer OAM state due to the inevitable defect of OAM generation elements. Secondly, it has been analytically deduced that fractional OAM Bessel beams could form an infinite number of orthogonal subsets of OAM modes [55], which can further benefit classical and quantum optical communication. Thirdly, the fractional OAM Bessel beams preserve the nondiffracting properties that integer OAM beams possess [53]. This

property is vital for beam propagation applications, including propagation through turbulence and turbid environments [56]. Moreover, it has been found that a group of fractional OAM modes generated by a synthesis of Laguerre-Gaussian (LG) modes have good structural stability on propagation to the far-field [57]. These LG mode-based fractional OAM states can be used in classical and quantum communication [58]. The fractional OAM structure has been used in turbulence research [56, 59]. A partially coherent fractional vortex beam has been studied [60]. The propagation property of these groups of beams has been revealed.

There are several ways to generate fractional OAM beams, such as fractional wrap spiral phase modulation [2, 58, 61], continuously shift SLM's fork-shaped hologram [62-64], combine the phase front of several integer charged OAM beams to form an OAM spectrum [23, 57, 65], log-polar optical geometric transformation to transform linear phase into fractional OAM phase [8], introducing new singularity into the light field to weight the integer charge into fractional charge [54], and or shift the singularity off away from the beam's axis [66]. The off-axis displaced singularity gives the charge number modulated by $m\exp\left(-\frac{2r_0^{\,2}}{w^2}\right)$, where m is the topological charge of the designed SPP, r_0 is the dislocation of the singularity from the beam center, w is the Gaussian's $1/e^2$ beam radius. The total charge number of the whole Gaussian beam is continuously tuned from 0 (singularity infinitely far away from the Gaussian's axis, Gaussian beam only sees a slow linear phase) to m (singularity overlap with the Gaussian's axis, regular integer charge Kummer beam). In the opposite of the case of fractional charge number always smaller than the designed

integer charge, always consider positive handedness at this point, Kotlyar's asymmetric Bessel Gaussian beam [23] has a tunable fractional charge number always greater than the designed integer charge. The comparison of log-polar optical geometric transformation generated asymmetric Bessel Gaussian beam with Kotlyat's asymmetric Bessel-Gauss beam will be addressed in section 3.6.

3.2 Plane-wave go through SPP to generate fractional OAM

The SPP is an efficient and robust way to generate optical vortices, including fractional OAM. The plane wave and Gaussian beam's paraxial Fresnel and Fraunhofer diffraction by SPP have been studied. The most vital work of the analysis of the fractional OAM of a plane wave was conduction by M Berry [2]. Due to the reason of propagation wave must be smooth, the initial phase discontinuity caused by the fractional charge number m on SPP must be smooth out along the propagation. The original phase singularity will separate into several singularities around the original phase singularity's transverse location. The original phase discontinuity evolves into a chain of singularities. The closer the charge number approaches to the half-integer, the obvious the chain. And more interestingly, this phenomenon is exact a physical demonstration of a mathematic concept of Hilbert's Hotel [4]. Given the arbitrary charge number of $m = l + \alpha$, where m is a continuous charge number, l is the integer part of m, and α is the fractional part. To avoid confusion, we define α as a positive real number $0 \leq \alpha < 1$. The decomposition of fractional singularity can be mathematically described as a combination or superposition of integer singularities. Namely, the well-known OAM phase term $\exp(jm\phi)$ can be expressed as a Fourier series [2, 4]:

$$\exp\left(\mathrm{j}m\phi\right)=\frac{\exp\left(\mathrm{j}\pi m\right)\sin\left(\pi m\right)}{\pi}\sum_{n=-\infty}^{\infty}\frac{\exp\left(\mathrm{j}n\phi\right)}{m-n}. \tag{3.1}$$

For and arbitrary scaler form a complex field $U_n\left(\mathbf{r}\right)$ carrying integer OAM *n*, the fractional charge field can be expressed as

$$U_m\left(\mathbf{r}\right)=\frac{\exp\left(\mathrm{j}\pi m\right)\sin\left(\pi m\right)}{\pi}\sum_{n=-\infty}^{\infty}\frac{U_n\left(\mathbf{r}\right)}{m-n}. \tag{3.2}$$

where $\mathbf{r}$ is the vector form of cylindrical coordinate. Due to the most common optical components are circular symmetric. A finite-size plane wave can be described as a circular aperture function:

$$U_n\left(\boldsymbol{\rho}\right)=\mathrm{circ}\left(\frac{\rho}{\rho_{\mathrm{SPP}}}\right)\exp\left(\mathrm{j}n\phi\right), \tag{3.3}$$

where ρ_{SPP} is the finite radius of the circular aperture, $\boldsymbol{\rho}$ is the vector form of cylindrical coordinate in the input plane. The Fresnel transform of the charge *m* finite apertured plane wave $U_n\left(\boldsymbol{\rho}\right)$ in polar coordinates is given by

$$\begin{aligned}U_{\mathrm{Fresnel}}\left(r,\theta,z\right)=&\frac{\exp\left(\dfrac{\mathrm{j}2\pi z}{\lambda}+\dfrac{\mathrm{j}\pi}{\lambda z}r^2\right)}{\mathrm{j}\lambda z}\\&\cdot\int_0^{2\pi}\int_0^{\rho_{\mathrm{SPP}}}\exp\left(\frac{\mathrm{j}\pi\rho^2}{\lambda z}\right)\exp\left[\mathrm{j}n\phi-\mathrm{j}\frac{2\pi}{\lambda z}\rho r\cos\left(\theta-\phi\right)\right]\rho\mathrm{d}\rho\mathrm{d}\phi,\end{aligned} \tag{3.4}$$

where *r* and θ are the polar coordinates of the transformed field, and *z* is propagation distance. According to the general two-dimensional polar coordinate Fourier transforms integration method in [50], Eq. (3.4) will reduce to

$$U_{\mathrm{Fresnel}}\left(r,\theta,z\right)=\frac{2\pi}{\mathrm{j}\lambda z}\exp\left(\mathrm{j}\frac{2\pi z}{\lambda}+\mathrm{j}\frac{\pi}{\lambda z}r^2+\mathrm{j}n\theta\right)\int_0^{\rho_{\mathrm{SPP}}}\exp\left(\frac{\mathrm{j}\pi\rho^2}{\lambda z}\right)J_n\left(\frac{2\pi}{\lambda z}r\rho\right)\rho\mathrm{d}\rho, \tag{3.5}$$

where $J_n(\cdot)$ is the Bessel function of the first kind of the *n*-th order. The Eq. (3.5) has been solved as [46, 47, 67]

$$U_{\text{Fresnel}}(r,\theta,z) = 2\exp\left(\mathrm{j}\frac{z_0}{z}\overline{r}^2 + \mathrm{j}n\theta\right)\frac{\overline{r}^n}{n!}\left(\frac{-\mathrm{j}z_0}{z}\right)^{n+1} \cdot\sum_{k=0}^{\infty}\frac{\left(\frac{\mathrm{j}z_0}{z}\right)^m}{(2k+n+2)k!}{}_1F_2\left[\frac{2k+n+2}{2},\frac{2k+n+4}{2},n+1;-\left(\frac{z_0\overline{r}}{z}\right)^2\right] \tag{3.6}$$

where $z_0 = \dfrac{\pi\rho_{\text{SPP}}{}^2}{\lambda}$ is the Rayleigh range, $\overline{r} = \dfrac{r}{\rho_{\text{SPP}}}$ is the normalized radial parameter in cylindrical coordinate, ${}_1F_2(\cdot,\cdot,\cdot;\cdot)$ is a hypergeometric (HyG) function. Apparently, ρ_{SPP} is the aperture size parameter, at $\rho_{\text{SPP}} = 0$ the aperture closes, at $\rho_{\text{SPP}} \to \infty$ the aperture will be wide open and the resulting the Eq. (3.6) reduce to [4]

$$U_{\text{Fresnel}}(r,\theta,z) = \exp\left(\mathrm{j}\frac{2\pi z}{\lambda} + \mathrm{j}\frac{\pi}{2\lambda z}r^2 + \mathrm{j}n\theta\right)\sqrt{\frac{\pi}{8}}(-\mathrm{j})^{\frac{n}{2}}\sqrt{\frac{2\pi}{\lambda z}r^2} \cdot\left[J_{\frac{n-1}{2}}\left(\frac{\pi}{2\lambda z}r^2\right) - \mathrm{j}J_{\frac{n+1}{2}}\left(\frac{\pi}{2\lambda z}r^2\right)\right]. \tag{3.7}$$

Fraunhofer diffraction is the far-field case of Fresnel diffraction at $z \to \infty$ or the complex distribution in the rear focal plane of an ideal spherical lens. Considering removing the parabolic phase term $\exp\left(\dfrac{\mathrm{j}\pi\rho^2}{\lambda z}\right)$ in the integral of Eq. (3.4), omitting the insignificant propagation phase $\exp\left(\mathrm{j}\dfrac{2\pi z}{\lambda}\right)$ and parabolic phase $\exp\left(\mathrm{j}\dfrac{\pi}{\lambda z}r^2\right)$, the finite apertured plane wave's Fraunhofer diffraction at the rear focal plane is given [47, 67]

$$U_{\text{Fraunhofer}}(r,\theta)=\frac{(-\mathrm{j})^{n+1}\exp(\mathrm{j}n\theta)}{(n+2)n!}\left(\frac{2\pi{\rho_{\text{SPP}}}^2}{\lambda f}\right)\left(\frac{\pi\rho_{\text{SPP}}r}{\lambda f}\right)^n \cdot {}_1F_2\left[\frac{n+2}{2},\frac{n+4}{2},n+1;-\left(\frac{\pi\rho_{\text{SPP}}r}{\lambda f}\right)^2\right], \tag{3.8}$$

where f is the focal length of the ideal spherical lens.

Given the integer charged scaler form diffraction expression, the fractional charge scaler form diffraction expression can be expressed by applying the general case equation Eq. (3.2). It's noticeable that plane wave is always the most simplified ideal wave model, but in reality, the more practical beam is the Gaussian beam. As long as the working distance is smaller than the Rayleigh range, the Gaussian beam should be a proper approximation of plane waves.

3.3 Gaussian go through SPP to generate fractional OAM

The Gaussian beam is the fundamental mode of modern optical science and engineering, and its property has been well studied. As working in the collimated range or Rayleigh range, the Gaussian beam's wavefront is approximated flat. That's a fair approximation of plane wave phase front, which was mentioned in section 3.2 if the Gaussian intensity distribution is neglected. It's essential to know the propagation property of the Gaussian beam modulated by the vortex SPP. Given the general relationship between the fraction charged scaler beam and integer charged scaler beam in Eq. (3.2), the fractional OAM mode generated by the Gaussian beam passes through fractional vortex SPP could be developed once having the integer charge vortex Gaussian beam's diffraction derived.

Consider the scaler form paraxial Fresnel diffraction of Gaussian beam at the waist position as

$$U_{\text{Fresnel}}(r,\theta,z)=\frac{\exp\left(\frac{\mathrm{j}2\pi z}{\lambda}+\frac{\mathrm{j}\pi}{\lambda z}r^2\right)}{\mathrm{j}\lambda z}\cdot\int_0^{2\pi}\int_0^{\infty}\exp\left(-\frac{\rho^2}{w_0{}^2}+\frac{\mathrm{j}\pi\rho^2}{\lambda z}\right)\exp\left[\mathrm{j}n\phi-\mathrm{j}\frac{2\pi}{\lambda z}\rho r\cos(\theta-\phi)\right]\rho\mathrm{d}\rho\mathrm{d}\phi. \tag{3.9}$$

where w_0 is the Gaussian beam waist radius. Apply the same method, according to the general two-dimensional polar coordinate Fourier transforms integration method in [50], Eq. (3.9) will reduce to

$$U_{\text{Fresnel}}(r,\theta,z)=\frac{2\pi}{\mathrm{j}\lambda z}\exp\left(\mathrm{j}\frac{2\pi z}{\lambda}+\mathrm{j}\frac{\pi}{\lambda z}r^2+\mathrm{j}n\theta\right)\int_0^{\infty}\left(-\frac{\rho^2}{w_0{}^2}+\frac{\mathrm{j}\pi\rho^2}{\lambda z}\right)J_n\left(\frac{2\pi}{\lambda z}r\rho\right)\rho\mathrm{d}\rho. \tag{3.10}$$

Refer to the integral solution 6.631.7 from [51]

$$\int_0^{\infty}x\exp\left(-ax^n\right)J_\nu(bx)\mathrm{d}x=\frac{\sqrt{\pi}b}{8a^{\frac{3}{2}}}\exp\left(-\frac{b^2}{8a}\right)\left[I_{\frac{\nu-1}{2}}\left(\frac{b^2}{8a}\right)-I_{\frac{\nu+1}{2}}\left(\frac{b^2}{8a}\right)\right],\quad\left[\mathrm{Re}\,\nu>-2,\mathrm{Re}\,a>0\right], \tag{3.11}$$

where $I_\nu(\cdot)$ is the modified Bessel function of the first kind of order ν. Then Eq. (3.10) is solved as [47, 68, 69]

$$U_{\text{Fresnel}}(r,\theta,z)=\frac{(-\mathrm{j})^{n+1}\sqrt{\pi}}{2}\left(\frac{z_0}{z}\right)^2\left(\frac{r}{w_0}\right)\left[1+\left(\frac{z_0}{z}\right)^2\right]^{-\frac{3}{4}}\cdot\exp\left[-\frac{r^2}{w^2(z)}+\mathrm{j}\frac{3}{2}\arctan\left(\frac{z_0}{z}\right)-\mathrm{j}\frac{\pi}{\lambda}r^2\left(\frac{1}{R_0(z)}-\frac{1}{z}\right)+\mathrm{j}n\theta+\mathrm{j}\frac{2\pi z}{\lambda}\right]\left\{I_{\frac{n-1}{2}}\left[r^2\left(\frac{1}{w^2(z)}+\mathrm{j}\frac{\pi}{\lambda R_0(z)}\right)\right]-I_{\frac{n+1}{2}}\left[r^2\left(\frac{1}{w^2(z)}+\mathrm{j}\frac{\pi}{\lambda R_0(z)}\right)\right]\right\}, \tag{3.12}$$

where $z_0 = \frac{\pi w_0^{\,2}}{\lambda}$ is the Rayleigh range, $w^2(z) = 2w_0^{\,2}\left[1+\left(\frac{z}{z_0}\right)^2\right]$, $R_0(z) = 2z\left[1+\left(\frac{z}{z_0}\right)^2\right]$.

The modified Bessel function form is the most commonly used solution of the diffraction of the vortex Gaussian beam. Moreover, this diffraction field could be expressed in hypergeometric function or Kummer function (confluent hypergeometric function) form, so vortex Gaussian beam's diffraction field is also called hypergeometric Gaussian (HyGG) mode, which is also the solution of scalar Helmholtz paraxial wave equation [70].

At $z \to \infty\left(z \gg z_0\right)$, the Fresnel transform Eq. (3.12) evolves into the Fraunhofer diffraction of the integer charged SPP modulated Gaussian beam:

$$\begin{aligned} U_{\text{Fraunhofer}}\left(r,\theta,z\to\infty\right) = {} & \frac{\left(-\mathrm{j}\right)^{n+1}\sqrt{\pi}}{2}\left(\frac{z_0}{z}\right)^2\left(\frac{r}{w_0}\right)\left[1+\left(\frac{z_0}{z}\right)^2\right]^{-\frac{3}{4}} \\ & \cdot\exp\left[-\frac{r^2}{w^2(z)}+\mathrm{j}n\theta+\mathrm{j}\frac{2\pi z}{\lambda}\right] \\ & \cdot\left[I_{\frac{n-1}{2}}\left(\frac{r^2}{w^2(z)}\right)-I_{\frac{n+1}{2}}\left(\frac{r^2}{w^2(z)}\right)\right]. \end{aligned} \tag{3.13}$$

3.4 Total singularity strength

Due to there is no fractional singularity exist in the stable nature system, the fractional charge OAM always refers to the total singularity strength or total charge number. Because the light propagation will smooth phase step or discontinuity, the fractional charged vortex beam's singularity structure is not stable along with propagation, including the location and the strength. Even for integer charge number vortex, if the beam's azimuthal symmetry is not perfectly even, the higher charge singularity will break

into several ±1 singularities around the transverse optical axis. Then in this context, the topic of conservation of charge number or singularity strength is not applicable for the local fast-changing singularities. It makes more sense to talk about the total singularity strength conservation due to the momentum conservation law. The concept of total singularity strength [2] was also called by global OAM [71], normalized total OAM [25], total OAM [72], normalized OAM [25], average OAM [72], the mean value of OAM [24] for different researchers background reason. We will keep using average OAM in all the chapters for continuity, simplicity, and easy understanding reason.

Average OAM, m_{ave}, is defined as the integration of the z component of OAM density, $\mathbf{j}_z$, over the transverse plane then normalized by the total power:

$$m_{\text{ave}} = \frac{J_z}{W} = \frac{\int_0^{\infty}\int_0^{2\pi} j_z r dr d\phi}{\int_0^{\infty}\int_0^{2\pi} U_m^*(\rho,\phi,z)\cdot U_m(\rho,\phi,z) r dr d\phi}, \tag{3.14}$$

where J_z is the OAM projection along the z-direction optical axis, W is the total power of the complex field, U_m and U_m^* are scalar form complex field and the conjugate, $j_z = \left|\mathbf{j}\cdot\hat{z}\right|$ is OAM density projection along the z-direction, $\hat{z}$ is the z-direction unit vector. Eq. (3.14) is defined in the cylindrical coordinate. The OAM density, $\mathbf{j}$, is determined by the cross product of space vector $\mathbf{r} = x\hat{x} + y\hat{y} + z\hat{z}$ and linear momentum density, $\mathbf{p} = \varepsilon_0(\mathbf{E}\times\mathbf{B})$, through

$$\mathbf{j} = \mathbf{r}\times\mathbf{p}, \tag{3.15}$$

where $\hat{x}, \hat{y}$, and $\hat{z}$are the three-dimension unit vectors, ε_0 is the vacuum permittivity, $\mathbf{E}$ is the electric field, $\mathbf{B}$ is the magnetic field. Recall the definition of the Poynting vector $\mathbf{S} = c^2 \varepsilon_0 \left(\mathbf{E} \times \mathbf{B} \right)$, where c is the vacuum light speed. We have the linear momentum density and the Poynting vector related as $\mathbf{p} = \frac{\mathbf{S}}{c^2}$. Consider the time-average Poynting vector [73]

$$\mathbf{S} = c^2 \varepsilon_0 \left[\mathrm{Im}\left(\mathbf{E} \right) \times \mathrm{Im}\left(\mathbf{B} \right) \right] = \frac{c^2 \varepsilon_0}{4} \left(\mathbf{E} \times \mathbf{B}^* + \mathbf{E}^* \times \mathbf{B} \right), \tag{3.16}$$

$$S_x = \frac{\varepsilon_0 \omega}{4} \left(i \left(U_m \frac{\partial U_m^*}{\partial x} - U_m^* \frac{\partial U_m}{\partial x} \right) \right), \tag{3.17}$$

$$S_y = \frac{\varepsilon_0 \omega}{4} \left(i \left(U_m \frac{\partial U_m^*}{\partial y} - U_m^* \frac{\partial U_m}{\partial y} \right) \right), \tag{3.18}$$

$$S_z = \frac{\varepsilon_0 \omega \pi}{\lambda} \left| U_m \right|^2, \tag{3.19}$$

where ω is the angular frequency of the electromagnetic wave. Conclude all the relationships above, the OAM density along z-direction is

$$j_z = \left| \left(\mathbf{r} \times \frac{\mathbf{S}}{c^2} \right) \cdot \hat{z} \right| = \mathrm{Im}\left(x U_m^* \frac{\partial U_m}{\partial y} - y U_m^* \frac{\partial U_m}{\partial x} \right). \tag{3.20}$$

Substitute the Eq. (3.20) into the Eq. (3.14). The well-known average OAM defined in Cartesian coordinate is derived as

$$m_{\mathrm{ave}} = \frac{J_z}{W} = \frac{\int_0^\infty \int_0^\infty \mathrm{Im}\left(x U_m^*(x,y,z) \frac{\partial U_m(x,y,z)}{\partial y} - y U_m^*(x,y,z) \frac{\partial U_m(x,y,z)}{\partial x} \right) dxdy}{\int_0^\infty \int_0^\infty U_m^*(x,y,z) \cdot U_m(x,y,z)\, dxdy}. \tag{3.21}$$

The cylindrical coordinate's version of average OAM turns into

$$m_{\text{ave}} = \frac{J_z}{W} = \frac{\int_0^{\infty}\int_0^{2\pi} \text{Im}\left(U_m^*(\rho,\phi,z) \cdot \frac{\partial U_m(\rho,\phi,z)}{\partial \phi} \right) r dr d\phi}{\int_0^{\infty}\int_0^{2\pi} U_m^*(\rho,\phi,z) \cdot U_m(\rho,\phi,z) r dr d\phi}. \tag{3.22}$$

In 2004, M. Berry's famous paper has first time evaluated the fractional charged plane wave's average OAM (total singularity strength in the original paper), then numerically resolved the integration formula, concluded from the numerical result a simple, elegant form [2]

$$m_{\text{ave}} = \text{nearest integer to } m = \text{int}\left(m + \frac{1}{2} \right). \tag{3.23}$$

For a Gaussian beam carrying fractional OAM, the average OAM has been investigated from the quantum perspective [24] and the diffraction theory [25] base on the aforementioned Eq. (3.21)

$$m_{\text{ave}} = \frac{J_z}{W} = m - \frac{\sin(2\pi m)}{2\pi}. \tag{3.24}$$

The vortex plane wave and vortex Gaussian beams' average OAM are plotted in Fig. 3.1.

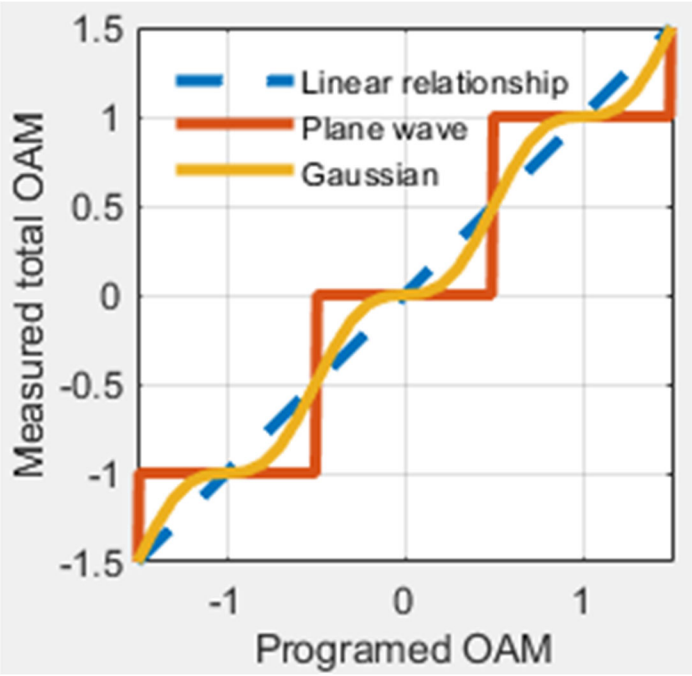

Fig. 3.1. A fractional vortex plane wave and fractional vortex Gaussian beams' average OAM are compared with the linear relationship.

Apparently, given any arbitrary complex field, the average OAM could be numerically computed based on Eq. (3.21). More importantly, by realizing the linear relationship between the wave vector and the linear momentum $p = \hbar \cdot \frac{2\pi}{\lambda}$, the average OAM could be indirectly measured by assessing the wave vector. Due to the wave vector and linear position are a Fourier conjugate pair, a single cylindrical lens method has been developed to measure the average OAM [72, 74]

$$m_{\text{ave}} = \frac{2\pi}{f\lambda}\left(\frac{\int_0^\infty\int_0^\infty I_m(x',y)\cdot x'ydx'dy}{\int_0^\infty\int_0^\infty I_m(x',y)dx'dy} - \frac{\int_0^\infty\int_0^\infty I_m(x,y')\cdot xy'dxdy'}{\int_0^\infty\int_0^\infty I_m(x,y')dxdy'}\right). \tag{3.25}$$

where the $I_m(x',y)$ is the intensity at the location (x',y), x' is the transformed horizontal coordinate, y is the vertical coordinate before Fourier transforms, and vice versa. Due to the cylindrical lens only do one dimensional Fourier transform, there is always one dimension coordinate keeps the same before and after the transform.

3.5 OAM spectrum and asymmetric fractional Bessel Gaussian beam

As the last two sections talked about, the average OAM, m_{ave}, of plane wave or Gaussian beam with initial fractional vortex phase, won't keep a linear relationship with the initial fractional charge number. So, in this sense, the average OAM does not conserve in free space propagation. The OAM must transform into spin angular momentum or linear momentum. To keep the OAM conservation law work for fractional OAM beam as how it works for integer OAM beams, we developed a way to generate a group of innovative beams that have fractional average OAM preserve along with free space propagation.

The fractional charge OAM is not conserved because the phase disconnection always tries to heal itself into a smooth continuous phase along with the propagation. And as Eq. (3.21) shows, the average OAM is weighted by the power/intensity of the local beam. Therefore, in the view of each local sector of the beam, the more intensity, the more the azimuthal phase gradient weight in the computation of average OAM and vice versa. We design a beam with the least power at the phase discontinuity location. The phase discontinuity still affects the average OAM, but not too much power support it to do so.

Meanwhile, the intensity distribution should be as smooth as possible to avoid Fourier transform's high-frequency response. Due to the Gaussian distribution's Fourier

transform is Gaussian, the Gaussian azimuthal intensity distribution's Fourier transform is the OAM spectrum, which is Gaussian distribution as well. The azimuthal Gaussian ring beam's intensity and fractional OAM phase are shown in Fig. 3.2.

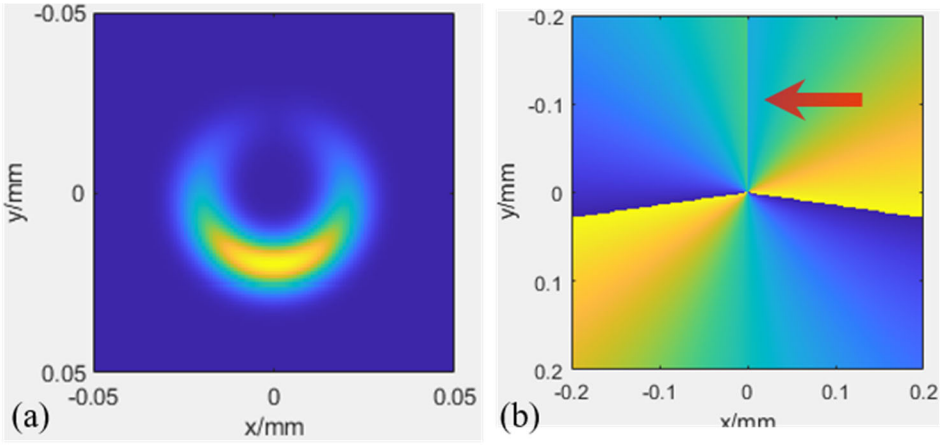

Fig. 3.2. Azimuthal Gaussian ring beams' (a) intensity and (b) fractional OAM phase. The red arrow indicates the azimuthal phase discontinuity.

The horizontal polarized azimuthal Gaussian ring, $\mathbf{U}_{\text{az-Gauss}}$, in polar coordinate, can be expressed as

$$\mathbf{U}_{\text{az-Gauss}}(\rho,\phi)=\hat{x}\exp\left[-\frac{(\rho-\rho_0)^2}{w_{\text{ring}}{}^2}\right]\cdot\exp\left[-\frac{\phi^2}{(\beta\pi)^2}+\text{j}m\phi\right] \tag{3.26}$$

where the (ρ,ϕ) is the polar coordinates, ρ_0 is the beam radius from the center of the beam to the ring peak intensity location, w_{ring} is the ring half size from the ring peak intensity location to the $\exp(-2)I_{\text{peak}}$ boundary, $\beta\in(0,1]$ is a tuning ratio, which determines the Gaussian ring's azimuthal size, it's possible that $\beta>1$, but in this case, there will be more than 9% power loss. According to the angular diffraction theory [75-

77], angular pattern diffracts into a discrete OAM spectrum. For the azimuthal Gaussian ring's case, the angular distribution is

$$\Psi(\phi)=\exp\left[-\frac{\phi^2}{(\beta\pi)^2}+\mathrm{j}m\phi\right]=\sum_{k=1}^{\infty}A_k\exp(\mathrm{j}k\phi), \tag{3.27}$$

$$A_k=\frac{1}{2\pi}\int_{-\pi}^{\pi}\Psi(\phi)\exp(-\mathrm{j}k\phi)\,d\phi=\frac{1}{2\pi}\int_{-\pi}^{\pi}\exp\left[-\frac{\phi^2}{(\beta\pi)^2}+\mathrm{j}m\phi\right]\exp(-\mathrm{j}k\phi)\,d\phi. \tag{3.28}$$

Refer to the integral solution 2.33.3 [51]

$$\int\exp(ax^2+bx+c)\,dx=\frac{1}{2}\sqrt{\frac{\pi}{a}}\exp\left(\frac{4ac-b^2}{4a}\right)\mathrm{erfi}\left(\sqrt{a}x+\frac{b}{2\sqrt{a}}\right),a\neq 0, \tag{3.29}$$

where the imaginary error function

$$\mathrm{erfi}(z)=\frac{\mathrm{erf}(\mathrm{j}z)}{\mathrm{j}}, \tag{3.30}$$

the Fourier coefficient A_k is solved

$$A_k=\frac{\beta\sqrt{\pi}}{2}\exp\left(-\frac{(\beta\pi(m-k))^2}{4}\right)\mathrm{Re}\left(\mathrm{erf}\left(-\frac{1}{\beta}+\mathrm{j}\frac{\beta\pi(m-k)}{2}\right)\right). \tag{3.31}$$

From the OAM spectrum perspective, the tuning ratio factor β is inversely related to the OAM spectrum bandwidth. The smaller the β, the wider the spectrum. One can tell from Eq. (3.31) that the OAM spectrum is a discrete function, which makes sense because its Fourier conjugate is a periodic function. More interestingly, the discrete value Gaussian function is modulated by a complex error function. It broadens the OAM spectrum a little bit but won't change the Gaussian envelop nature in general. Another intuitive way to explain the Fourier transform of the azimuthal Gaussian truncated by $(-\pi,\pi]$ aperture, it's

a convolution of a Gaussian with a sinc function [78]. This is the first time (to our knowledge) the azimuthal Gaussian's Fourier spectrum being solved, and more importantly, this exact solution works for fractional charge number's OAM spectrum also.

The Eq. (3.26) is the asymptotic form of the perfect vortex beam because the beam size is irrelevant to the charge number. Given a large degree of perfectness $\frac{\rho_0}{w_{\text{ring}}} \gg 1$ [79], we apply the asymptotic relation of modified Bessel function $I_m\left(\frac{2\rho_0\rho}{w_{\text{ring}}^2}\right) \sim \exp\left(\frac{2\rho_0\rho}{w_{\text{ring}}^2}\right)$ [79, 80], the Eq. (3.26) evolves into a more precise form of the perfect vortex

$$\mathbf{U}_{\text{PV}}(\rho,\phi) \propto \hat{x}\exp\left[-\frac{\rho^2+\rho_0^2}{w_{\text{ring}}^2}\right]\cdot I_m\left(\frac{2\rho_0\rho}{w_{\text{ring}}^2}\right)\exp\left[-\frac{\phi^2}{(\beta\pi)^2}+\text{j}m\phi\right], \tag{3.32}$$

where $I_m(\cdot)$ is the modified Bessel function of the first kind of order *m*. The Fourier transform of Eq. (3.32) is a superposition of a group of Bessel Gaussian function with the OAM spectrum coefficient depicted in Eq. (3.31). The OAM spectrum makes the Bessel Gaussian beam's azimuthal distribution nonuniform, so it's called an asymmetric Bessel Gaussian beam. It's worth pointing out that our asymmetric Bessel Gaussian beam is different from the first brought asymmetric Bessel Gaussian beam in 2014 [23], since the OAM spectra are designed differently. The systematical comparison will be addressed in section 3.6.

Other than using SLM coded phase profile to generate Kotlyar's asymmetric fractional Bessel Gaussian beam, we use log-polar optical geometric coordinate transformation diffractive optics to generate the angular spectrum of asymmetric fractional

Bessel Gaussian beam, which is a ring shape wrapped elliptical Gaussian beam into Eq. (3.26). Other techniques like multiplane light conversion (MPLC) can do this beam shaping also. In fact, the MPLC can generate more than 210 orthogonal LG modes (transformed from the corresponding HG modes) [81], but for efficiency consideration, the MPLC method utilizes too many phase elements. In contrast, the log-polar method only requires two elements. Spiral transform is developed base on the log-polar transform, but the mode symmetry and power efficiency need to be improved.

Once the beam is successfully generated, we propagate the asymmetric Bessel Gaussian beam a certain distance. The average OAM plot can be easily computed by using Eq. (3.21). From Fig. 3.3, it's obvious that the asymmetric Bessel Gaussian beam's average OAM is more linear than both the vortex plane wave and the vortex HyGG beam.

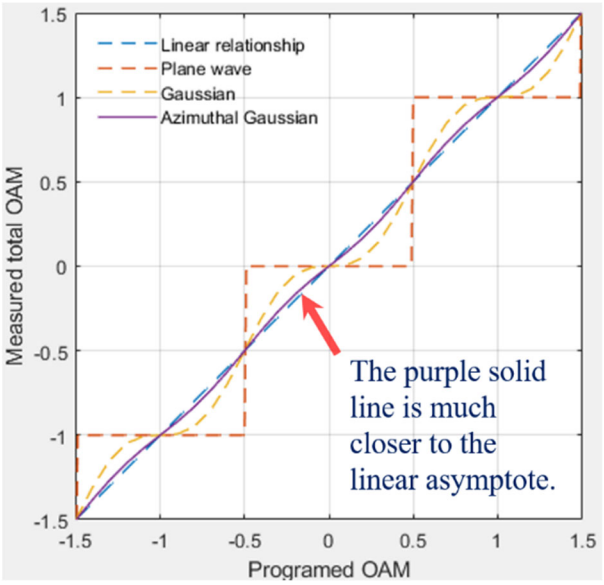

Fig. 3.3. Average OAM of vortex plane wave (red dash line), vortex HyGG (yellow dash line), and asymmetric Bessel Gaussian beam (solid purple line).

3.6 Comparison of the asymmetric Bessel Gaussian beams

We have mentioned that due to the OAM spectrum coefficient reason, our asymmetric Bessel Gaussian beam is different from the well known asymmetric Bessel Gaussian beam in Kotlyar's work [23]. We will compare these two cases in detail in this section. The Kotlyar version's asymmetric Bessel Gaussian beam has an elegant expression [23]:

$$U_{\mathrm{aBG\_K}}\left(r,\theta,z;c\right)=\sum_{p=0}^{\infty}\frac{c^{p}}{p!}\mathrm{BG}_{n+p}\left(r,\theta,z\right), \tag{3.33}$$

where asymmetry degree c is a positive real constant [65],

$$\mathrm{BG}_{n}\left(r,\theta,z\right)=\frac{1}{\mu\left(z\right)}\exp\left(\mathrm{j}kz-\frac{\mathrm{j}k_{\mathrm{t}}^{2}z}{2k\mu\left(z\right)}+\mathrm{j}n\theta-\frac{r^{2}}{w_{\mathrm{G}}^{2}\mu\left(z\right)}\right)J_{n}\left(\frac{k_{\mathrm{t}}r}{\mu\left(z\right)}\right), \tag{3.34}$$

is the propagation form of Bessel Gaussian beam at any location z, $\mu\left(z\right)=1+\frac{\mathrm{j}z}{z_{0}}$,

$z_{0}=\frac{kw_{\mathrm{G}}^{2}}{2}$ is the Rayleigh range, $k=\frac{2\pi}{\lambda}=\sqrt{k_{t}^{2}+k_{z}^{2}}$ is the wavenumber of the wavelength λ wave, $k_{t}=k\sin\varphi_{0}=\frac{2\pi\sin\varphi_{0}}{\lambda}$ is the transverse wavenumber, which is also the Bessel beam's scale factor, φ_{0} is the angle of the conical wave that forms the Bessel beam, w_{G} is the Gaussian envelop's waist radius, and $J_{n}\left(\cdot\right)$ is the Bessel function of the first kind of nth-order. The important parameter is the degree of perfectness $\frac{\rho_{0}}{w_{\mathrm{ring}}}$, as we mentioned in section 3.5, which is in a perfect vortex parameter. The equivalent Bessel Gaussian

parameter form degree of perfectness $\frac{k_{\mathrm{t}} w_{\mathrm{G}}}{2}$ can be obtained by applying perfect vortex to Bessel Gaussian parameter relationships $\rho_0 = \frac{k_{\mathrm{t}} f}{k}$ and $w_{\mathrm{ring}} = \frac{2f}{k w_{\mathrm{G}}}$ (the Gaussian beam's diffraction limit relation). On the contrary, the azimuthal Gaussian ring formed asymmetric Bessel Gaussian beam is

$$U_{\mathrm{aBG\_GR}}(r,\theta,z;\beta) = \sum_{p=-\infty}^{\infty} A_p \mathrm{BG}_p(r,\theta,z), \tag{3.35}$$

where the OAM spectrum coefficient

$$A_p = \frac{\beta\sqrt{\pi}}{2}\exp\left\{-\frac{\left[\beta\pi(m-p)\right]^2}{4}\right\}\mathrm{Re}\left\{\mathrm{erf}\left[-\frac{1}{\beta}+\mathrm{j}\frac{\beta\pi(m-p)}{2}\right]\right\} \tag{3.35}$$

is a complex constant, the azimuthal distribution of the angular spectrum of $U_{\mathrm{aBG\_GR}}(r,\theta,z;\beta)$ is a Gaussian distribution with azimuthal phase $\exp\left[-\frac{\phi^2}{(\beta\pi)^2}+\mathrm{j}m\phi\right]$, β represents the ratio of the azimuthal Gaussian distribution covering the whole $(-\pi,\pi]$ rang, $m = l+\alpha$ is a fractional charge number, l is the integer part of m, and α is the fractional part of m. The parameter β is similar to the $U_{\mathrm{aBG\_K}}(r,\theta,z;c)$'s asymmetry degree c, which controls the asymmetry of the Bessel Gaussian beam. The greater the asymmetry degree, the more asymmetry. When the asymmetry degree c = 0, the asymmetric Bessel Gaussian beam $U_{\mathrm{aBG\_K}}(r,\theta,z;c)$ returns to the regular Bessel Gaussian beam $\mathrm{BG}_n(r,\theta,z)$. For $U_{\mathrm{aBG\_GR}}(r,\theta,z;\beta)$ case, the asymmetry degree β controls the asymmetry in a different way. The greater the β, the more symmetric the beam. When

asymmetry degree $\beta \to \infty$, the asymmetric Bessel Gaussian beam $U_{\text{aBG\_GR}}\left(r,\theta,z;\beta\right)$ returns to the regular Bessel Gaussian beam $\text{BG}_n\left(r,\theta,z\right)$.

For the asymmetric Bessel Gaussian beams, either Kotlyar's version $U_{\text{aBG\_K}}\left(r,\theta,z;c\right)$ or azimuthal Gaussian ring version $U_{\text{aBG\_GR}}\left(r,\theta,z;\beta\right)$, there is four fundamental beam character determining parameters:

1) Degree of perfectness: $\frac{k_{\text{t}} w_{\text{G}}}{2}$ for both cases.

2) Degree of asymmetry: c for $U_{\text{aBG\_K}}\left(r,\theta,z;c\right)$ and β for $U_{\text{aBG\_GR}}\left(r,\theta,z;\beta\right)$.

3) OAM spectrum coefficient: $\frac{c^p}{p!}$ for $U_{\text{aBG\_K}}\left(r,\theta,z;c\right)$ and A_p (Eq. 3.35) for $U_{\text{aBG\_GR}}\left(r,\theta,z;\beta\right)$.

The degree of perfectness reflects the relationship between the Bessel term and the Gaussian term. To make a fair comparison, we will compare the degree of asymmetry's impact on intensity, phase, and OAM spectrum under the same degree of perfectness. In Fig. 1 of Kotlyar's paper [23], the degree of perfectness is $\frac{k_{\text{t}} w_{\text{G}}}{2} = 0.5$. The exact $U_{\text{aBG\_K}}\left(r,\theta,z=0;c\right)$ figure is replotted by utilizing the same degree of perfectness and degree of asymmetry c = 0.1, 1, 10, as shown in Fig. 3.4. Additionally, the normalized coefficients are also plotted to show the OAM spectrum. The intensity figure shows the asymmetry grows with the degree of asymmetry c, and a charge one singularity move approaching the original charge three singularity (n = 3). The normalized OAM spectrum confirms the increasing degree of asymmetry c. The spectrum broadens and shifts away

from the designed center charge number, n = 3, for example, in Fig. 3.4 (i). When the degree of asymmetry is approximately 0, as Fig. 3.4 (a) shows, the intensity approximately symmetric, (b) phase one n = 3 singularity, (c) spectrum only one spike at n = 3.

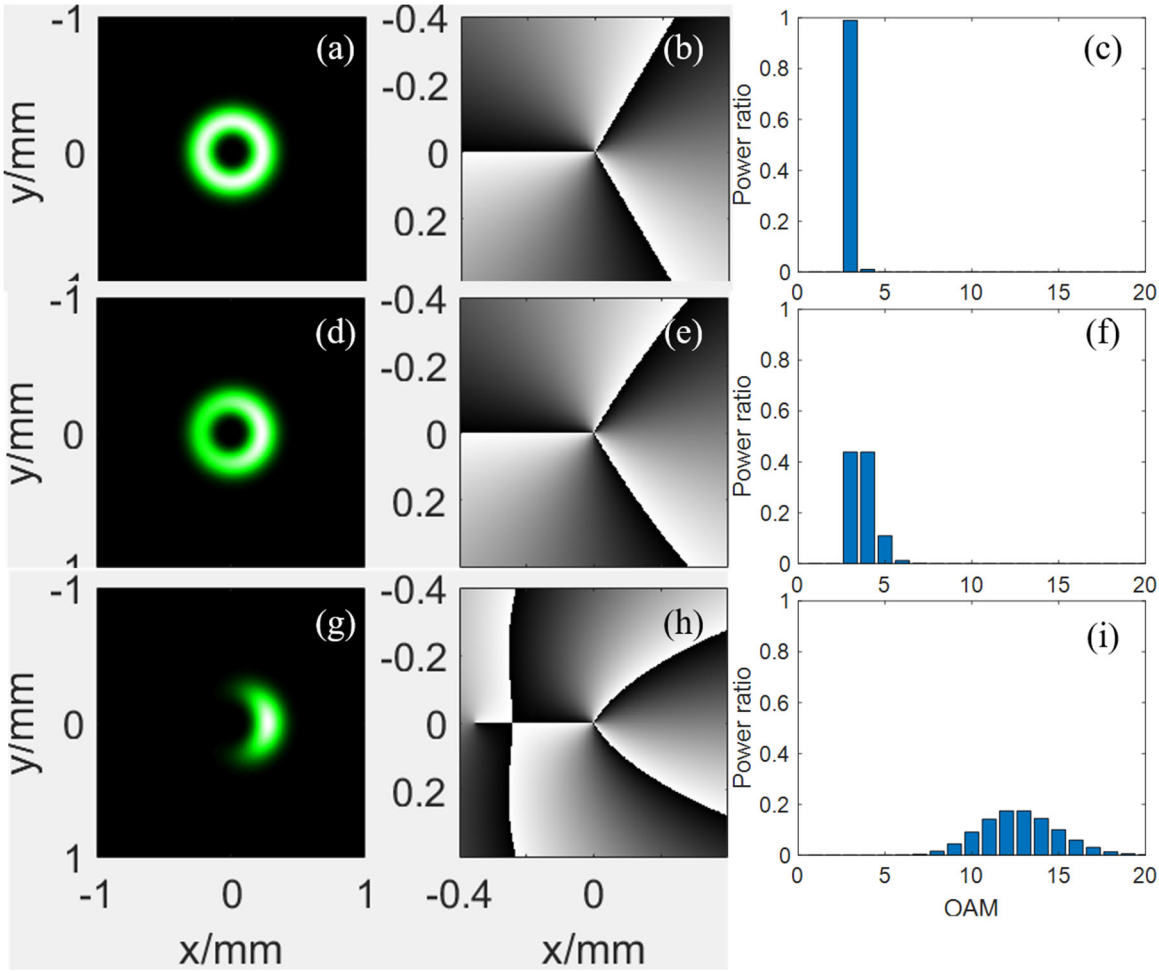

Fig. 3.4. (a), (d), (g) Intensity, (b), (e), (h) phase, and (c), (f), (i) normalized OAM spectrum coefficients from the Eq. 3.33 $U_{\mathrm{aBG\_K}}\left(r,\theta,z=0;c\right)$ at n = 3, and different asymmetric degree c: (a), (b), (c) 0.1; (d), (e), (f).1; and (g), (h), (i) 10.

The $U_{\text{aBG\_GR}}\left(r,\theta,z=0;\beta\right)$ degree of asymmetry β works differently from Fig. 3.4 $U_{\text{aBG\_K}}\left(r,\theta,z=0;c\right)$ cases. Under the same degree of perfectness $\frac{k_{\text{t}}w_{\text{G}}}{2}=0.5$, the asymmetry is shown in Fig. 3.5. The intensity figure shows the asymmetry grows reversely with the degree of asymmetry β, the origin charge three singularity (n = 3) split into charge two singularity and charge one singularity. As the asymmetry degree increases, the charge one singularity moves far away from the origin, as shown in Fig. 3.5 (e), (h), and (k). The charge two singularity split into two charge one singularities and departure aways from each other, as shown in Fig. 3.5 (h), (k), and (n). The normalized OAM spectrum confirms the increasing degree of asymmetry β, the spectrum broadens but keeps centering at the designed center charge number, n = 3, for example, in Fig. 3.5 (c), (f), (i), (l), and (o). When the degree of asymmetry is greater than 2, as Fig. 3.5 (a) shows, the intensity approximately symmetric, (b) phase one n = 3 singularity, (c) spectrum only one spike at n = 3. It's worth to notice that, under the same degree of perfectness, both $U_{\text{aBG\_K}}\left(r,\theta,z=0;c\right)$ and $U_{\text{aBG\_GR}}\left(r,\theta,z=0;\beta\right)$ have broad OAM spectrum with similar beam asymmetry. But the $U_{\text{aBG\_GR}}\left(r,\theta,z=0;\beta\right)$ beam's OAM spectrum is narrower than $U_{\text{aBG\_K}}\left(r,\theta,z=0;c\right)$ beam's; compare Fig. 3.4 (g) and (i) with Fig. 3.5 (m) and (o). For asymmetric degree β > 0.5, 5 to 7 central terms could represent the whole series pretty well because other terms converge to zero fast, shown as Fig. 3.4 (o). Another advantage of the $U_{\text{aBG\_GR}}\left(r,\theta,z=0;\beta\right)$ beam is the spectrum does not move with the degree of asymmetry β. On the contrary, the $U_{\text{aBG\_GR}}\left(r,\theta,z=0;\beta\right)$ beam's OAM spectrum shift

away from the initial Bessel beam's order towards higher charges with the increasing of asymmetry degree c. And that's how the $U_{\mathrm{aBG\_GR}}\left(r,\theta,z=0;\beta\right)$ beam resulting fractional charge numbers because the shifting is continuous.

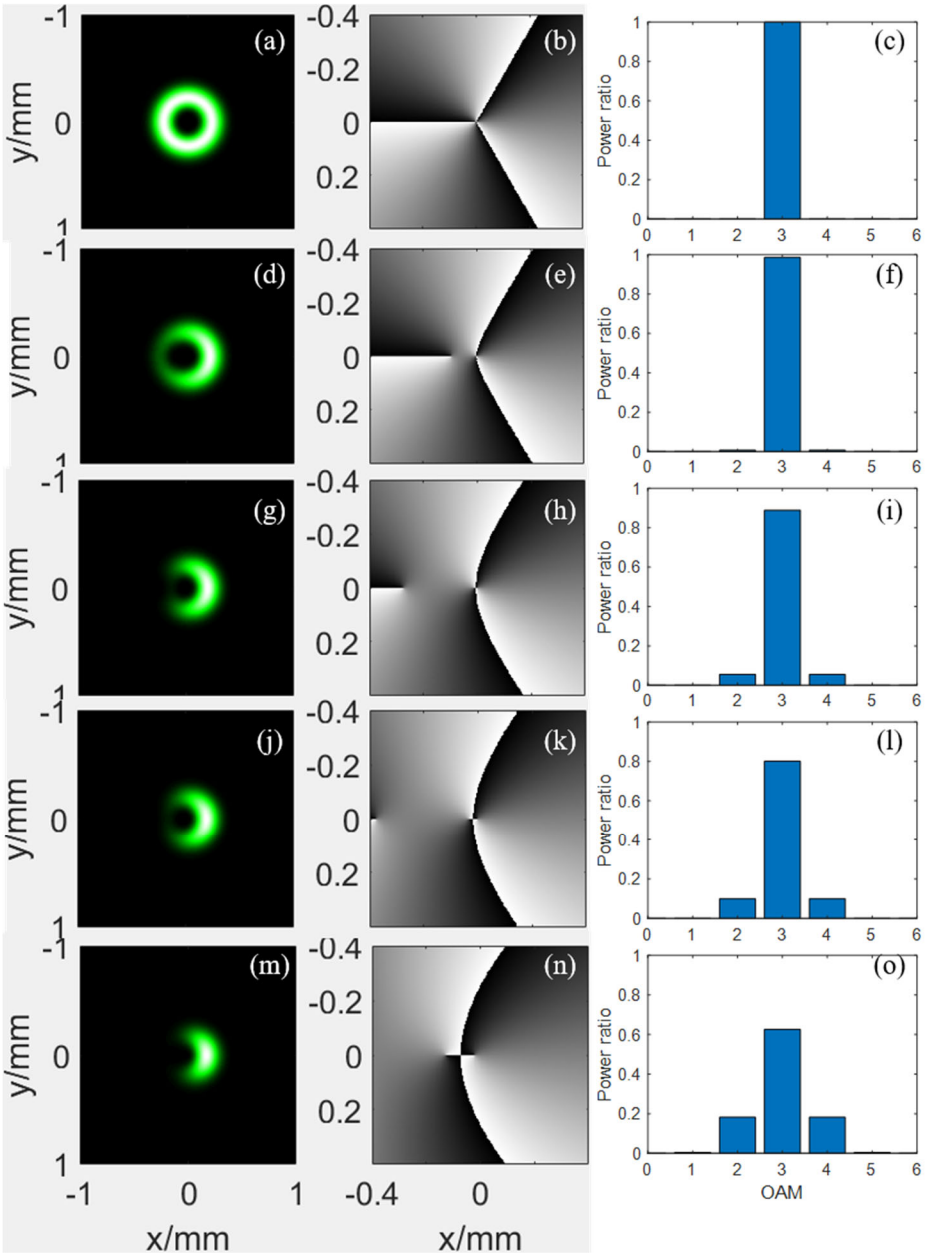

Fig. 3.5. (a), (d), (g), (j), (m) Intensity, (b), (e), (h), (k), (n) phase, and (c), (f), (i), (l), (o) normalized OAM spectrum coefficients from the Eq. 3.35 $U_{\mathrm{aBG\_GR}}\left(r,\theta,z=0;\beta\right)$ at n = 3, and different asymmetric degree β : (a), (b), (c) 2; (d), (e), (f).1; (g), (h), (i) 0.75; (j), (k), (l) 0.65, and (m), (n), (o) 0.5.

The degree of perfectness $\frac{k_{\mathrm{t}} w_{\mathrm{G}}}{2}$ does not contribute to the OAM spectrum of asymmetric Bessel Gaussian beams. As shown in Eq. 3.33 and 3.35, the OAM spectrums are solely determined by the degree of asymmetry either c or β . But the degree of perfectness does affect the Bessel Gaussian beams ringing effect, $U_{\mathrm{aBG\_K}}\left(r,\theta,z=0;c=1\right)$ is shown in Fig. 3.6, keeping the degree of asymmetry c = 1, the third-order aBG (n = 3), and the Gaussian envelope size w_{G}= 500 μm, tuning the degree of perfectness $\frac{k_{\mathrm{t}} w_{\mathrm{G}}}{2}$ = 0.5, 5, and 10.

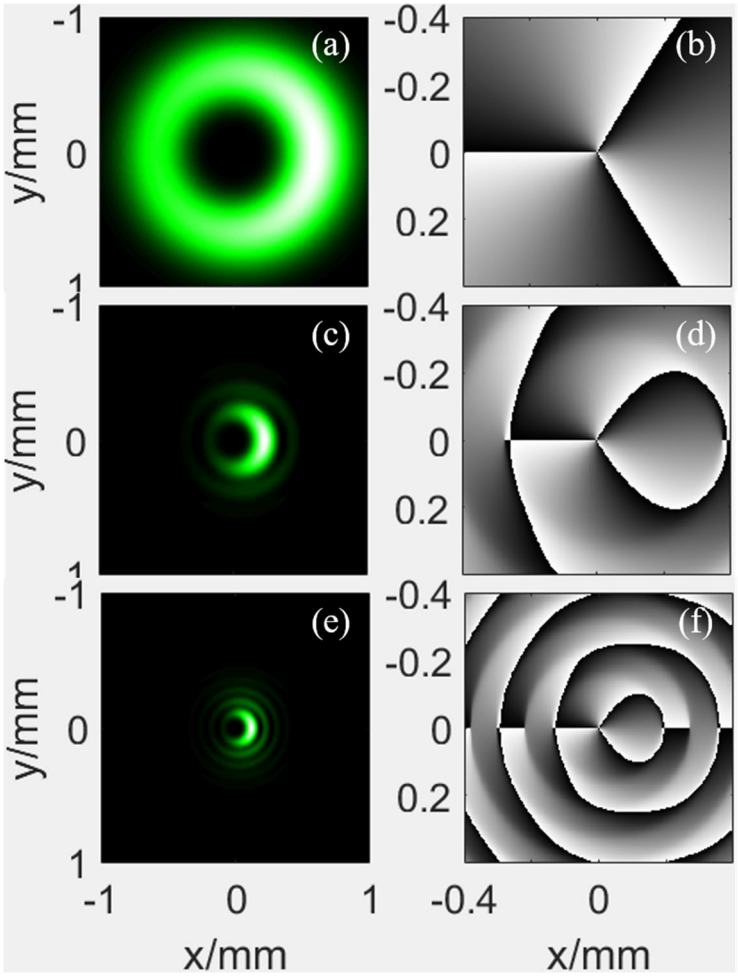

Fig. 3.6. (a), (c), (e) Intensity, and (b), (d), (f) phase, from the Eq. 3.33 $U_{\mathrm{aBG\_K}}\left(r,\theta,z=0;c=1\right)$ at n = 3, and different degree of perfectness $\frac{k_{\mathrm{t}}w_{\mathrm{G}}}{2}$: (a), (b), 0.5; (c), (d) 5; and (e), (f) 10.

Applying the same parameters to show $U_{\mathrm{aBG\_GR}}\left(r,\theta,z=0;\beta=1\right)$ in Fig. 3.7, keeping the degree of asymmetry β = 1, the third-order asymmetric Bessel Gaussian (n = 3), and the Gaussian envelope size w_{G}= 500 μm, tuning the degree of perfectness $\frac{k_{\mathrm{t}}w_{\mathrm{G}}}{2}$ = 0.5, 5, and 10.

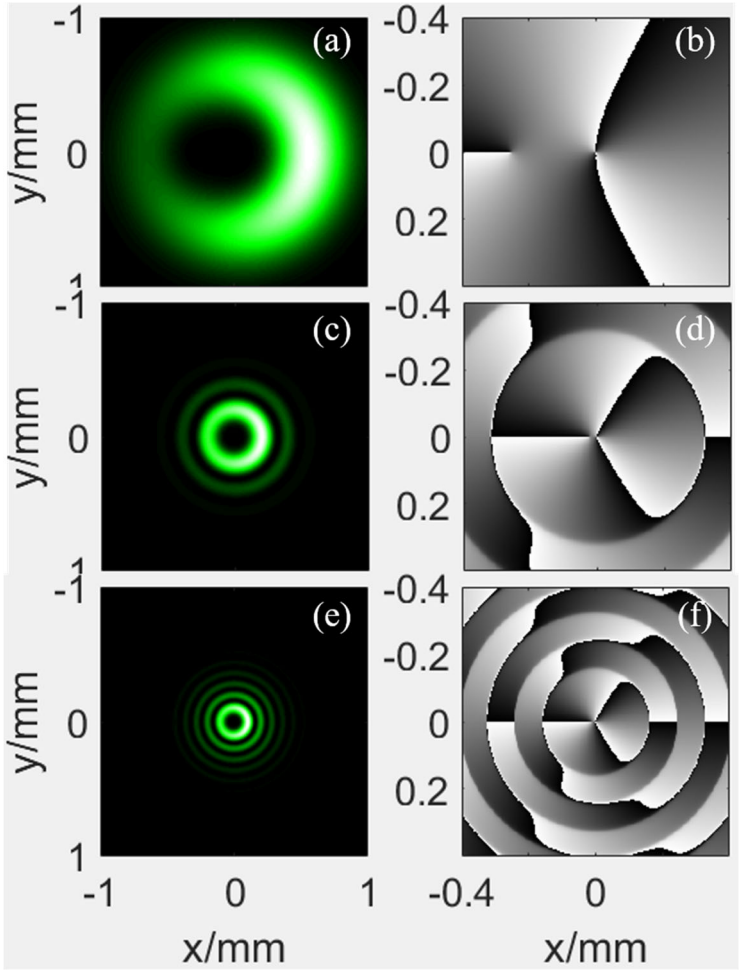

Fig. 3.7. (a), (c), (e) Intensity, and (b), (d), (f) phase, from the Eq. 3.33 $U_{\mathrm{aBG\_GR}}\left(r,\theta,z=0;\beta=1\right)$ at n = 3, and different degree of perfectness $\frac{k_{\mathrm{t}}w_{\mathrm{G}}}{2}$: (a), (b), 0.5; (c), (d) 5; and (e), (f) 10.

Compare Fig. 3.6 and 3.7, the degree of perfectness only controls the size ratio of the Gaussian envelope and the Bessel beam. It won't affect the asymmetry of the whole beam profile.

Last but not least is the fractional charge OAM generation capability of asymmetric Bessel Gaussian beams. Due to the OAM spectrum is solely determined by the degree of

asymmetry either in $U_{\text{aBG\_K}}(r,\theta,z;c)$ or $U_{\text{aBG\_GR}}(r,\theta,z;\beta)$. The fractional charge OAM generated by $U_{\text{aBG\_K}}(r,\theta,z;c)$ is approximately continuous but always greater than the initial Bessel beam's order, shown in Fig. 3.4 (c), (f), and (i). On the other hand, the $U_{\text{aBG\_GR}}(r,\theta,z;\beta)$ beam's spectra are always centered at the input continuous charge number $m = l + \alpha$. The $U_{\text{aBG\_GR}}(r,\theta,z;\beta = 0.5)$ beam's spectrum under different fractional m = 3, 3.3, 3.5, 3.9, and 4 are shown in Fig. 3.8.

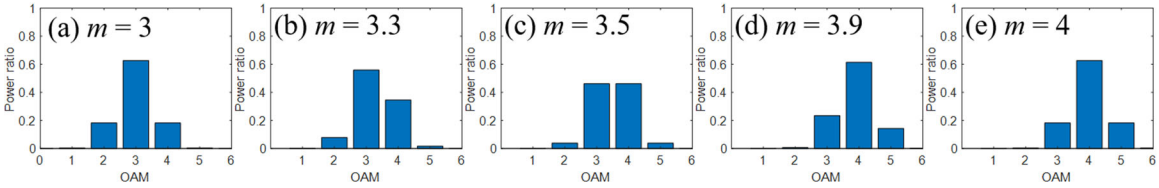

Fig. 3.8. OAM spectrum of $U_{\text{aBG\_GR}}(r,\theta,z;\beta = 0.5)$ at (a) m = 3, (b) 3.3, (c) 3.5, (d) 3.9, and (e) 4.

Above all, the asymmetry Bessel Gaussian beams $U_{\text{aBG\_K}}(r,\theta,z;c)$ and $U_{\text{aBG\_GR}}(r,\theta,z;\beta)$ are functionally similar to each other. Firstly, the degree of perfectness determines the ratio of the Gaussian envelop and the Bessel term size, shown in Fig. 3.6 and 3.7. Secondly, the degree of asymmetry affects the beam's asymmetry proportionally, shown in Fig. 3.4 and 3.5. The greater the asymmetry, the broader the OAM spectrum. Thirdly the $U_{\text{aBG\_K}}(r,\theta,z;c)$ generated fractional charge number is proportional to the degree of asymmetry c and always greater than the initial Bessel beam's order, shown in Fig. 3.4.(c), (f), and (i). The $U_{\text{aBG\_GR}}(r,\theta,z;\beta)$ beam's OAM spectra are always centered

at the initial charge number setting $m = l + \alpha$, and the fractional OAM is achievable through setting fractional *m*. Finally, the $U_{\text{aBG\_K}}(r,\theta,z;c)$ pattern asymmetry correlates with unit same sign singularity moving from outside towards the origin, shown as Fig. 3.4 (b), (e), and (h). The $U_{\text{aBG\_GR}}(r,\theta,z;\beta)$ pattern's asymmetry correlates with unit same sign singularity splitting from the higher-order singularity at the origin.

3.7 Contribution summary

In conclusion, this chapter is the theoretical foundation of the whole asymmetric fractional Bessel Gaussian beam research. The main contributions are concluded as such: we elaborated on the fractional OAM beam's average OAM conservation dilemma and systematically analyzed the vortex plane wave and vortex HyGG beam's Fresnel diffraction, Fraunhofer diffraction, and the average OAM equation. We reviewed the OAM density and average OAM's equation from the fundamental relation between OAM and linear moment. In the last section, by thoroughly analyzing the fractional OAM beam's phase profile problem, we proposed a novel fractional vortex beam with exemplary average OAM conservation, which is an asymmetric Bessel Gaussian beam. The OAM spectrum of the asymmetric Bessel Gaussian beam has been analyzed. And the Fourier conjugate of the asymmetric Bessel Gaussian beam is azimuthal Gaussian perfect vortex beam. Our azimuthal Gaussian ring evolved asymmetric fractional Bessel Gaussian beam $U_{\text{aBG\_GR}}(r,\theta,z;\beta)$ has been systematically compared with Kotlyar's asymmetric Bessel Gaussian beam $U_{\text{aBG\_K}}(r,\theta,z;c)$. The two kinds of asymmetric fractional Bessel Gaussian

beams are similar to each other, but $U_{\text{aBG\_K}}(r,\theta,z;c)$ have a broader and shifting OAM spectrum, $U_{\text{aBG\_GR}}(r,\theta,z;\beta)$ has relatively narrower and a center fixing OAM spectrum. Other than that, the generation of $U_{\text{aBG\_K}}(r,\theta,z;c)$ requires complex SLM coding, the log-polar optics could be used to generate $U_{\text{aBG\_GR}}(r,\theta,z;\beta)$ beams easily with high power efficiency. From the OAM spectrum perspective, the fractional OAM research is necessary because the modern OAM based communication technology is built on the OAM spectrum manipulation. The fractional OAM itself is a superposition of individual integer OAM modes.

CHAPTER FOUR

NEW LOG-POLAR DESIGN

4.1 Introduction

We generate a fractional asymmetric Bessel Gaussian beam by using a unique optical geometric log-polar transformation optics. To the state, the multi-plane light conversion (MPLC) [81] can generate a large number of orthogonal laser modes, but the tricky part is the more the modes involved, the more the phase elements are required. The number of phase elements soaring up could bring three direct puzzles. Firstly, the power efficiency will be hard to keep high. Secondly, the alignment will be challenged even if all the elements are precisely separated into two whole pieces. Thirdly, the MPLC method is essentially an iterative computation dense technique. The pro is that the computed phase elements could adaptively be refreshed according to the feedback of the input and output condition. Still, the con is that the phase elements are preferred to be recorded friendly, such as spatial light modulator (SLM), then most of the high power application is unavailable. High power endurable elements, such as fused-silica-based diffractive optics, only work for one-time design, and it could not be refreshed (here, refresh means change the phase design in real-time). So adaptivity and high power endurability are a pair of trade-offs. The log-polar transform is a family member of the geometrical coordinate transforms. It is applicable in the optical scenario because of the Fourier transform logic embedded in the physical optics. In 2013, Mirhosseini and co-workers innovatively cascaded fan-out elements following log-polar optics. Wan and co-workers have made log-polar optics fuse with fan-out design to increase the OAM mode sorter's resolution [18]. The concern of the

fan-out design comes from power efficiency due to the upper bound of the diffraction efficiency has been studied [82]. Power efficiency is a crucial aspect of the high power application. 2018 Wen and co-workers proposed the spiral log-polar transform [83] to expand the polar transform range from $[0, 2\pi)$ to $[0, \infty)$, then the OAM mode sorting resolution increases accordingly. Novel transform, such as *n*-fold circular-sector transform, is also grown from the traditional log-polar transform [21]. It improved the OAM channel separation without the fan-out design gets involved. More importantly, Ruffato and co-workers have pushed the log-polar transform family design from the paraxial region to the non-paraxial region [22]. Most of the relevant papers look at the demultiplexing or mode sorting part of the log-polar transform family. Few of them talk about the multiplexing or OAM generation part of the corresponding designs. Even a few do so, and barely any paper mentions power efficiently accomplish the mode generation. In this chapter, following the brief review of the log-polar transform, we will talk about the current popular design issue and find out a way to improve the design.

4.2 General optical geometric transformation

As early as 1974, Bryngdahl [12, 13] has developed a geometrical transformations method, which is also known as coordinate transformation [14] or coordinate mapping in the later relevant researches. The geometric transformations were first studied to process images, such as image registration, mapping, and object recognition.

Following Bryngdahl's method [12, 13], consider the Fourier transform relation between input U^{in} and output U^{out} light field

$$U^{\text{out}}(u,v) \approx -\frac{\mathrm{j}}{\lambda f}\int_{-\infty}^{\infty}\int_{-\infty}^{\infty} U^{\text{in}}(x,y)\exp\left\{\mathrm{j}\left[\Omega_{\text{transform}}(x,y)-\frac{2\pi}{\lambda f}(xu+yv)\right]\right\}\mathrm{d}x\mathrm{d}y \tag{4.1}$$

where (x,y) and (u,v) are the Cartesian coordinates of the input and output planes, λ is the wavelength, f is the Focal length, j is the imaginary unit, and $\Omega_{\text{transform}}$ is the desired transform phase profile. The Stationary phase approximation [84] or standard saddle-point method assumes the phase term in the integral is approximately a constant value in the (x,y) plane. The high oscillation phase's total contribution to the global integration will be zero due to a phasor is a periodic function. It means that the partial derivatives of the phase term should be zero:

$$\begin{cases} \dfrac{\partial\left[\Omega_{\text{transform}}(x,y)-\dfrac{2\pi}{\lambda f}(xu+yv)\right]}{\partial x}=0 \\ \dfrac{\partial\left[\Omega_{\text{transform}}(x,y)-\dfrac{2\pi}{\lambda f}(xu+yv)\right]}{\partial y}=0 \end{cases}. \tag{4.2}$$

The first-order partial derivatives of the desired phase are

$$\frac{\partial\Omega_{\text{transform}}(x,y)}{\partial x}=\frac{2\pi}{\lambda f}u, \tag{4.3}$$

$$\frac{\partial\Omega_{\text{transform}}(x,y)}{\partial y}=\frac{2\pi}{\lambda f}v. \tag{4.4}$$

For a general mapping relation from (x,y) to (u,v)

$$u(x,y)=\frac{\lambda f}{2\pi}\frac{\partial\Omega_{\text{transform}}(x,y)}{\partial x}, \tag{4.5}$$

$$v(x,y)=\frac{\lambda f}{2\pi}\frac{\partial\Omega_{\text{transform}}(x,y)}{\partial y}. \tag{4.6}$$

Once the mapping relation is clear, the desired phase $\Omega_{\text{transform}}(x,y)$ can be integrated from the Eqs. (4.3) and (4.4). But the solution only exists if and only if the mixed second-order partial derivatives of the desired phase $\Omega_{\text{transform}}(x,y)$ is the same (Schwarz's theorem)

$$\frac{\partial^2 \Omega_{\text{transform}}(x,y)}{\partial x \partial y} = \frac{\partial^2 \Omega_{\text{transform}}(x,y)}{\partial y \partial x}. \tag{4.7}$$

Substitute the mapping relations

$$\frac{\partial^2 \Omega_{\text{transform}}(x,y)}{\partial x \partial y} = \frac{\partial\left[\dfrac{\partial \Omega_{\text{transform}}(x,y)}{\partial x}\right]}{\partial y} = \frac{\partial\left[\dfrac{2\pi}{\lambda f}u\right]}{\partial y} = \frac{2\pi}{\lambda f}\frac{\partial u}{\partial y}, \tag{4.8}$$

$$\frac{\partial^2 \Omega_{\text{transform}}(x,y)}{\partial y \partial x} = \frac{\partial\left[\dfrac{\partial \Omega_{\text{transform}}(x,y)}{\partial y}\right]}{\partial x} = \frac{\partial\left[\dfrac{2\pi}{\lambda f}v\right]}{\partial x} = \frac{2\pi}{\lambda f}\frac{\partial v}{\partial x}, \tag{4.9}$$

The Eq. (4.7) is an equivalence of

$$\frac{\partial u(x,y)}{\partial y} = \frac{\partial v(x,y)}{\partial x}. \tag{4.10}$$

The Eq. (4.10) is the coordinate transformation's existence condition. Any transformation/mapping that satisfies this condition is called conformal mapping.

In general, given any form of coordinate transformation, the first existence test should be assessed by Eq. (4.10). Once the existence condition is satisfied, the desired phase profile $\Omega_{\text{transform}}(x,y)$ can be easily integrated from either Eq. (4.3) or Eq. (4.4).

$$\Omega_{\text{transform}}(x,y) = \iint \frac{\partial^2 \Omega_{\text{transform}}(x,y)}{\partial x \partial y}\mathrm{d}y\mathrm{d}x = \int \frac{\partial \Omega_{\text{transform}}(x,y)}{\partial x}\mathrm{d}x = \frac{2\pi}{\lambda f}\int u(x,y)\mathrm{d}x, \tag{4.11}$$

$$\Omega_{\text{transform}}(x,y) = \iint \frac{\partial^2 \Omega_{\text{transform}}(x,y)}{\partial y \partial x}\mathrm{d}y\mathrm{d}x = \int \frac{\partial \Omega_{\text{transform}}(x,y)}{\partial y}\mathrm{d}y = \frac{2\pi}{\lambda f}\int v(x,y)\mathrm{d}y. \tag{4.12}$$

There are mathematical intuitively basic transforms, such as the polar transform, which does not satisfy this conformal existence condition. Stuff and Cederquist have demonstrated that a two-step transformation could make any one-to-one transformation happen [85]. That means for any desired non-conformal transformation, a media state of transformation makes the input to media and media to output both possible conformal. Other than the existing condition, another important fact for the coordinate transformations is that the 2nd phase profile is always needed to cancel out the complex phase residual after a particular special plane. We can understand this phase element as a collimator at this point. Multiple complex phase element alignment is always a challenge in the lab realization.

4.3 Paraxial optical log-polar geometric transformation

In 1983, the log-polar transformation was brought out to realize the scale and rotation invariant correlation [15]. Modern log-polar transform optics was used to map the OAM beam's spiral phase/momentum to linear phase/momentum, then sort the OAM modes through a simple Fourier transform [16]. In 2013, Mirhosseini and co-workers cascaded fan-out optics after the log-polar elements to increase the mode sorter's separation efficiency [17]. In 2017, Wan and the co-workers used the same fan-out idea but integrated the fan-out phase and log-polar phase to reduce the total number of the phase elements [18]. Since 2017, Ruffato and co-workers have made endeavors to improve the miniaturization and alignment simplicity [19-21]. In 2019, Ruffato redesigned the log-polar elements to expand the paraxial transformation to the non-paraxial region [22]. The fundamental log-polar mapping relation is shown in Fig. 4.1.

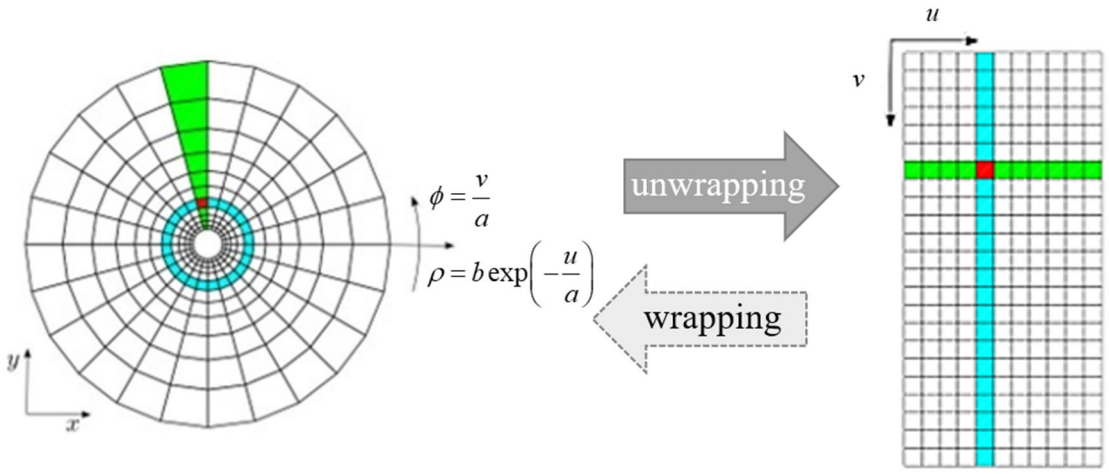

Fig. 4.1. The log-polar coordinates mapping from (x,y) to (u,v) unwraps a ring shape into a line, from (u,v) to (x,y) wraps a line shape into a ring.

As mentioned in the general geometric transform, a practical conformal mapping phase should be resolved after the existence test. Let us take a look at the log-polar mapping relation:

$$u(x,y) = -a\ln\left(\frac{\rho}{b}\right) = -a\ln\left(\frac{\sqrt{x^2+y^2}}{b}\right), \tag{4.13}$$

$$v(x,y) = a\phi = a\arctan 2(y,x). \tag{4.14}$$

where (ρ,ϕ) are the polar coordinates of (x,y), a and b are the log-polar scaling parameters determining the line length and the ring size. It is worth noting that the azimuthal polar coordinate ϕ has to be defined as the 2-argument arctangent because of its principal value in the range $(-\pi,\pi]$. The typical error that appears in most of the relevant log-polar papers is using the arctangent function to express the azimuthal polar coordinate,

which is mathematically wrong because the arctangent function's principal value is in the range $\left(-\frac{\pi}{2},\frac{\pi}{2}\right]$. Considering the existence condition Eq. (4.10),

$$\frac{\partial u(x,y)}{\partial y}=\frac{\partial v(x,y)}{\partial x}=\frac{-ay}{x^2+y^2}. \tag{4.15}$$

From here, the negative sign in Eq. (4.13) makes sense because this is the way to fulfill the conformal mapping requirement, though intuitively, the negative sign looks obscure at first sight. Substitute Eq. (4.13) into Eq. (4.11), or Eq. (4.14) into Eq. (4.12), the desired unwrapping phase can be integrated as

$$\Omega_{\mathrm{UN}}=\frac{2\pi a}{\lambda f}\left(y\arctan 2(y,x)-x\ln\left(\frac{\sqrt{x^2+y^2}}{b}\right)+x\right). \tag{4.16}$$

Considering the wrapping process in Fig. 4.1 from right to left, the mapping relations are

$$x(u,v)=\rho\cos(\phi)=b\exp\left(-\frac{u}{a}\right)\cos\left(\frac{v}{a}\right), \tag{4.17}$$

$$y(u,v)=\rho\sin(\phi)=b\exp\left(-\frac{u}{a}\right)\sin\left(\frac{v}{a}\right). \tag{4.18}$$

The conformal mapping existence was proven by Eq. (4.15). It's also easy to show

$$\frac{\partial x(u,v)}{\partial v}=\frac{\partial y(u,v)}{\partial u}=-\frac{b}{a}\exp\left(-\frac{u}{a}\right)\sin\left(\frac{v}{a}\right). \tag{4.19}$$

Applying the same process, the wrapper's phase profile could be integrated as

$$\Omega_{\mathrm{W}}=-\frac{2\pi ab}{\lambda f}\exp\left(-\frac{u}{a}\right)\cos\left(\frac{v}{a}\right). \tag{4.20}$$

The wrapping process setup and the two phases are shown in Fig. 4.2.

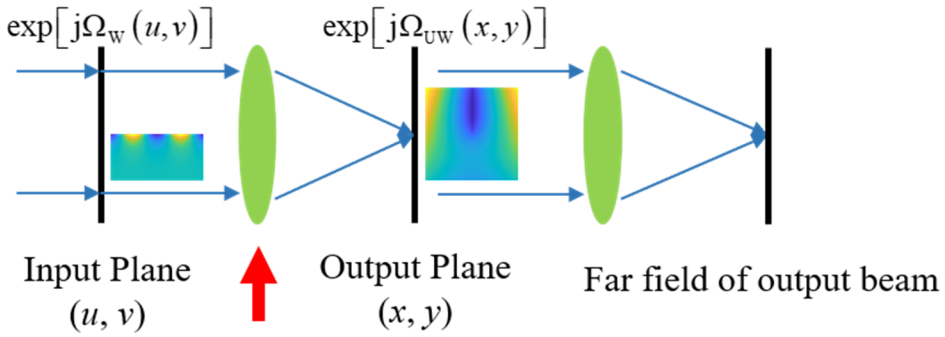

Fig. 4.2 The optical log-polar wrapping transformation setup from (u,v) to (x,y), the red arrow indicates the Fourier lens location.

To save the red arrow pointed Fourier lens from the whole setup, one could put an extra parabolic phase in the resolved phases as

$$\Omega_{\mathrm{W}} = -\frac{2\pi ab}{\lambda f}\exp\left(-\frac{u}{a}\right)\cos\left(\frac{v}{a}\right) - \frac{\pi}{\lambda f}\left(u^2+v^2\right), \tag{4.21}$$

$$\Omega_{\mathrm{UW}} = \frac{2\pi a}{\lambda f}\left[y\arctan 2\left(y,x\right) - x\ln\left(\frac{\sqrt{x^2+y^2}}{b}\right) + x\right] - \frac{\pi}{\lambda f}\left(x^2+y^2\right). \tag{4.22}$$

The modified wrapping process setup and the two phases depict by Eqs. (4.21) and (4.22) are shown in Fig. 4.3. The $\Omega_{\mathrm{W}}(u,v)$ wrapper's fast oscillating phase is smoothed by the parabolic phase, which is shown in Figs. 4.2, and 4.3. This is helpful for keeping diffractive optic's diffraction efficiency high.

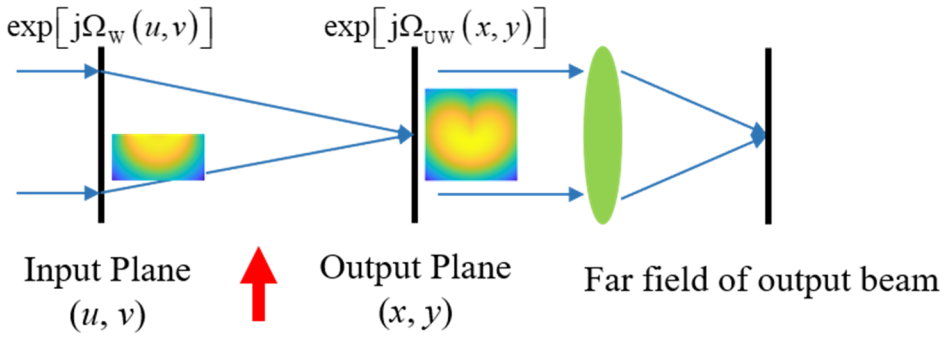

Fig. 4.3 The modified setup of optical log-polar wrapping transformation from (u,v) to (x,y), the red arrow indicates the Fourier lens location.

This operation does not break the conformal mapping criteria because the secondary mix partial derivatives of the parabolic phase are always the same. The wrapper phase and the unwrapped phase are phase residual corrector for each other. This is an analog of the conjugate relationship.

4.4 Conventional log-polar design's dilemma and five evaluation metrics

The sorted modes distortion induced by the skew OAM phase front has been noticed since the 2010 paper [16]. It is agreed that the log-polar theory assumes the wavevector goes straight, in which case the log-polar transformation works perfectly. But that is just the charge zero beam; even if the higher charge OAM beam's skew phase angle is small, the paraxial approximation comes into play, the distortion starts to accumulate. For the same reason, if we have the input as a line-shaped beam, the output will be a ring-shaped beam. Assume the log-polar maps the complex light field distribution. We expect a linear phase on the line shape maps into an OAM phase on the ring. The ideal log-polar wrapping process is shown in Fig. 4.4. But the truth is the linear input phase won't stay

there and do nothing. It will deflect the beam at a certain angle, which is agreed by both geometric optics and Fourier optics theory. This phenomenon is shown in Fig. 4.5. Eventually, this unexpected near field wrapped ring's shift will affect the average charge number both in the near-field and the far-field, and the far-field Bessel Gaussian beam's symmetry.

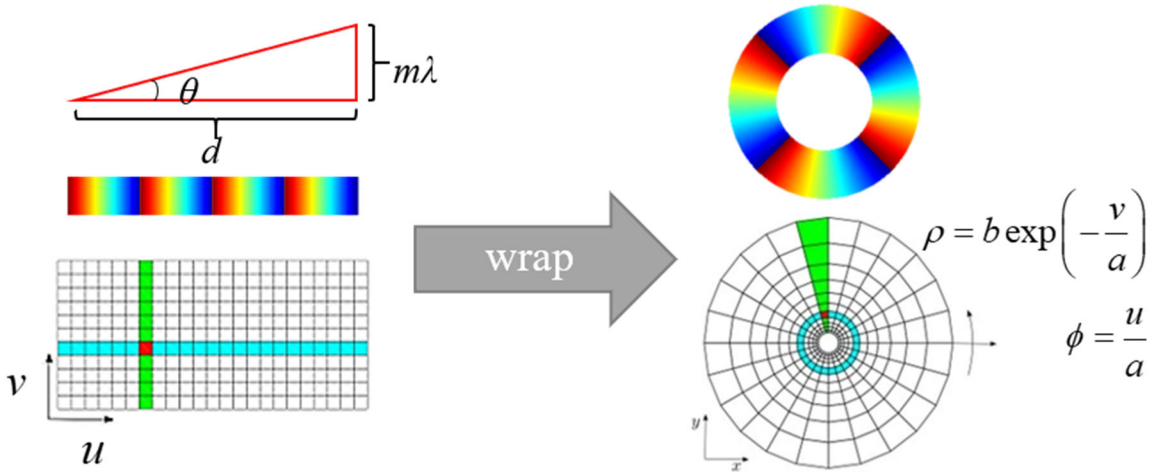

Fig. 4.4 Ideal log-polar wrapping process.

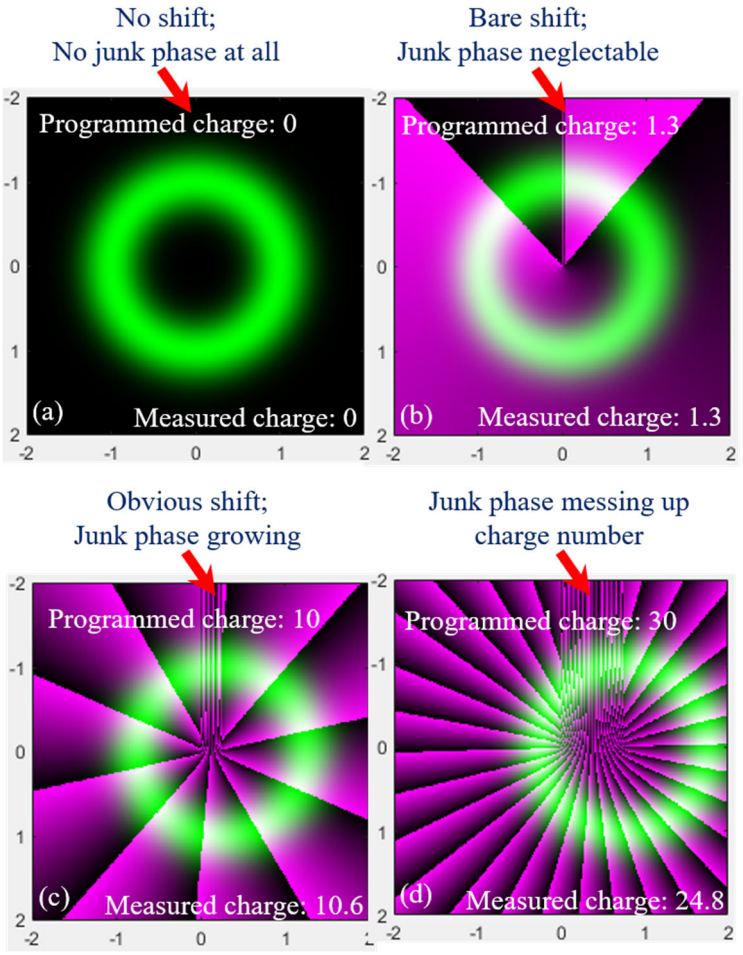

Fig. 4.5 The wrapped ring shift away from the phase corrector's center. (a) m =0 no shift, (b) m = 1.3 bare shift, (c) m = 10.6 obvious shift, (d) m = 30 very large shift.

Theoretically, the linear input phase or tilted wave vector shifts the beam's output location. The shift value can be readily derived from Fourier transform theory or geometric optics' trigonometric relation:

$$\Delta x = \frac{\lambda f m}{2\pi a}, \tag{4.23}$$

where $2\pi a$ is the designed line length. The rigorous phase residual of the wrapped ring shape beam passing through the phase corrector can be expressed as

$$\begin{aligned}\Delta\Omega &= \Omega_{\mathrm{UW}}(x,y) - \Omega_{\mathrm{UW}}(x-\Delta x,y) \\ &= \frac{2\pi a}{\lambda f}\left\{\begin{array}{l} x\left[\arctan 2(y,x) - \arctan 2(y,x-\Delta x)\right] \\ +\Delta x \arctan 2(y,x) + y\ln\left(\dfrac{\sqrt{(x-\Delta x)^2+y^2}}{\sqrt{x^2+y^2}}\right)\end{array}\right\} \\ &\quad -\frac{\pi}{\lambda f}\left(2x\Delta x - (\Delta x)^2\right) + \frac{2\pi}{2\pi a} mx.\end{aligned} \tag{4.24}$$

In Fig. 4.4's ideal case, the phase residual $\Delta\Omega = m\phi$. This happens when the lateral shift is approaching zero $\Delta x = \frac{\lambda f m}{2\pi a} \to 0$. The azimuthal Gaussian transformed asymmetric fractional Bessel Gaussian beam in chapter 3 does not consider the lateral shift and the corresponding aberration or phase distortion, but only the OAM phase. In Fig. 4.5, there are redundant phase generated. The larger the ring shape beam size, the lesser the redundant phase messing up. In general, one can increase the input line zone size $2\pi a$ (scaled by a parameter), the output ring shape beam size $b\exp\left(-\frac{v_0}{a}\right)$ (scaled by b parameter, where v_0 is the input line shape beam's position), and decrease charge number, and decrease focal length f. Given a constant charge number, all the log-polar improvement methods push the log-polar design from the paraxial region to the non-paraxial region. The first time, to our knowledge, pointing out the non-paraxial log-polar design can improve the generated OAM mode's quality or suppress the OAM mode's distortion.

The lateral shift is the reason for OAM mode's degeneration or distortion. But how to evaluate the OAM mode's quality is still an open question. We propose five metrics to evaluate the OAM mode's quality. The first one is the lateral shift ratio, which is defined as

$$\gamma_{\text{shift}} = \frac{\Delta x}{2\rho_0} = \frac{m\lambda \cdot f}{4\pi ab \exp\left(-\frac{v_0}{a}\right)}. \tag{4.25}$$

The smaller the ratio, the cleaner the phase residual $\Delta\Omega$, the better the OAM mode quality. So, in this context, for a given charge number, we are looking for decreased focal length, increased log-polar parameters *a* and *b* to suppress the lateral shift ratio.

The second metric is the average charge number, which is measurable by [25]

$$m_{\text{ave}} = \frac{\int_0^\infty \int_0^\infty \text{Im}\left(xU^* \frac{\partial U}{\partial y} - yU^* \frac{\partial U}{\partial x}\right) \text{d}x\text{d}y}{\int_0^\infty \int_0^\infty U^* \cdot U dx dy}. \tag{4.26}$$

where the U and U^* are arbitrary complex light field and its conjugate. It is evident in Fig. 4.5, the higher the charge number, the more deviation from the measured average charge number to the designed charge number. And hopefully, by reducing the lateral shift ratio, the charge number could be consistent with the designed value.

The third metric is focusing on the far-field Bessel Gaussian beam's symmetry. Fig. 4.6 shows that the wrapped ring's far-field has its peak intensity lobe moving away from the *x*-axis. This is another side effect of the lateral shift caused phase residual. As a comparison, Fig. 4.6 (b) shows a better symmetry, in which case the lateral shift ratio has been suppressed to less than 1%. It is pronounced the beam's symmetry about the *x*-axis is

much better than Fig. 4.6 (a), in which the lateral shift ratio is about 5.3%. The far-field peak intensity shift can be quantized as an absolute distance value. For instance, the far-field peak intensity shift for Fig. 4.6 (a) and (b) are -131 μm and -1 μm, respectively. The azimuthal Gaussian transformed asymmetric fractional Bessel Gaussian beam in chapter 3 does not consider the lateral shift, and the corresponding aberration or phase distortion Eq. (4.24), Fig. 4.6 is closer to $U_{\text{aBG\_GR}}\left(r,\theta,z=0;\beta=0.66,m=4\right)$.

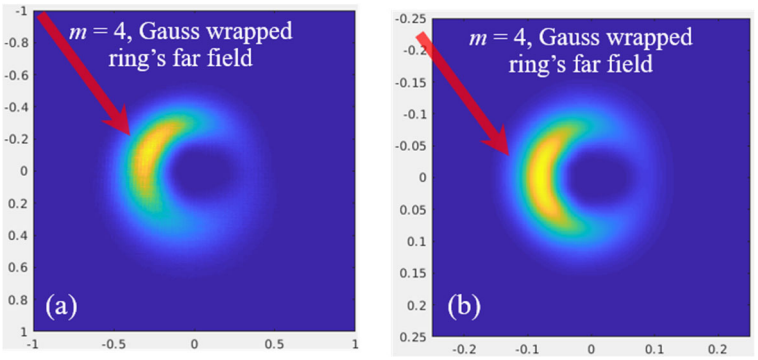

Fig. 4.6 The far-field asymmetric Bessel Gaussian beam's symmetry comparison. (a) traditional log-polar transform result, m = 4 peak intensity location is high above the x-axis, (b) same charge number, lateral shift suppressed design's peak intensity location lands on approximately the x-axis.

The fourth metric goes back to the lateral shift issue itself. Since the lateral shift is deterministic, Eq. (4.23), in numerical simulation, it is possible to shift the whole complex filed back to the origin and then put a corresponding desired OAM phase, which we consider the ideal case. Fig. 4.7 shows the ideal case in purple color and shifted the case in green color. The charge ten log-polar near field ring is shifting very obviously. The Dia in the figure is the $\exp(-2)$ intensity defined diameter. Consequently, the far-field complex

field is different from each other. A cross complex correlation coefficient can be numerically computed given the two complex fields. The closer to one the coefficient, the lesser the lateral shift-induced distortion, the better the mode quality.

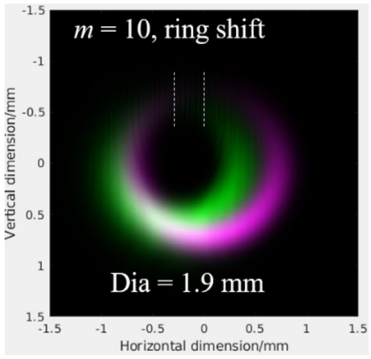

Fig. 4.7 Comparing m = 10 shifted ring (green color) and the ideal case zero shift ring (purple color).

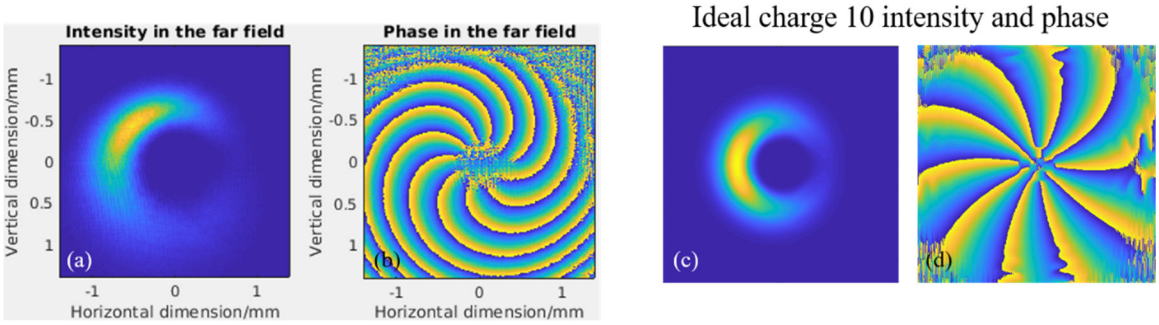

Fig. 4.8 The far-field of m = 10 shifted ring (a) intensity, (b) phase, ideal case no shift ring (c) intensity, and (d) phase.

Finally, power efficiency is always an important parameter to evaluate the diffractive beam shaping, and it is the bottom line of the high-power applications. The novel transformations such as circular-sector transformation [21;86], azimuthal-scaling spiral transformation [87], and fan-out log-polar transformation [17, 18, 88] are not the

best for high-power applications because they are Dammann grating-based design, which reduces the power efficiency dramatically.

In conclusion, the five metrics are 1) lateral shift ratio; 2) average OAM; 3) far-field peak intensity shift; 4) complex cross-correlation coefficient; 5) power efficiency. The next section will discuss a new design with better OAM mode quality, which can be confirmed by the above five metrics.

4.5 Non-paraxial log-polar transform and the new design

The lateral shift is the reason for OAM mode's degeneration or distortion. To obtain asymmetric fractional higher order Bessel Gaussian beam in the far field, there are several methods that one could apply. First of all, increase the propagation medium's refractive index between two log-polar elements [89]. The more general form of Eq. 4.23 is $\Delta x = \frac{\lambda f m}{n_\lambda 2\pi a}$, where n_λ is the refractive index of the propagation medium between the two holograms, for conventional cases n_λ=1, but if n_λ is greater than 1, the lateral shift will be reduced to a small value, then the far-field OAM mode quality will be improved. Secondly, design a separate diffractive optic to multiplicate the resulting lower-order OAM a constant number, such as two or three, resulting in a higher charge number OAM. The examples are circular-sector transformation [21, 86] and azimuthal-scaling spiral transformation [87]. The scaling factor of 2020 published azimuthal-scaling spiral transformation was 3/2 [87]. Due to its fractional phase discontinuity overlay with pseudo-azimuthal uniform intensity, this beam's fractional charge global OAM follows the same yellow curve trend in Fig 3.1. These methods are essentially azimuthal Dammann grating design combined with general

polar transform, which generates multiple azimuthal copies of the original OAM mode. Dammann grating inevitably drops the total power efficiency dramatically, which is not acceptable for any high-power applications. The same issue happens in the lateral Dammann grating design, namely fan-out grating coupled log-polar design [17, 18, 88]. Finally, as section 4.4 shows, the last method should reduce the focal length and enlarge the log-polar parameter a and b to improve the generated OAM mode quality. Fig. 4.9 illustrates the log-polar OAM modes generation process, which is very clear in the insect subplots. Increasing ρ_0 and d are equivalent to increasing a and b. All the tuning methods push the log-polar design from the paraxial region to the non-paraxial region [22].

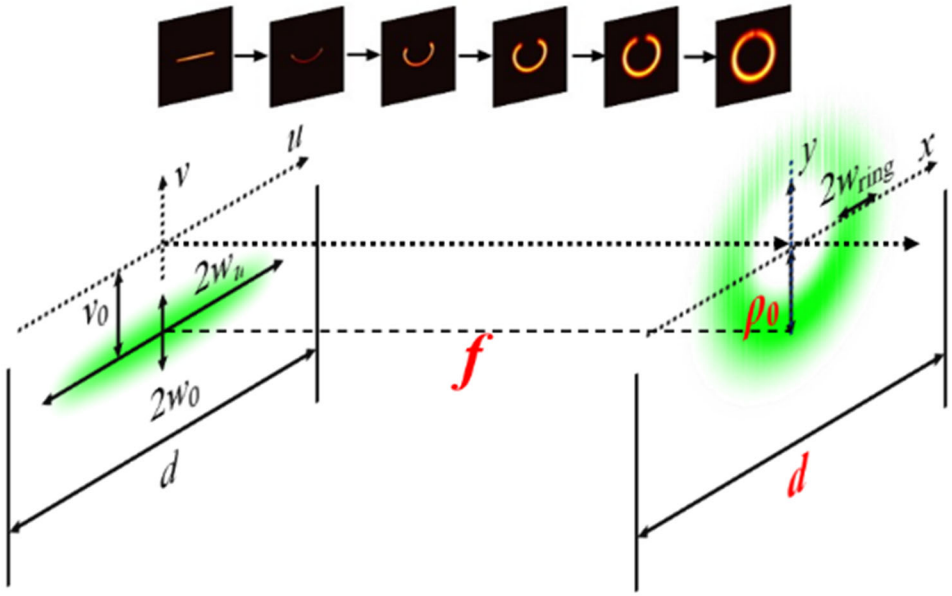

Fig. 4.9 The log-polar OAM modes generation process and the corresponding parameters.

Since paraxial approximation is one foundation of the general geometric transform discussed in section 4.2, we need to consider the rigorous non-paraxial propagation process, such as Rayleigh-Sommerfeld integral

$$U^{\text{out}}(x,y,z)=\frac{z}{\mathrm{j}\lambda}\int_{-\infty}^{\infty}\int_{-\infty}^{\infty}\frac{U^{\text{in}}(u,v)\exp\left\{\mathrm{j}\left[\Omega_{\text{transform}}(u,v)+\frac{2\pi}{\lambda}\sqrt{z^2+(u-x)^2+(v-y)^2}\right]\right\}}{z^2+(u-x)^2+(v-y)^2}\mathrm{d}u\mathrm{d}v, \tag{4.27}$$

where the $U^{\text{in}}(u,v)$ is the input complex light field, the $U^{\text{out}}(x,y,z)$ is the output complex light field, and the $\Omega_{\text{transform}}(u,v)$ is the desired transform phase profile. For the same stationary phase approximation reason, the partial derivatives of the phase term should be zero[22]:

$$\begin{cases}\dfrac{\partial\left[\Omega_{\text{transform}}(u,v)+\dfrac{2\pi}{\lambda}\sqrt{z^2+(x-u)^2+(y-v)^2}\right]}{\partial u}=0\\ \dfrac{\partial\left[\Omega_{\text{transform}}(u,v)+\dfrac{2\pi}{\lambda}\sqrt{z^2+(x-u)^2+(y-v)^2}\right]}{\partial v}=0\end{cases}. \tag{4.28}$$

The first partial derivative of the $\Omega_{\text{transform}}(u,v)$ can be derived as

$$\frac{\partial\Omega_{\text{transform}}(u,v)}{\partial u}=-\frac{2\pi}{\lambda}\frac{x-u}{\sqrt{z^2+(x-u)^2+(y-v)^2}}, \tag{4.29}$$

$$\frac{\partial\Omega_{\text{transform}}(u,v)}{\partial v}=-\frac{2\pi}{\lambda}\frac{y-v}{\sqrt{z^2+(x-u)^2+(y-v)^2}}. \tag{4.30}$$

For a general mapping relation from (u,v) to $\left(x(u,v),y(u,v)\right)$, the solution $\Omega_{\text{transform}}(u,v)$ only exists if and only if the mixed second-order partial derivatives of the

desired phase $\Omega_{\text{transform}}(u,v)$ is the same (Schwarz's theorem or Clairaut's theorem on equality of mixed partials)

$$\frac{\partial^2 \Omega_{\text{transform}}(u,v)}{\partial u \partial v} = \frac{\partial^2 \Omega_{\text{transform}}(u,v)}{\partial v \partial u}. \tag{4.31}$$

Unfortunately, neither log-polar transform mapping relation nor polar transform satisfies the Eq. (4.31) criteria. This means there is no mathematically rigorous solution to the desired phase $\Omega_{\text{transform}}(u,v)$. The only thing that worth trying is to find an approximate solution. Since the first partial derivatives are provided by substituting Eqs. (4.17) and (4.18) into Eqs. (4.29) and (4.30), the desired phase $\Omega_{\text{transform}}(u,v)$ can be reconstructed numerically in the least-squares sense.

Numerically, assume the desired matrix is $n \times n$ lattice, the linear system of equations of size $2n^2$ in n^2 unknowns. The linear system is overdetermined (almost always inconsistent, which means no solution exists). The reconstructed phase is the solution in the least-squares sense, which is the closed approximation. As Fig. 4.10 shows, the partial derivatives are approximated by numerical differences. For instance, use forward difference, backward difference, and central difference represent the leading edge, trailing edge, and interior element's partial derivatives.

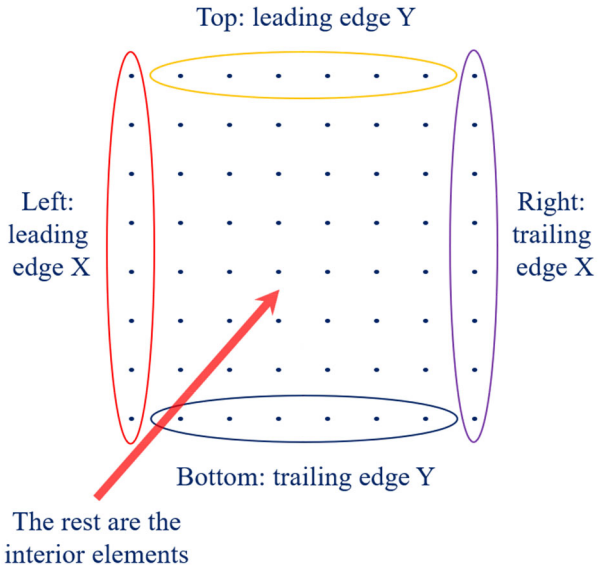

Fig. 4.10 Use numerical differences to approximate the partial derivatives.

The approximation relation can be expressed as

$$\Delta \cdot \underbrace{\Omega_{\text{transform}}(u,v)}_{\text{To be estimated}} \approx \begin{Bmatrix} \dfrac{\partial \Omega_W}{\partial u} \\ \dfrac{\partial \Omega_W}{\partial v} \end{Bmatrix}. \tag{4.32}$$

The desired phase reconstruction/solving can be computed by solving Δ^{-1}

$$\underbrace{\Omega_{\text{transform}}(u,v)}_{\text{To be estimated}} \approx \Delta^{-1} \begin{Bmatrix} \dfrac{\partial \Omega_W}{\partial u} \\ \dfrac{\partial \Omega_W}{\partial v} \end{Bmatrix}. \tag{4.33}$$

For a simple example to visually show the matrix equation, say 4 × 4 lattices, for example, the Eq. (4.32) will be

$$
\begin{bmatrix}
0 & 0 & 0 & -1 & 0 & 0 & 0 & 1 & 0 & 0 & 0 & 0 & 0 & 0 & 0 & 0 \\
-0.5 & 0 & 0 & 0 & 0 & 0 & 0 & 0 & 0.5 & 0 & 0 & 0 & 0 & 0 & 0 & 0 \\
0 & -0.5 & 0 & 0 & 0 & 0 & 0 & 0 & 0 & 0.5 & 0 & 0 & 0 & 0 & 0 & 0 \\
0 & 0 & -0.5 & 0 & 0 & 0 & 0 & 0 & 0 & 0 & 0.5 & 0 & 0 & 0 & 0 & 0 \\
0 & 0 & 0 & -0.5 & 0 & 0 & 0 & 0 & 0 & 0 & 0 & 0.5 & 0 & 0 & 0 & 0 \\
0 & 0 & 0 & 0 & -0.5 & 0 & 0 & 0 & 0 & 0 & 0 & 0 & 0.5 & 0 & 0 & 0 \\
0 & 0 & 0 & 0 & 0 & -0.5 & 0 & 0 & 0 & 0 & 0 & 0 & 0 & 0.5 & 0 & 0 \\
0 & 0 & 0 & 0 & 0 & 0 & -0.5 & 0 & 0 & 0 & 0 & 0 & 0 & 0 & 0.5 & 0 \\
0 & 0 & 0 & 0 & 0 & 0 & 0 & -0.5 & 0 & 0 & 0 & 0 & 0 & 0 & 0 & 0.5 \\
0 & 0 & 0 & 0 & 0 & 0 & 0 & 0 & -1 & 0 & 0 & 0 & 1 & 0 & 0 & 0 \\
0 & 0 & 0 & 0 & 0 & 0 & 0 & 0 & 0 & -1 & 0 & 0 & 0 & 1 & 0 & 0 \\
0 & 0 & 0 & 0 & 0 & 0 & 0 & 0 & 0 & 0 & -1 & 0 & 0 & 0 & 1 & 0 \\
0 & 0 & 0 & 0 & 0 & 0 & 0 & 0 & 0 & 0 & 0 & -1 & 0 & 0 & 0 & 1 \\
-1 & 1 & 0 & 0 & 0 & 0 & 0 & 0 & 0 & 0 & 0 & 0 & 0 & 0 & 0 & 0 \\
0 & 0 & 0 & 0 & -1 & 1 & 0 & 0 & 0 & 0 & 0 & 0 & 0 & 0 & 0 & 0 \\
0 & 0 & 0 & 0 & 0 & 0 & 0 & 0 & -1 & 1 & 0 & 0 & 0 & 0 & 0 & 0 \\
0 & 0 & 0 & 0 & 0 & 0 & 0 & 0 & 0 & 0 & 0 & 0 & -1 & 1 & 0 & 0 \\
-0.5 & 0 & 0.5 & 0 & 0 & 0 & 0 & 0 & 0 & 0 & 0 & 0 & 0 & 0 & 0 & 0 \\
0 & -0.5 & 0 & 0.5 & 0 & 0 & 0 & 0 & 0 & 0 & 0 & 0 & 0 & 0 & 0 & 0 \\
0 & 0 & 0 & 0 & -0.5 & 0 & 0.5 & 0 & 0 & 0 & 0 & 0 & 0 & 0 & 0 & 0 \\
0 & 0 & 0 & 0 & 0 & -0.5 & 0 & 0.5 & 0 & 0 & 0 & 0 & 0 & 0 & 0 & 0 \\
0 & 0 & 0 & 0 & 0 & 0 & 0 & 0 & -0.5 & 0 & 0.5 & 0 & 0 & 0 & 0 & 0 \\
0 & 0 & 0 & 0 & 0 & 0 & 0 & 0 & 0 & -0.5 & 0 & 0.5 & 0 & 0 & 0 & 0 \\
0 & 0 & 0 & 0 & 0 & 0 & 0 & 0 & 0 & 0 & 0 & 0 & -0.5 & 0 & 0.5 & 0 \\
0 & 0 & 0 & 0 & 0 & 0 & 0 & 0 & 0 & 0 & 0 & 0 & 0 & -0.5 & 0 & 0.5 \\
0 & 0 & -1 & 1 & 0 & 0 & 0 & 0 & 0 & 0 & 0 & 0 & 0 & 0 & 0 & 0 \\
0 & 0 & 0 & 0 & 0 & 0 & -1 & 1 & 0 & 0 & 0 & 0 & 0 & 0 & 0 & 0 \\
0 & 0 & 0 & 0 & 0 & 0 & 0 & 0 & 0 & 0 & -1 & 1 & 0 & 0 & 0 & 0 \\
0 & 0 & 0 & 0 & 0 & 0 & 0 & 0 & 0 & 0 & 0 & 0 & 0 & 0 & -1 & 1
\end{bmatrix}
\cdot
\underbrace{\begin{bmatrix}
\Omega_{11} \\ \Omega_{21} \\ \Omega_{31} \\ \Omega_{41} \\ \Omega_{21} \\ \Omega_{22} \\ \Omega_{23} \\ \Omega_{24} \\ \Omega_{31} \\ \Omega_{32} \\ \Omega_{33} \\ \Omega_{34} \\ \Omega_{41} \\ \Omega_{42} \\ \Omega_{43} \\ \Omega_{44}
\end{bmatrix}}_{\text{To be estimated}}
=
\begin{bmatrix}
(\partial\Omega/\partial u)_{11} \\ (\partial\Omega/\partial u)_{21} \\ (\partial\Omega/\partial u)_{31} \\ (\partial\Omega/\partial u)_{41} \\ (\partial\Omega/\partial u)_{21} \\ (\partial\Omega/\partial u)_{22} \\ (\partial\Omega/\partial u)_{23} \\ (\partial\Omega/\partial u)_{24} \\ (\partial\Omega/\partial u)_{31} \\ (\partial\Omega/\partial u)_{32} \\ (\partial\Omega/\partial u)_{33} \\ (\partial\Omega/\partial u)_{34} \\ (\partial\Omega/\partial u)_{41} \\ (\partial\Omega/\partial u)_{42} \\ (\partial\Omega/\partial u)_{43} \\ (\partial\Omega/\partial u)_{44} \\ (\partial\Omega/\partial v)_{11} \\ (\partial\Omega/\partial v)_{21} \\ (\partial\Omega/\partial v)_{31} \\ (\partial\Omega/\partial v)_{41} \\ (\partial\Omega/\partial v)_{21} \\ (\partial\Omega/\partial v)_{22} \\ (\partial\Omega/\partial v)_{23} \\ (\partial\Omega/\partial v)_{24} \\ (\partial\Omega/\partial v)_{31} \\ (\partial\Omega/\partial v)_{32} \\ (\partial\Omega/\partial v)_{33} \\ (\partial\Omega/\partial v)_{34} \\ (\partial\Omega/\partial v)_{41} \\ (\partial\Omega/\partial v)_{42} \\ (\partial\Omega/\partial v)_{43} \\ (\partial\Omega/\partial v)_{44}
\end{bmatrix}
\tag{4.34}
$$

The matrix Δ is not always invertible. One could use QR decomposition to find a least-squares sense solution Δ^{-1} in Eq. (4.33).

Considering the first wrapping phase is a numerical solution, one can find the phase corrector's phase profile from the initial design requirement. This corrector's phase is expected to cancel out the wrapped ring's phase residual but the OAM phase. In other words, for the zero OAM phase case, the corrector should cancel out all the phase components. So, the corrector is designed as the conjugate of zero tilt line $U^{\text{in}}_{\text{OAM=0}}(u,v)$ wrapped ring's phase:

$$U_{\text{corrector}}(x,y)=\arg\left\{\begin{array}{l}\dfrac{z}{\mathrm{j}\lambda}\displaystyle\int_{-\infty}^{\infty}\int_{-\infty}^{\infty}\dfrac{U_{\text{OAM=0}}^{\text{in}}(u,v)}{z^2+(u-x)^2+(v-y)^2}\\ \cdot\exp\left\{\mathrm{j}\left[\Omega_{\text{transform}}(u,v)+\dfrac{2\pi}{\lambda}\sqrt{z^2+(u-x)^2+(v-y)^2}\right]\right\}\mathrm{d}u\mathrm{d}v\end{array}\right\}. \quad (4.35)$$

Above all, the new log-polar optics are designed as $2\pi a = 5$ mm , b = 60 mm, f = 40 mm, pixel size 1 um. By comparing the paraxial log-polar wrapper design Eq. (4.21) and the numerical result that Eq. (4.33) solved, the five metrics do not show an apparent difference between these two cases. Thus the final new log-polar wrapper is designed by Eq. (4.21), and the unwrapper/corrector is designed by Eq. (4.35). The wrapper and unwrapper's dimensions are 10 mm × 5 mm and 10 mm × 10 mm, respectively. The ideal input Gaussian beam's parameters are w_u = 1875 um, w_0 = 375 um, and v_0 = -2522 um.

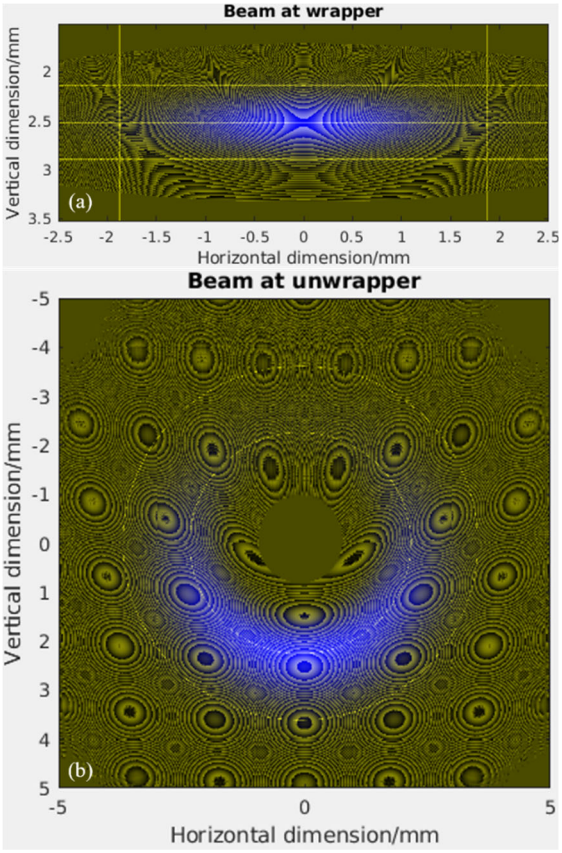

Fig. 4.11 Input Gaussian beam's intensity and the overlapped wrapper's phase (a) and the corresponding azimuthal Gaussian perfect vortex beam's intensity and the overlapped unwrapper's phase (b).

The wrapped azimuthal Gaussian ring's size is corresponding with the input Gaussian beam's vertical position. In Fig. 4.11 (b), the outside yellow ring indicates the $1/e^2$ beam size, and the inner yellow ring indicates the ring's peak intensity location. Aiming to minimize the new design's later ring shift ratio, the wrapped ring size was designed as large as possible. In fact, the wrapped azimuthal Gaussian ring's outside $1/e^4$ size is almost as large as 10 mm in diameter. By shifting the input elliptical Gaussian beam towards the origin, the wrapped azimuthal Gaussian perfect vortex ring will enlarge; shift away from the origin, the ring size shrinks. It's not recommended to scale the wrapped Gaussian ring's size too much, because eventually there will be a power leaking either from the outside boundary or the inside boundary of the unwrapper optic at the phase correction position.

For comparison, the old design and the new design's far-field beam intensity are plotted together in Fig. 4.12. It is pronounced that the new log-polar design's far-field peak intensity is very close to the *x*-axis, which represents good symmetry and OAM mode quality. Furthermore, Table 4.1 shows the whole five metrics comparison between old and new designs.

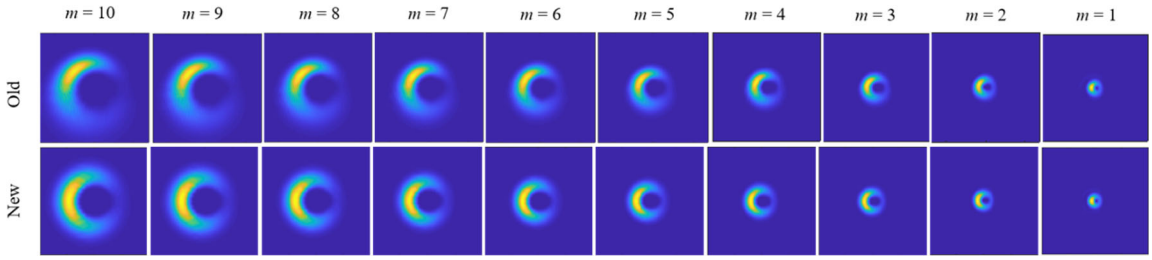

Fig. 4.12 Comparing two versions of log-polar optics design's far-field intensity under different integer charge numbers.

Table. 4.1 Five metrics of old log-polar optics design

Charge	**10**	**9**	**8**	**7**	**6**	**5**	**4**	**3**	**2**	**1**
Shift Ratio/%	13.23	11.90	10.58	9.26	7.94	6.61	5.29	3.97	2.65	1.32
OAM_total	9.6	8.6	7.7	6.7	5.8	4.9	3.9	2.9	1.9	1
Complex Cross Correlation Coefficient/%	52	62	69	81	86	90	93	95	96	96
Far field Peak Intensity Shift/μm	-411	-375	-321	-277	-223	-181	-131	-113	-69	-17
Efficiency/%	93.6	95.5	96.6	98.9	97.1	97.2	97.3	97.4	97.5	97.5

Table. 4.2 Five metrics of new log-polar optics design

Charge	**10**	**9**	**8**	**7**	**6**	**5**	**4**	**3**	**2**	**1**
Shift Ratio/%	1.18	1.06	0.94	0.82	0.71	0.59	0.47	0.35	0.24	0.12
OAM_total	10.03	9.02	8.02	7.02	6.02	5.01	4.01	3.01	2.01	1
Complex Cross Correlation Coefficient/%	99.27	99.46	99.61	99.72	99.79	99.84	99.88	99.88	99.96	99.85
Far field Peak Intensity Shift/μm	-9	-5	-3	-3	-3	-1	-1	-1	-1	-1
Efficiency/%	99.40	99.51	99.53	99.53	99.54	99.54	99.54	99.53	99.57	99.49

Above all, the log-polar optics generated OAM mode's distortion is theoretically analyzed. A new design method is proposed and numerically computed. The proposed five metrics to evaluate log-polar optics generated OAM modes' quality is applied to the old design and the new log-polar optics design. As Table 4.1 and 4.2 show, the new log-polar optics generate better OAM modes than the old version.

4.6 Contribution summary

In conclusion, this chapter analyzed the limitation of log-polar optics. The generated OAM modes' distortion has been carefully studied. The reason for the distortion is the assumption of the none zero transverse wavevector is negligible in the geometric transformation process. In the real geometric transformation, such as the log-polar transform, the none zero transverse wavevector plays an essential role in both the OAM phase generation and the final mode lateral shifting. Hence, the distortion only could be suppressed but eliminated by tuning the log-polar optics design parameters, the closer to the non-paraxial region, the less distortion. The new log-polar design has a noticeable improvement, which is measurable and confirmed by the five mode evaluation metrics including 1) wrapped ring's lateral shift ratio, 2) total OAM charge number, 3) complex cross-correlation coefficient from the idea no shift beam, 4) far-field peak intensity shift, and 5) far-field final mode's power efficiency.

CHAPTER FIVE

COLLIMATOR/FIBER ARRAY HOBBIT

5.1 Introduction

There are a couple of ways to generate higher-order fractional and integer laser modes, such as spatial light modulation (SLM), multiplane light conversion (MPLC), and log-polar transformation. The SLM direct phase modulation can generate any practical phase profile apparently, and this is the most commonly used method. Meanwhile, this method is pricy and dynamic computation is required. It is a good experiment realization but not easy to commercialize for a large number of higher-order laser modes generation. The MPLC, also known as unitary programmable mode converter (UPMC), was first brought by Morizur and co-workers in 2010 [90]. Very similar to the machine learning concept, the MPLC starts from the input and output mode description iteratively design a group of phase profiles to smoothly accomplish the light conversion. This method has already been successfully applied in the commercial space division multiplexing system by CAILabs [91]. In 2019, Fontaine and co-workers reported an MPLC based Laguerre-Gaussian (LG) mode sorter converts 210 LG modes or HG modes [81]. The MPLC requires $2N+1$ phase profiles for the conversion between N inputs and outputs. Even applying the lossless phase element, the loss accumulates dramatically with the number of optical elements. Secondly, the MPLC method adopts an approximation instead of the full theoretical decomposition of unitary transform [91]. The generated mode quality is not perfect even after the smoothness by optimization algorithm such as the simulated annealing (SA) method [92]. Thirdly, for MPLC method always generate the orthogonal

basis of laser modes. In other words, MPLC only generates integer OAM modes. Recently a novel *n*-fold circular-sector transformation was proposed by Ruffato and co-workers [21]. The *n*-fold circular-sector transformation was developed from the basic concept of an optical coordinate geometrical transform. It was essentially an azimuthal fan-out design of log-polar geometric transform, so the power efficiency and fractional charge OAM operation is the primary concern of this transform.

The log-polar geometric transform is another way to generate the higher-order Bessel Gaussian modes. To power efficiently generate continuous higher-order OAM modes, we apply an elliptical Gaussian beam as an input of the log-polar beam wrapper. Then an azimuthal asymmetric ring is the output of the log-polar beam phase corrector. There are two advantages to this beam shaping. Firstly, it's power efficient. The elliptical Gaussian beam avoids power clipping by the log-polar wrapper's acceptance aperture, and then almost all of the power is deflected into the 1st diffraction order. The acceptance aperture is defined as the azimuthal mapping range $[0, 2\pi)$ or $[-\pi, \pi)$, any photon outside the range will be deflected away along the final desired ring shape pattern's propagation process. That's because in the one to one mapping process, the phase corrector only corrects the phase within the acceptance aperture. Secondly, it's average OAM conserved. The average OAM of the fractional Bessel Gaussian beam is approximately the same as the near field designed OAM charge number. That is because of the azimuthal Gaussian distribution assigning the least power at the fractional OAM spiral phase's phase discontinuity location.

The log-polar optical geometric mapping method maps the linear phase tilt into an azimuthal spiral OAM phase. This is the foundation of the log-polar OAM mode generation. Several ways to generate the linear phase tilt: 1) geometrically tilted arrange the source; 2) Fourier transform of shifting is tilted phase or wavevector; 3) use optical modulation device, such as acousto-optic deflector, for example, to modulate the wavevector direction. The first method requires a very fine alignment of multiple sources. And due to the required angle is very small, one source light needs to propagate a very long path to meet the other source's light, so it is not practical. The second method is the most commonly applied. The question is state of the art is almost translating the laser source, either single-mode fiber or collimator, but rare use an array to demonstrate the OAM modes generation.

On the contrary, the array is more practical than the source translation. In this section, we will show fiber/collimator array log-polar OAM modes generation design. We will deliver the third method to generate higher-order OAM modes in Chapter 6. Two practical log-polar OAM mode generation methods are shown in Fig. 5.1.

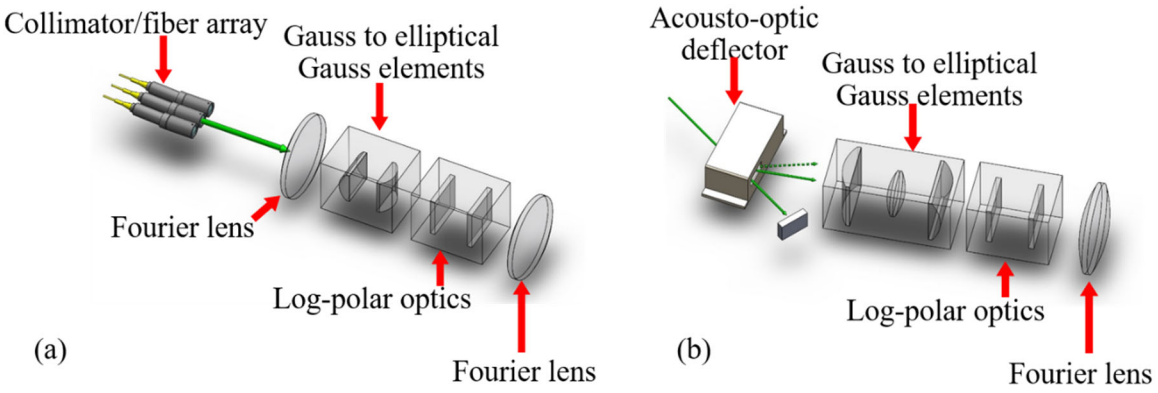

Fig. 5.1. Two practical log-polar OAM mode generation methods (a) fiber/collimator array; (b) acousto-optic deflector.

5.2 1550 nm fiber array HOBBIT

The practical design is important because all the former researches, either published or unpublished, were translating a single source, such as a collimator or a single-mode fiber, to mimic a collimator array or fiber array. But the key is the translation pitch was always very small, not big enough to physically put another collimator or fiber. Thus, it's crucial to know the relationship between the array pitch and the resulting charge number interval. The Fourier transform of shifted light source resulting in linear phase tilt is shown in Fig. 5.2.

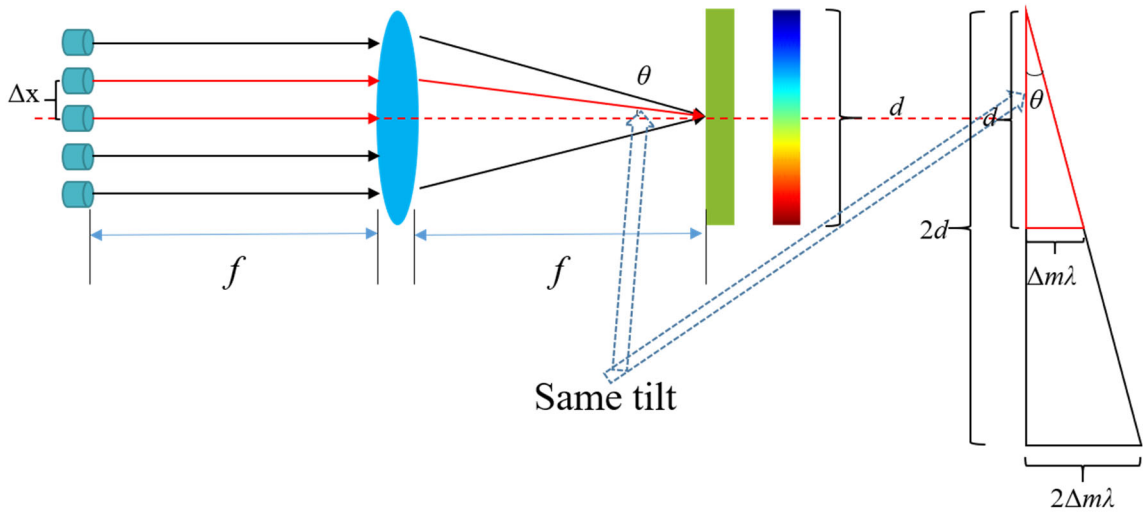

Fig. 5.2. Diagram of single-lens Fourier transform pair of lateral shift and linear phase.

Given the wave vector tilting angle

$$\theta = \arctan\left(\frac{\Delta x}{f}\right), \tag{5.1}$$

where Δx is the lateral array pitch, f is the focal length of the Fourier lens. Considering the charge number related phase gradient angle

$$\theta = \arctan\left(\frac{\Delta m \lambda}{d}\right), \tag{5.2}$$

where Δm is the target OAM mode's charge number difference, λ is the wavelength, d is the corresponding beam size. Due to the tilt angle is the same, the pitch size and the charge number relationship is

$$\Delta x = \frac{\Delta m \lambda f}{d}, \tag{5.3}$$

which is the same equation as the log-polar demultiplexing mode detection resolution equation. This makes sense because mode generation and mode detection are essentially the same things according to the principle of optical reversibility. Given the Gaussian beam's diffraction limit relation

$$w_1 \frac{w_2}{\lambda f} \pi = 1, \tag{5.4}$$

where the w_1 and $w_2 = \frac{d}{2}$ are the Gaussian beam's waist radius on the front and back Fourier plane of the Fourier lens. Substitute the Eq. (5.4) into Eq. (5.3), and we can find the resulting charge number is solely determined by the input array's fill fraction

$$\Delta m = \frac{4}{\pi \cdot \frac{2w_1}{\Delta x}} = \frac{4}{\pi \cdot \text{Fill fraction}}. \tag{5.5}$$

For example, targeting the neighboring array channel's charge number index 1, the corresponding fill fraction is computed as 1.27 > 1, which is not practical. On the other hand, an array structure with fill fraction one results in the charge number interval 1.27. It won't change the result if the input Fourier plane's Gaussian beam has a parabolic phase or not because the diffraction limit is the relation between the Fourier transform pair of Gaussian beam waist. And the Gaussian waist is supposed to be the narrowest position of the whole Gaussian beam. In this context, analog with the diffraction limit equation, Eq. (5.5) could be considered as a charge number and pitch size diffraction limit equation.

Applying the analytical theory of the charge number and pitch size diffraction limit, as shown in Fig5.3, a fiber array higher-order Bessel Gaussian beam generation system was set up. The elliptical Gaussian beam generation optics include a 1550 nm single-mode fiber array with 250 um pitch size and 10.5 um mode field diameter, a cylindrical microlens array with a focal length of 1.6 mm and 250 um pitch size, a cylindrical lens with a focal length of 45 mm and a Fourier-transforming lens with a focal length of 411 mm. The distancing of two log-polar optics is 47 mm.

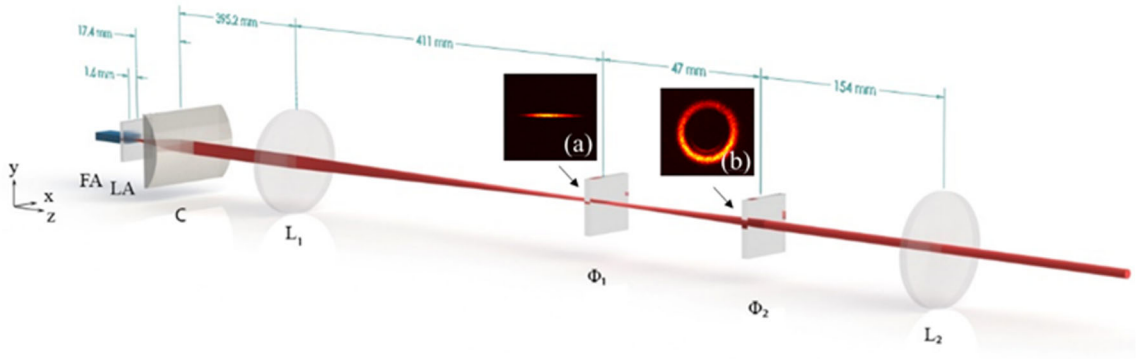

Fig. 5.3. Diagram of line-generation and log-polar transformation. Φ_1 – wrapper, Φ_2 – phase corrector, L_2 – Fourier lens with f=154 mm. Inset (a), line profile on the wrapper inset (b), ring profile on the phase corrector.

The elliptical Gaussian beam generation part is a two-dimensional beam shaping system. In the *x*-direction, the cylindrical microlens array and the Fourier lens work as a 4*f* system; on the *y*-direction, the cylindrical lens and the Fourier-transforming lens work as a two-lens telescope system. The output beam is a 3.35 mm (L) × 300 um Gaussian line, as shown in Fig. 5.3 (a) incident on the wrapper. Fig.5.3 (b) offers the wrapped line-shaped beam right at the 2nd log-polar element and with 1.5× magnification. There are four fiber array ports involved in the experiment. Align the center of the boundary between port 2 and 3 with the system's optical axis, port 1 and 4 SMF will naturally ± 375 um away from the origin due to the 250 μm pitch size. The linear phase tilt introduced by the two SMF at the back focal plane will be ±3.9π. After the log-polar optics wrap the line with a linear phase into a ring, the linear phase will be wrapped into an azimuthal phase of $\exp(jm\theta)$. The corresponding OAM charge number will be approximately $m = \pm 2$, and the resulting interference pattern of these two channels is a four-petal pattern. For the evenly distributed array ports, the charge number interval is around 1.3, then the charge number corresponding with ports 2 and 3 is approximately ±0.7.

Use a phase modulator to modulate channels 2 and 3, and encoded information could be detected and interpreted by the detector. To demonstrate high-speed modulation and detection, we applied a 1 GHz sin function code on the phase modulator, and the signal was detected and decoded experimentally. Meanwhile, for visual demonstration purposes,

a slow modulation version has been performed. The modulation rate was approximately half Hertz, and the experimental result agrees with the simulation very well. The experiment setup and resulting interference pattern are shown in Fig. 5.4. The pattern will rotate periodically with the frequency of the modulation signal. The resulting interference pattern is imaged by an imaging lens to make the detector, Thorlab DET08CL 5GHz InGaAs, only accepting one portion of the pattern. Then the collected photon will be analyzed by the scope. The red circle represents the detector aperture, which is 800 μm in diameter. The beam size is ~ 1700 μm in the longer diameter.

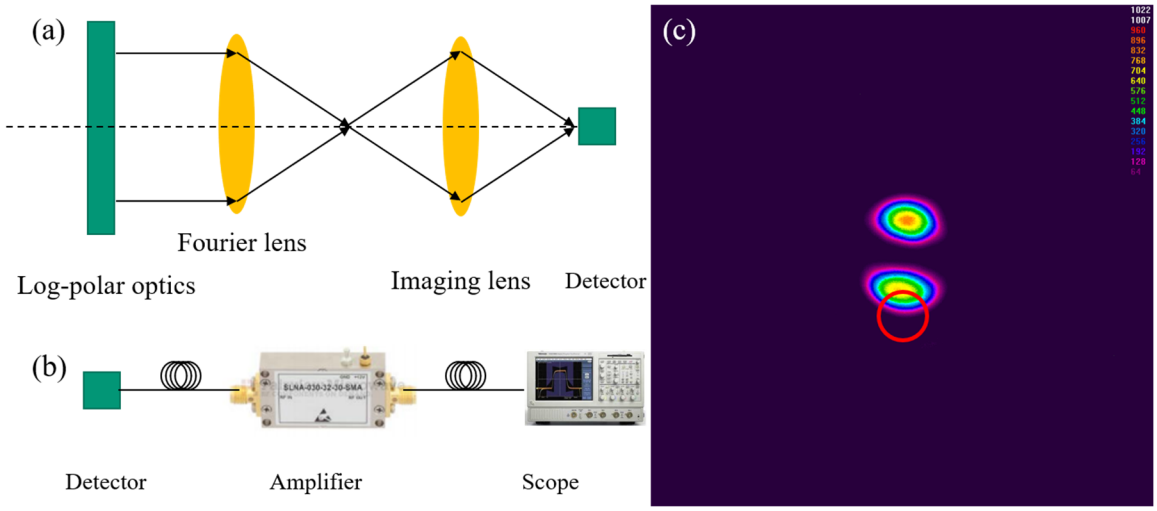

Fig. 5.4. The interference OAM mode detection system. (a) setup, (b) electrical decode system, and (c) resulting interference pattern and detector aperture (red circle).

On the transmitter side, we use Tektronix AWG500 series arbitrary waveform generator(AWG) to generate a 1 GHz sinusoidal wave with 5 G sample/sec sampling rate.

On the detection side, the signal is analyzed by TektronixTDS7404B digital phosphor oscilloscope with the same sampling rate. The transmitted signal is entirely recovered by the detector, as shown in Fig. 5.5.

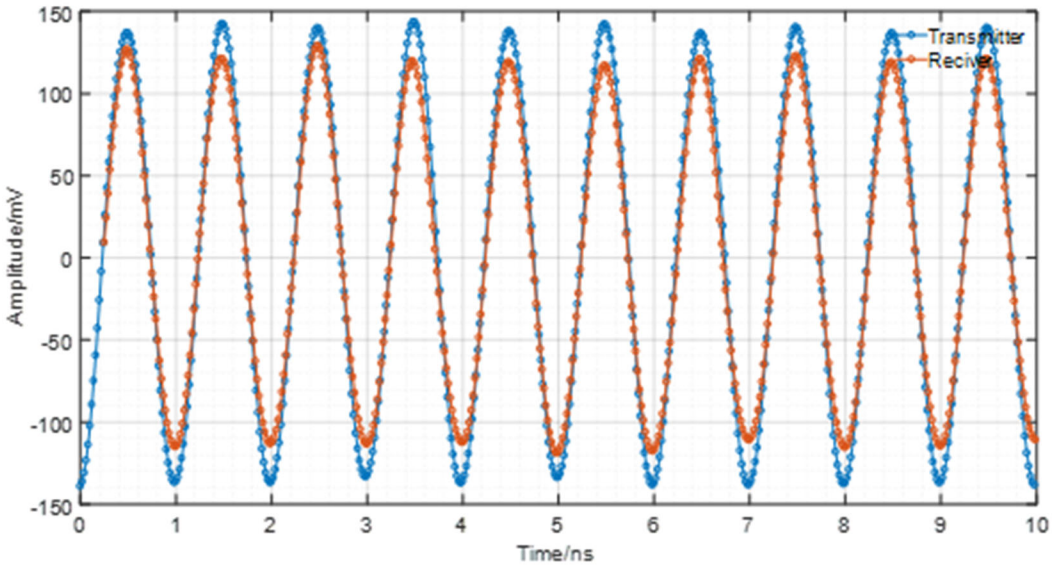

Fig. 5.5 The comparison of transmitted sinusoidal signal and the recovered signal.

This experiment shows that we can dynamically control the phase of ±0.7 OAM mode in the 1550 nm fiber array HOBBIT system. We collect and recover the signal carried by the asymmetric fractional Bessel Gaussian beam as high as 1GHz. This modulation rate beats the fastest SLM's modulation rate (~100MHz). With the OAM modulation ability, this technique can find potential applications in classic/quantum optical communication, dynamic beam control, imaging, directed energy, fractional OAM filamentation, particle manipulation, and probing.

As we introduced in Chapter 3, the far-field generated beams are asymmetric continuous OAM Bessel Gaussian beams. The propagation form of linear polarized asymmetric Bessel Gaussian beam is

$$\overline{U}(r,\theta,z,t) \propto \vec{x} \cdot \exp\left[-\frac{r^2}{w^2(z)} + \mathrm{j}\left(kz - \omega_c t + \frac{kr^2}{2R(z)} - \Theta(z)\right)\right] \cdot \sum_{n=-\infty}^{\infty} B_n \exp(\mathrm{j}n\theta) J_n\left(k_t \frac{r}{\mu}\right), \tag{5.6}$$

where $k = \frac{2\pi}{\lambda}$ is the wavenumber, ω_c is the angular frequency of the light, $R(z) = z\left[1 + \left(\frac{z_R}{z}\right)^2\right]$ is the radius of curvature of parabolic phase front at location z, $z_R = \frac{\pi w_0^2}{\lambda}$ is the Rayleigh range, $\Theta(z) = \arctan\left(\frac{z}{z_R}\right)$ is the Gouy phase, $B_n = \frac{\beta\sqrt{\pi}}{2}\exp\left\{-\frac{\left[\beta\pi(m-n)\right]^2}{4}\right\}\mathrm{Re}\left\{\mathrm{erf}\left[-\frac{1}{\beta} + \mathrm{j}\frac{\beta\pi(m-n)}{2}\right]\right\}$ is the OAM spectrum coefficient, $m \in \mathbb{R}$ is the continuous OAM charge number, β is the ratio of input elliptical Gaussian beam's length versus log-polar wrapper design acceptance line length, $J_n(\cdot)$ is the Bessel function of the first kind of order n, $k_t = \frac{k\rho_0}{f}$ is the transverse wavenumber, ρ_0 is the near field wrapped ring's radius, f is the focal length of Fourier transform lens, $\mu = 1 + \mathrm{j}\frac{z}{z_R}$ is a Gaussian beam propagation scaling factor. As we can tell, the asymmetric Bessel Gaussian beam is a spectrum of integer Bessel Gaussian beam with complex spectrum coefficients. The nondiffractive property is still embedded in the Bessel

Gaussian beam's character. For our HOBBIT beam generated by the setup illustrated by Fig. 5.3, the depth of focus was measured and compared with the general Gaussian beam. The measurement result is shown in Fig. 5.6.

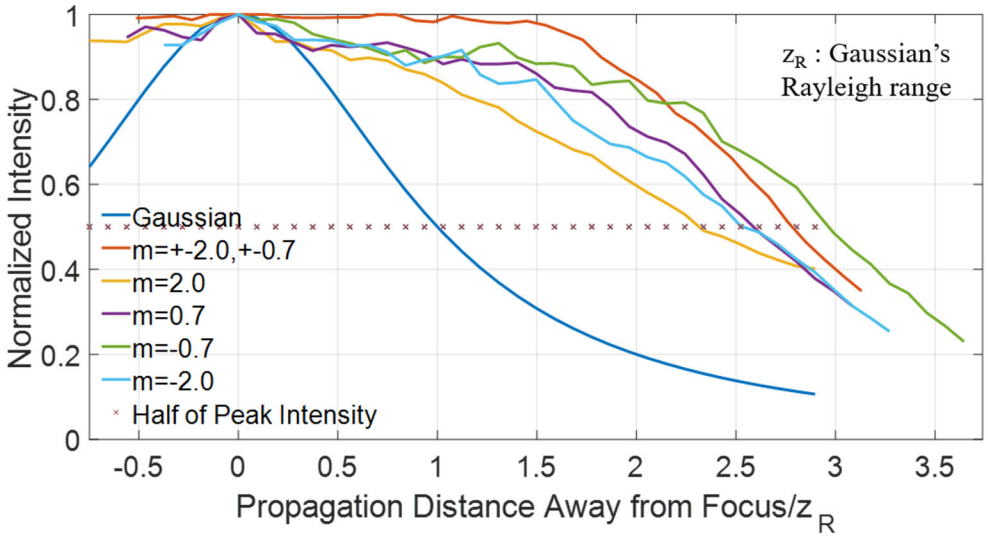

Fig. 5.6 Comparing the depth of focus measurement of Gaussian beam and asymmetric fractional Bessel Gaussian beam.

The depth of focus is defined by [93] the range of the peak intensity drops to a half of the maximum. The more extended depth of focus of the Bessel Gaussian beam can be quickly concluded from Eq. (5.6). The Gaussian envelope evolvement controls the peak intensity. Because the Gaussian envelope has a larger size than the zeroth Bessel central spot, the Bessel Gaussian beam has a longer depth of focus than the standard Gaussian beam, the same size as the zeroth Bessel beam's central spot. In other words, the more ringing effect on the Bessel Gaussian beam, the large the Gaussian envelope size, the longer depth of focus of the Bessel Gaussian beam. When the Gaussian envelope's size is small enough, the Bessel Gaussian beam will reduce to a general Kummer beam.

5.3 Collimator array higher-order fractional HOBBIT generation

Traditionally, researchers translate the collimator source to mimic an array of laser source construction [20]. That's because the charge number and pitch size diffraction limit was confined by Eq. (5.5). To confirm the practical collimator array HOBBIT beam generation method's validity, we have performed two collimators higher-order Bessel Gaussian beam generation experiments. The setup is shown in Fig. 5.7.

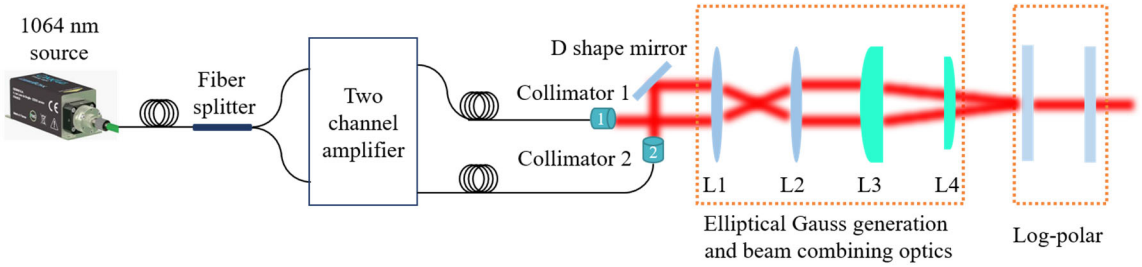

Fig. 5.7 The setup of two collimators HOBBIT beam generation.

The Gaussian output of collimators is shaped into an elliptical Gaussian beam on the input of log-polar optics; meanwhile, the collimator displacement is transformed into a different linear phase at the wrapper location. The charge numbers are designed as ±2 for each collimator, respectively, as shown in Fig. 5.8 (a) and (b). And the charge numbers are confirmed by the optical correlation of charge ±2 SPP. The correlation spot is shown in Fig. 5.8 (c) and (d). The coherent combination mode is shown in Fig. 5.8 (e).

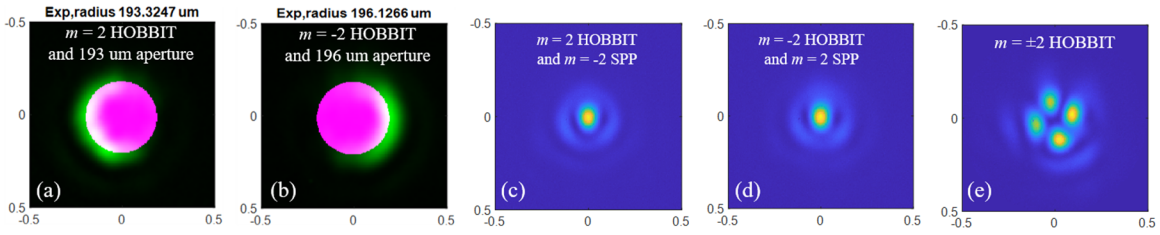

Fig. 5.8 The generated charge ±2 asymmetric Bessel Gaussian beams.

As shown in Fig. 5.8, we have applied two methods to confirm the charge number. Method one, we measure the beam size to ensure the charge number, the beam size of the asymmetric ring is defined by peak intensity location other than the $1/e^2$ method. Method 2, put the conjugate charge SPP after the generated asymmetric Bessel Gaussian beam. The far-field correlation spots are obtained to confirm the charge number as shown in Fig. 5.8 (c) and (d). The power in the correlation spots is measured by approximated 40% of the total power, confirmed by the numerical simulation result. This technique can find potential applications in classic/quantum optical communication, micro object manipulation, directed energy, fractional OAM spectrum analysis, and fractional OAM filamentation. This method's collimator number could expand to a considerable value. The potential confinements are the Fourier lens's aberration, collimators' tip/tilt correction,

5.4 Contribution summary

In conclusion, this chapter gives the array pitch and charge number diffraction limit relation, Eq. (5.5). Higher-order asymmetric fractional Bessel Gaussian beams are generated by a 1550 nm fiber array system and a 1064 nm collimator array system. The depth of focus of the asymmetric fractional Bessel Gaussian beam is theoretically analyzed and experimentally confirmed using the 1550 nm fiber array system. The main contributions are concluded as follow:

1. We dynamically control the phase of ±0.7 OAM mode in the 1550 nm fiber array HOBBIT system.
2. Simulation results predict experimental results well.

3. This asymmetric fractional Bessel Gauss beam could be modulated above 1GHz, which beats the fastest SLM's frequency (100MHz).
4. Potential applications are communication, dynamic beam control, imaging, directed energy, stable fractional OAM beam.
5. The asymmetric fractional Bessel Gaussian beams' depth of focus is longer than the regular Gaussian beam's depth of focus.
6. According to the propagation form of the asymmetric Bessel Gaussian beam, the depth of focus is determined by the Gaussian envelope's Rayleigh range.
7. To have more extended depth of focus, the Bessel Gaussian beam needs to have a larger Gaussian envelope, i.e., more rings.

CHAPTER SIX

AOD HOBBIT SYSTEM

6.1 Introduction

As interest in exploring orbital angular momentum (OAM) properties grows, fast switching between different OAM modes is crucial for exploring applications thoroughly. A common approach in both classical and quantum OAM communications uses different OAM modes as symbols or bits. The capability of switching or hopping between OAM modes can increase the data rate dramatically [94-98]. Studies of OAM beams in turbulent environments suggests that different OAM modes have various propagation performances through turbulence [99, 100]. Fast switching between OAM modes will benefit such studies by enabling the exploration of a wide range of OAM modes. Other sensing related applications that could benefit from rapidly-tunable OAM include beam steering through scattered media [101], particle manipulation using three-dimensional beams [102], object rotation detection [103, 104], temperature sensing [105], and motion detection [106].

So far, one of the most popular techniques for mode switching uses spatial light modulators (SLM), a device that has a very limited switching speed. Digital micro-mirror devices (DMD) can boost switching speeds up to tens of kHz [97], which is comparable with the switching speed of a direct OAM mode emitter [107]. The DMD micro-mirror pitch limits the spatial resolution, while the mode emitter is only capable of tuning integer OAM modes. Fractional OAM modes, also referred to as non-integer [3], continuous [53], successive [53], and rational [54] modes, are another interesting aspect of the study. This is primarily because it is almost impossible to generate an entirely pure integer OAM state.

Secondly, it has been analytically deduced that fractional OAM Bessel beams could form an infinite number of orthogonal subsets of OAM modes[55], which can further benefit classical and quantum optical communication. Thirdly, the fractional OAM Bessel beams preserve the nondiffracting properties that integer OAM beams possess [53]. This property is critical for beam propagation applications, including propagation through turbulence and turbid environments. Moreover, it has been found that a group of fractional OAM modes generated by a synthesis of Laguerre-Gaussian (LG) modes have good structural stability on propagation to the far-field [57]. These LG mode-based fractional OAM states can be used in both classical and quantum communication.

The proposed fast tunable OAM generation technique utilizes an optical geometric transformation[12, 13, 85, 108] known as the log-polar transform [16, 17, 19, 20, 33, 97-99, 109-113]. Refractive log-polar elements were first explored as an efficient OAM mode sorter in 2010 [16]. In 2013, Mirhosseini used a fan-out diffractive beam-copying method to increase the log-polar mode sorter separation efficiency up to 95% [17]. In 2013, Mhlanga successfully sorted more than forty HeNe Bessel beam OAM modes. In 2015, the same elements were successfully used to demultiplex OAM modes with higher mode selectivity and better efficiency than that of cascaded beam splitters [33]. In 2015, Morgan designed and fabricated a diffractive version of the log-polar elements for OAM mode (de)multiplexing [113]. In 2016, Srimathi used the same log-polar elements for an underwater communication link [110]. In 2017, Ruffato made a compact demultiplexing version of the log-polar elements operating at 632.8 nm [19, 20]. In 2017, Lightman 3D printed a log-polar mode sorter, which working for a broad-spectrum of light [112]. In

2018, Ruffato redesigned the log-polar diffractive elements and explored the non-paraxial regime property, which is a good example of diffractive device miniaturization [114].

The AOD is a reasonably fast modulation device that is commonly used for stable phase modulation and beam shaping [115]. Bessel beams have been generated using an AOD array [116] and a cylindrical axisymmetric AOD [117]. In this work, a novel technique for OAM switching and tuning using an AOD in conjunction with a log-polar coordinate transformation system is demonstrated. The maximum mode switching speed for the experimental setup is measured on the order of 400 kHz, which is determined by the acoustic velocity of the crystal as well as the beam diameter. For a different AOD and a reduced beam size, this speed has the potential of reaching tens of MHz with sub-microsecond response time — far higher than the kHz level switching methods mentioned above. Typically, AODs have a very high damage threshold and are widely used in high power laser systems for beam deflecting and laser pulse generation. The integration of an AOD also opens up high power and direct energy related applications for our HOBBIT system.

6.2 Method

The two log-polar coordinate transform optics work as a pair to perform the optical transformation of wrapping a linear-distributed beam into an annular-distribution. The mapping process involves two customized diffractive phase optics: the wrapper, which performs the line to ring transformation. At the same time, the phase-corrector corrects the phase distortion introduced by the wrapper upon propagation. Interestingly, if a length-

wise linear phase is applied along the linear-distributed beam, this will be transformed as well, producing a spiral phase that has been encoded onto the wrapped-ring. Therefore, the far-field of this ring shape beam carries OAM.

As the basis of this work, the optical setup used to generate OAM modes is shown in Fig. 1(a). In this technique, a Gaussian input beam is passed through an AOD. When a voltage signal with the central frequency of the AOD is applied, the 1st order deflection of the Gaussian input is at the Bragg condition with the Gaussian beam propagating along the optical axis. In this orientation, the Gaussian beam has a flat wavefront, and the designed system will generate an OAM mode of charge equal to zero. When the frequency of the acoustic wave deviates from this center frequency, the beam is instead deflected by some additional angle along the horizontal direction, as shown in Fig. 1(a). The deviation away from the Bragg condition results in the 1st order deflection with a tilted phase relative to the axis of propagation. The output of the AOD is then passed through a 4-f embedded line generator, used as a dual-axis manipulator. The output of the 4-f embedded line generator is an elliptical beam with an elongated length and a suppressed height with a phase tilt along the horizontal direction specific to the applied acoustic frequency. This elliptical beam then propagates through the log-polar HOBBIT optics that wrap the ellipse into an asymmetric annular-distribution. Overall, this results in an elliptical Gaussian beam with a linear phase being wrapped into an asymmetric ring with azimuthal OAM phase, which is the angular spectrum of the asymmetric Bessel-Gauss beams. The seminal concept of asymmetric Bessel beams and its physically realistic version, asymmetric Bessel-Gauss beams, have been proposed and studied by Kotlyar in 2014 [23, 65]. In 2018, a general

case of asymmetric Mathieu beams had been analytically derived and experimentally generated by Barcelo-Chong, who showed the recovery of asymmetric Bessel modes when the ellipticity parameter approaches zero [118]. Bessel-Gauss beams are well known for their nondiffracting behavior, but this property relies on the size of the Gaussian envelope. A larger Gaussian envelope produces more ringing outside of the Bessel beams, which in turn produces the longer Rayleigh range. In this case, a small Gaussian envelop is used, which will reduce the nondiffracting behavior. In addition, the azimuthal distribution of the angular spectrum of the asymmetric Bessel-Gauss beams is different from Kotlyar's papers [23, 65], which will be discussed in detail later in this chapter.

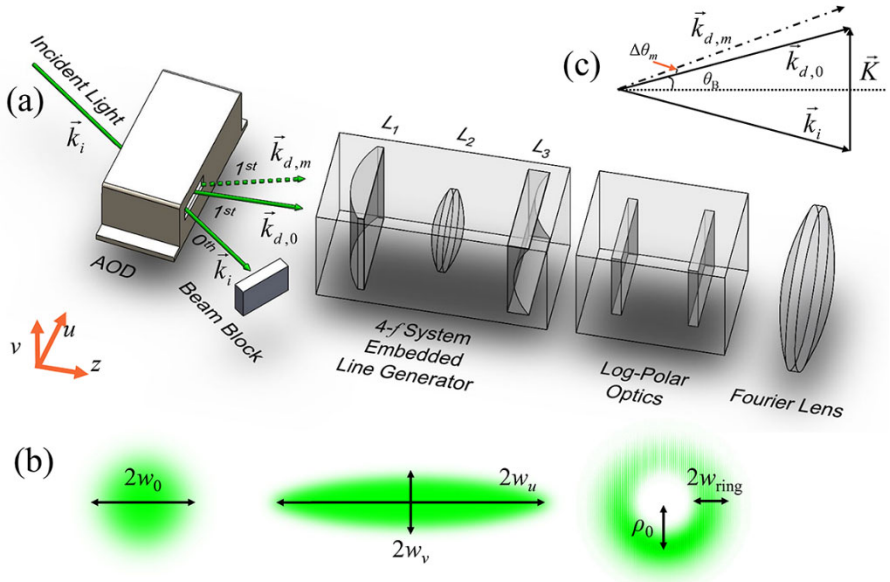

Fig. 6.1. (a) The proposed AOD concept, (b) illustration of the beam profiles at the AOD, after the line generator and after the log-polar optics, and (c) the momentum vector diagram.

The input to the AOD has a Gaussian distribution with the diameter of the beam defined as $2w_0$ as shown in Fig. 1(b). The momentum vector of the incident photon is $\vec{k}_i$, that of the diffracted photon is $\vec{k}_d$, and that of the phonon is $\vec{K}$. According to the principle of momentum conservation, the momentum vector of the diffracted photon should be equal to the sum of the momentum vectors of the incident photon and of the acoustic phonon, $\vec{k}_d = \vec{k}_i + \vec{K}$, shown in Fig. 1(c). The notation $\vec{k}_{d,0}$ and $\vec{k}_{d,m}$ is used for the diffracted photon's momentum vector when the far-field beam has charge 0 and m, respectively. The OAM mode index $m = l + \alpha$ is a continuous charge number in which l is the integer part and α is the fractional part, which is defined as a positive real number $0 \leq \alpha < 1$. The Bragg angle is greatly exaggerated in Fig. 1(a) for visual clarity, and a general Bragg angle equation can be represented as

$$\theta_{\mathrm{B}} \cong \sin\left(\theta_{\mathrm{B}}\right) = \frac{\left|\vec{K}\right|}{2\left|\vec{k}_i\right|} = \frac{\lambda_0 f_0}{2V_{\mathrm{a}}}, \tag{6.1}$$

where λ_0 is the electromagnetic wave Doppler-shifted wavelengths corresponding to the OAM charge 0, V_{a} is the acoustic velocity, and f_0 is the driving frequency of the AOD that results in the Bragg condition, and it's also the frequency corresponding with charge 0 output. The 1st order diffractive angle is $2\theta_{\mathrm{B}}$. By deviating the applied frequency away from the Bragg condition, $\Delta f_{\mathrm{m}} = |f_0 - f_{\mathrm{m}}|$, where f_{m} is the AOD driving frequencies corresponding with charge m output, there is a change in the deflection angle of the beam for charge m as

$$\Delta\theta_m = \left|\theta_m - \theta_0\right| = \left|\frac{\lambda_m \cdot f_m}{V_\mathrm{a}} - \frac{\lambda_0 \cdot f_0}{V_\mathrm{a}}\right| \approx \frac{\lambda_m \cdot \left|f_m - f_0\right|}{V_\mathrm{a}} = \frac{\lambda_m \cdot \Delta f_m}{V_\mathrm{a}}, \tag{6.2}$$

where λ_m is the electromagnetic wave Doppler shifted wavelengths corresponding to the OAM charge m. Since these wavelengths are extremely close with each other, differing by femtometers for a 532 nm input signal, we assume $\lambda_\mathrm{m} \approx \lambda_0$. The angle deviation after the line generator, $\Delta\theta_m$, will be scaled by the magnification of the 1st 4-f system according to

$$\Delta\theta'_m = \Delta\theta_m \frac{F_1}{F_2}, \tag{6.3}$$

where F_1 and F_2 are the focal lengths of the lenses L_1 and L_2, respectively, in Fig. 6.1. According to the paraxial approximation, this angle deviation corresponds to charge m and λ_m can be represented by

$$\Delta\theta'_m \approx \tan\left(\Delta\theta'_m\right) = \frac{\lambda_m m}{2\pi a}, \tag{6.4}$$

where parameter a is one design parameter of the optics which controls the active area in which the line to ring transform is performed in the wrapping procedure. The length of the active area is $2\pi a$, where any portion of a beam that exceeds this length will not be transformed, and therefore, the corresponding power is lost. Combining Eqs. (6.2)–(6.4) results in an expression for charge m as a function of the frequency change from the Bragg condition given by

$$m = \frac{2\pi a\left(\Delta f_m\right) F_1}{V_\mathrm{a} F_2}. \tag{6.5}$$

As shown in Fig. 6.1, the 1st order deflected beam exiting the AOD is a Gaussian distribution, which can be expressed as

$$\begin{aligned} U_{\text{AOD\_1st}}(u,v) &= \exp\left[-\frac{\left(u^2+v^2\right)}{w_0^{\,2}}\right]\exp\left[\mathrm{i}\left(2\pi\left(f_{\mathrm{c}}+f_m\right)t-\vec{k}_{d,m}\cdot\vec{r}\right)\right] \\ &= \exp\left[-\frac{\left(u^2+v^2\right)}{w_0^{\,2}}\right]\exp\left[\mathrm{i}\left(2\pi\left(f_{\mathrm{c}}+f_m\right)t-k_z z-k_u u\right)\right]. \end{aligned} \tag{6.6}$$

where u and v are both Cartesian coordinates, f_{c} is the input laser's central frequency, $k_z = 2\pi\cos\left(\Delta\theta_m\right)/\lambda_m$ and $k_u = 2\pi\sin\left(\Delta\theta_m\right)/\lambda_m \approx 2\pi\Delta\theta_m/\lambda_m$ are the wavenumbers along the z and u direction, and finally $(f_{\mathrm{c}} + f_m)$ and λ_m are the electromagnetic wave Doppler shifted frequency and wavelength corresponding to the OAM charge m. After passing through the AOD, the beam is sent to the line generator to be shaped into an elliptical Gaussian distribution using lenses L_1, L_2 and L_3 with focal lengths F_1, F_2 and F_3, respectively. The elliptical Gaussian beam now has diameters in both dimensions, defined as $2w_{\mathrm{v}} = 2w_0F_3/F_2$ and $2w_{\mathrm{u}} = 2w_0F_2/F_1$. The elliptical beam can be expressed as

$$U_{\text{line}}(u,v) = \exp\left[-\left(\frac{u^2}{w_u^{\,2}}+\frac{v^2}{w_v^{\,2}}\right)\right]\exp\left[\mathrm{i}\left(2\pi\left(f_{\mathrm{c}}+f_m\right)t-k_z' z-k_u' u\right)\right]. \tag{6.7}$$

where the wavenumber along z direction is $k_z' = 2\pi\cos\left(\Delta\theta_m'\right)/\lambda_m = 2\pi\cos\left(\Delta\theta_m F_1/F_2\right)/\lambda_m$, and the wavenumber along u direction is $k_u' = 2\pi\Delta\theta_m'/\lambda_m = m/a$.

The elliptical Gaussian beam is then incident on the log-polar optics, which have been well studied [16, 19, 33, 119]. The HOBBIT mapping process uses two customized log-polar optics: the wrapper that maps the elliptical Gaussian beam to an asymmetric ring

profile and the phase-corrector that corrects the phase distortion introduced by the wrapper. Since the elliptical line has a horizontal Gaussian distribution, the HOBBIT system wraps it into an asymmetric ring with a ring radius, ρ_0, defined from the origin to peak intensity location and width, $2w_{\text{ring}}$, as shown in Fig. 6.1(c). Given the log-polar mapping equation of $u = a\arctan 2\left(y/x\right) = a\phi$, the near-field output from the proposed HOBBIT system is given by

$$U_{\text{near}}\left(\rho,\phi\right) = \exp\left[-\left(\frac{\left(\rho-\rho_0\right)^2}{w_{\text{ring}}{}^2} + \frac{\phi^2}{\left(\beta\pi\right)^2}\right)\right]\exp\left[\mathrm{i}\left(-m\phi + 2\pi\left(f_{\text{c}} + f_m\right)t - k_z' z\right)\right], \qquad (6.8)$$

where ρ and ϕ are both the radial and azimuthal polar coordinates in the near-field plane, $\rho_0 = b\exp\left(-v_0/a\right)$ is the wrapped ring's radius defined from the origin to peak intensity location, $w_{\text{ring}} = b\exp\left(-v_0/a\right)\sinh\left(w_v/a\right)$ is the wrapped ring's half-width, v_0 is the input elliptical Gaussian beam's offset from the center of the wrapper, $w_v = w_0F_3/F_2$ is the half-width of the input elliptical Gaussian beam, a is the log-polar optics design parameter which scales the transformed line length in unwrapping procedure, b is another log-polar optics design parameter which scales the transformed ring size in the wrapping procedure. This parameter is proportional to the wrapped ring radius, ρ_0. And finally, $\beta = w0F_2/(\pi aF_1)$ is the ratio of the input elliptical Gaussian line's length to the designed input line length $2\pi a$. The Fourier transform of Eq. (6.8) can then be derived as

$$U_{\text{far}}\left(r,\theta\right) = A\exp\left(-\frac{r^2}{w_{\text{G}}{}^2}\right)\exp\left[\mathrm{i}\left(2\pi\left(f_{\text{c}} + f_m\right)t - k_z' z\right)\right]\sum_{n=-\infty}^{\infty} B_n \exp\left(\mathrm{i}n\theta\right) J_n\left(\frac{2\pi\rho_0}{\lambda_m F} r\right), \qquad (6.9)$$

where r and θ are both the radial and azimuthal polar coordinates in the far-field plane, $A = -{w_{\text{ring}}}^2 \beta \pi^{5/2} \rho_0 / (2\lambda f)$, $w_{\text{G}} = \lambda_m F / (\pi w_{\text{ring}})$, F is the focal length of the Fourier lens, $B_n = (-\text{i})^{n-1} 2 \exp\left[-\beta^2 \pi^2 (l + \alpha - n)^2 / 4\right] \text{Im}\left[\text{erfi}\left(\text{i}/\beta + \beta\pi(l + \alpha - n)/2\right)\right]$, erfi($x$) = erf(i$x$)/i is the imaginary error function, and finally Im(z) gives the imaginary part of complex number z. As one can tell, the far-field of the ring shape beam in Eq. (6.9) is the combination of a group of Bessel-Gaussian (BG) beams carrying OAM. Intuitively, it is a weighted linear combination of every possible integer OAM phase carrying nth-order Bessel function of the 1st kind modulated by the same Gaussian envelope. The parameter Bn is the weighting or selection factor, which distributes the power within the central 2 to 3 modes and decays rapidly as m approaches positive and negative infinity. When $\alpha = 0$, then $m = l$, meaning an integer charge will be select as $n = l$, and B_l is the maximum value. As α increases, the central weighting factor B_n's maximum value will move from $n = l$ to $n = l + 1$. This means fractional-charged OAM-carrying BG beams are a linear combination of integer BG beams. Considering the $\alpha = 0$ case, the B_n parameter has the property of

$$B_{m-k} = (-1)^k B_{m+k}, k = 0, 1, 2, \cdots \tag{6.10}$$

The far-field complex amplitude described by Eq. (6.9) can be rewritten as

$$U_{\text{far}}(r,\theta)=A\exp\left(-\frac{r^2}{{w_{\text{G}}}^2}\right)\exp\left[\mathrm{i}\left(m\theta+2\pi\left(f_m+f_{\text{c}}\right)t-k_z'z\right)\right]$$
$$\cdot\left\{\begin{aligned}&B_mJ_m\left(\frac{2\pi\rho_0 r}{\lambda_m F}\right)\\&+\mathrm{i}\sin\theta\frac{m\lambda_m F}{\pi\rho_0 r}B_{m+1}J_m\left(\frac{2\pi\rho_0 r}{\lambda_m F}\right)\\&+\cos\theta B_{m+1}\left[J_{m+1}\left(\frac{2\pi\rho_0 r}{\lambda_m F}\right)-J_{m-1}\left(\frac{2\pi\rho_0 r}{\lambda_m F}\right)\right]\\&+\sum_{k=1}^{\infty}\left\{\begin{aligned}&B_{m+2k+1}\left\{\begin{aligned}&\cos\left((2k+1)\theta\right)\left[J_{m+2k+1}\left(\frac{2\pi\rho_0 r}{\lambda_m F}\right)-J_{m-2k-1}\left(\frac{2\pi\rho_0 r}{\lambda_m F}\right)\right]\\&+\mathrm{i}\sin\left((2k+1)\theta\right)\left[J_{m+2k+1}\left(\frac{2\pi\rho_0 r}{\lambda_m F}\right)+J_{m-2k-1}\left(\frac{2\pi\rho_0 r}{\lambda_m F}\right)\right]\end{aligned}\right\}\\&+B_{m+2k}\left\{\begin{aligned}&\cos\left(2k\theta\right)\left[J_{m+2k}\left(\frac{2\pi\rho_0 r}{\lambda_m F}\right)+J_{m-2k}\left(\frac{2\pi\rho_0 r}{\lambda_m F}\right)\right]\\&+\mathrm{i}\sin\left(2k\theta\right)\left[J_{m+2k}\left(\frac{2\pi\rho_0 r}{\lambda_m F}\right)-J_{m-2k}\left(\frac{2\pi\rho_0 r}{\lambda_m F}\right)\right]\end{aligned}\right\}\end{aligned}\right\}\end{aligned}\right\}. \tag{6.11}$$

This indicates that these beams are comprised of only one integer OAM phase exp(i$m\theta$), and the Bessel term of $B_mJ_m\left(2\pi\rho_0 r/\lambda_m F\right)$ dominates since B_m is the maximum of B_n. The standing wave terms $\sin\theta\cdot m\lambda_m FB_{m+1}J_m\left(2\pi\rho_0 r/\lambda_m F\right)/\pi\rho_0 r$ and $\cos\theta\cdot B_{m+1}\left[J_{m+1}\left(2\pi\rho_0 r/\lambda_m F\right)-J_{m-1}\left(2\pi\rho_0 r/\lambda_m F\right)\right]$ contribute to the asymmetric intensity of this group of BG beams. In fact, the rest of the B_n factors are really small in comparison with the central term and contribute minimally to the BG beam, but still in the form of standing waves. As shown in Eq. (6.11), the fractional-charged OAM beams are essentially the combination of integer-charged OAM beams. For each of these integer

components, the parameter B_n works as a window to distribute the power between the integer charge OAMs and decays rapidly as parameter n approaches positive and negative infinity.

As can be seen in Eq. (6.11), a change in β only affects the weighting factor B_n. Conceptually, when β is very small, very little power will be contained at the edges of the active zone on the log-polar elements. When this whole area is wrapped, there will be a highly asymmetric ring. As β approaches 1, the distribution of the wrapped ring becomes more azimuthally Gaussian. In fact, as β increases beyond 1, the distribution about the wrapped ring becomes more azimuthally uniform, and the weighting factors $B_l \pm 1$ decrease, but more of the power will be clipped by the log-polar optic aperture. This results in a lower power efficiency of the system but higher modal symmetry. Equation (6.9) describes not only the distribution of integer charge numbers but also fractional charge numbers. Fig. 2 shows the analytic intensity and phase profiles using simulation parameters $\lambda = 532$ nm, $\beta = 0.66$, $w_{\text{ring}} = 329$ µm, $\rho_0 = 850$ µm, using 5 central terms, and for the focal length of Fourier lens $F = 400$ mm. Due to the small radius of the Gaussian envelope, only one faint ring of the 0^{th} order Bessel-Gaussian beam appears in the simulations and experimental results.

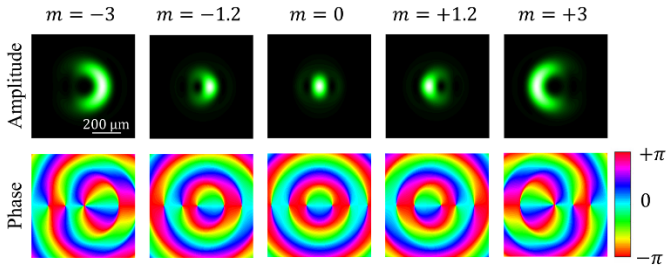

Fig. 6.2. Analytic intensity and phase profiles for $m = \pm 3, \pm 1.2$ and 0.

The log-polar coordinate transform theory assumes that the input is a rectangular shaped beam [12, 13, 85, 108]. This notion, in fact, reduces the translation efficiency of such systems due to the fact that a Fourier transform of a rectangular function contains high spatial frequency components. On the other hand, the Fourier transform of a Gaussian shape produces another Gaussian distribution. In the HOBBIT system presented above, an elliptical Gaussian beam is easily generated from a Gaussian input. This has the added benefit of a higher power efficiency compared to that of a rectangular beam input.

6.3 Diffractive phase-only optics

The diffractive log-polar HOBBIT elements are fabricated using a photolithographic method in our cleanroom facility as shown in Fig. 6.3(a), 6 row × 6 column devices has been fabricated on a single wafer. The optics are optimized for the wavelength of 532 nm, and have a pixel size of 2 μm × 2 μm and $2^4 = 16$ phase levels. The design parameter a is $1.8/\pi$ mm and b is 2 mm. The microscope profiles of a wrapper and phase-corrector are shown in Fig. 3(b) and (c). Scanning electron microscopy (SEM) images of the fabricated optics are shown in Fig. 3(d) and (e) with a magnification of 130×. The theoretical diffraction efficiency of a 4-layer lithographic process diffractive phase element is about 98%. After applying a 99.9% transmission anti-reflection (AR) coating on each surface of the HOBBIT optics, the mean transmission efficiency of both the wrapper and phase corrector combined has been measured to be 91% with 0.5% standard deviation from charge -10 to 10.

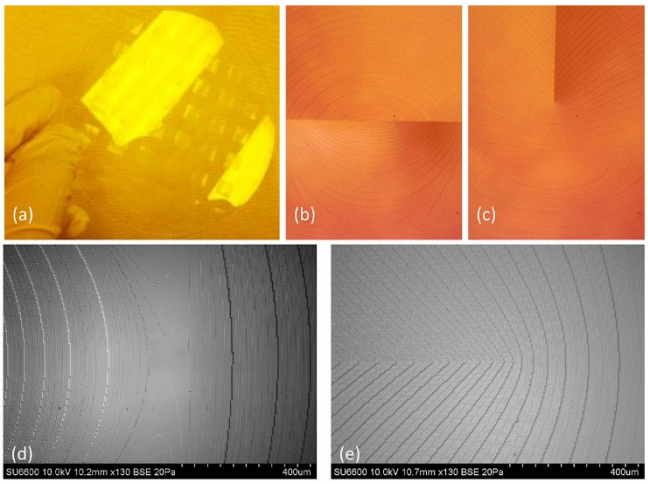

Fig. 6.3. (a) Multiple log-polar device fabrication on a single wafer, (b) the microscope image of central part of wrapper and (c) phase corrector, (d) the 130× magnification SEM inspection of device center of wrapper and (e) phase corrector.

6.4 Experimental setup and results

The AOD couples up to 70% of the optical energy into its 1st diffraction order. This deflection angle is continuously tunable by adjusting the frequency of the acoustic signal. As mentioned above, our experimental setup applies a 4-*f* system to image the AOD output deflection angle into the line shape beam's linear phase and another 4-*f* system to elongate the circular Gaussian beam into an elliptical Gaussian beam. The elliptical Gaussian beam is incident upon the wrapper and then is mapped into an azimuthally asymmetric ring shaped beam during propagation to the phase corrector. After phase correction at the second optical element, the ring-shaped beam carrying OAM phase will form a BG beam in the far-field. A diagram of the experimental setup is shown in Fig. 6.4.

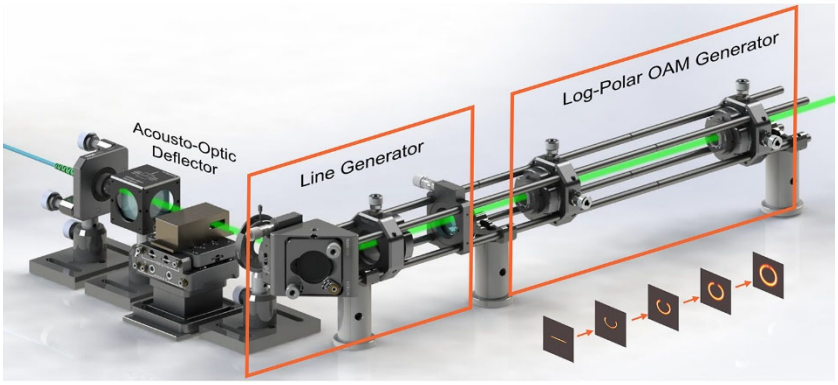

Fig. 6.4. Diagram of the acousto-optic deflector, line-generator and log-polar transformation optics.

The deflected beam was generated using a Gooch & Housego AODF 4120-3. This AOD is constructed using a tellurium dioxide (TeO_2) crystal, with a Bragg angle of 2.9°, computed by Eq. (6.1), as shown in Fig. 6.5. The acoustic velocity is 0.65 mm/μs, typical for the shear mode of a TeO_2 crystal. An input beam with a diameter of approximately 1.5 mm can be deflected at a rate of approximately 434.8 kHz, corresponding to a measured switching speed of 2.3 μs. Higher switching speeds are achievable in other materials such as quartz and fused silica. The acoustic velocity of such devices can be an order of magnitude above the shear-mode TeO_2 devices. By decreasing the beam size through a crystal and with a faster acoustic velocity, switching speeds could be further increased into the tens of megahertz. A picture of the compact experimental setup is shown in Fig. 6.5. The transmission efficiency of each surfaces of the 3 optics in the line generator is 99%, and the total transmission efficiency of log-polar OAM generator is 91%. Taking into account the 70% AOD's 1st order diffraction efficiency (DE), the total system efficiency is approximately 60%. Given a 30 mW input power, the output BG beam is approximately

18 mW. Given that the AOD requires a specific linear polarized input beam, this experimental setup is restricted only to one linear polarization.

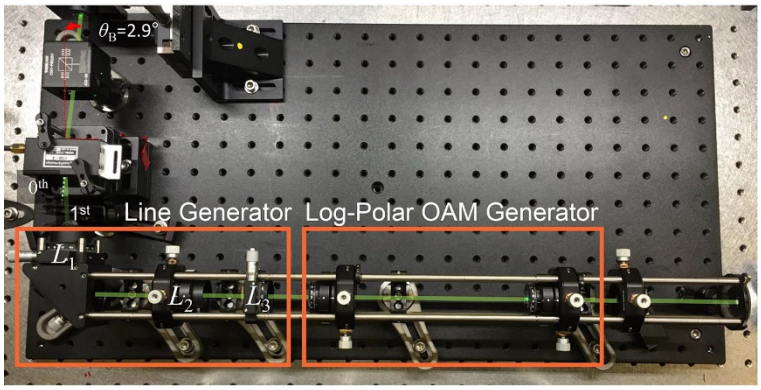

Fig. 6.5. Picture of the continuously tunable OAM generation system.

The focal lengths L_1 and L_2 are F_1 = 50 mm and F_2 = 100 mm respectively, parameter a = 1.8/π mm, and the frequency index corresponding to Δm = 1 interval is Δf_1 = 0.36 MHz. A series of rings with different OAM phases are output from the log-polar HOBBIT optics. The far-field of this group of ring shape OAM phase carrying beams are BG beams [111]. The generated BG beams are experimentally generated, imaged, and simulated using Eq. (6.9), as shown in Fig. 6.6. The experimental results have a good agreement with the simulation results. A comparison of the radius of the dark vortex to the corresponding charge numbers as well as driving signal frequencies is shown in Fig. 6.7 for both the experimental and simulated beam profiles. This radius was measured by finding the inner radial location of the half-maximum amplitude. The simulation is an approximation of an infinite series. The slight dips in the curve are a result of truncating the infinite series to obtain this approximation. The DE of the m = -5 beam is 8.8% lower

than the DE of the m = 5 beam because of the deviation away from the Bragg condition that has the highest DE.

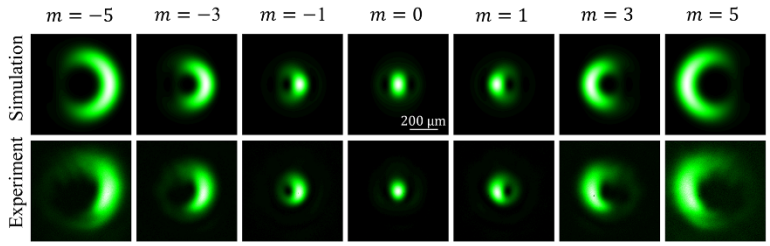

Fig. 6.6. Comparison of analytic expression with β = 0.663 and ρ_0 = 850 μm.

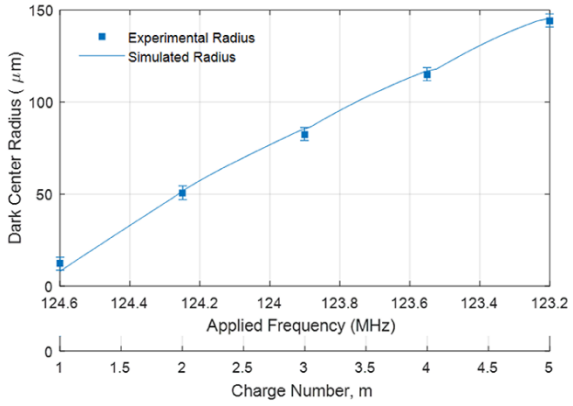

Fig. 6.7. The simulated and experiment results of BG beams central dark area's radius vary with charge number as well as AOD driving signal's frequency.

The deflection angle of the 1st order AOD output is continuously tunable. Therefore the OAM phase is continuously tunable as well. The intensity distributions of the fractional OAM modes spanning from charge -1.2 to +1.2 in steps of 0.6 are shown in Fig. 6.8. The charge numbers are verified by the single stationary cylindrical lens method [24, 72, 120] as -1.21 ± 0.03, -0.63 ± 0.03, -0.01 ± 0.08, 0.64 ± 0.02 and 1.21 ± 0.02.

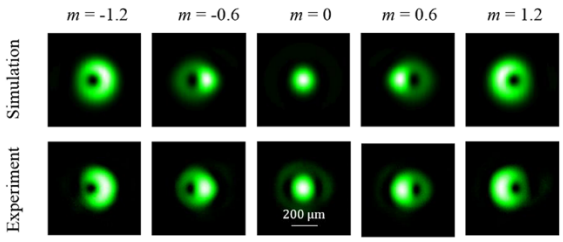

Fig. 6.8. Experimentally generated and simulated fractional OAM BG beams.

6.5 Conclusion

In conclusion, we have proposed a method of cascading an AOD with the HOBBIT log-polar transform the optical system to rapidly and continuously tune the output OAM mode of a BG beam. This means the HOBBIT system has the capability of generating tunable fractional OAM modes. The OAM mode is controlled through the AOD driving frequency, which controls the amount of linear tilt to be wrapped into a ring through the log-polar transformation. The tuning speeds of AODs are limited by the velocity of the acoustic wave through the crystal, which has the potential to well exceed conventional mode manipulators such as DMDs, SLMs, and single electrically contacted thermos-optical controlled vortex emitters. The scalar form of the far-field HOBBIT has been analytically derived, resulting in a group of asymmetric fractional BG beams.

This technique provides a fast and continuous OAM carrying BG beam tuning solution. This HOBBIT system may benefit a multitude of areas not limited to communication from classical to quantum applications, particle optical manipulation, beam shaping, laser beam machining, microscopy, microlithography, direct energy, filamentation [36-38], as well as sensing through turbulence in the air and underwater environments. OAM is rapidly gaining interest in all of these areas, and the tunable

capabilities of this system have the potential to open up the in-depth study of these modes under various conditions, including environments that change slowly, such as turbulence. Also, the AOD can support a superposition of driving frequencies that result in multiple OAM modes being generated simultaneously. Because of this, future work will consist of exploring coherent combinations of OAM modes from this AOD based HOBBIT system.

6.6 Contribution summary

The whole AOD HOBBIT system is teamwork. This dissertation's significant and innovative contribution is developing the imaging method instead of the original Fourier transform method to realize log-polar input functionality. The imaging method uses a minimum number of lenses, namely three, to efficiently shape the regular Gaussian beams into a group of overlapped tilted elliptical Gaussian beams. The log-polar optics transform these elliptical Gaussian beams into azimuthal Gaussian perfect vortex beam carrying corresponding OAM phase. Due to the OAM phase is continuously tunable, the asymmetric fractional Bessel Gaussian beams charge number spectrum, OAM phase, and transverse intensity distributions are easily manipulated at high speed. The fabricated diffractive log-polar optics' diffraction efficiency is as high as 91%.

CHAPTER SEVEN

CONCLUSION AND FUTURE WORK

7.1 Conclusion

This work deepens the understanding of the fractional OAM concept and asymmetric Bessel Gaussian beam. Driven by the OAM conservation law, an average OAM conserved fractional OAM mode is found as an asymmetric mode; namely, asymmetric fractional Bessel Gaussian beam. This beam is different from the well-known asymmetric Bessel Gaussian beam derived by Kotlyar in 2014 [23]. Because the OAM spectra are different, even the two groups of beams are built on the same bases, the Bessel Gaussian beam. Kotlyar's asymmetric Bessel Gaussian beam's spectrum shifts away from the initial setting OAM toward infinity and increase the average OAM value accordingly. Our asymmetric Bessel Gaussian beam's spectrum is always centered at the initial setting OAM, either integer or fractional. With a similar asymmetric profile, our asymmetric Bessel Gaussian beam's OAM spectrum is narrower than Kotlyar's case. And most importantly, our beam conserves the average fractional OAM.

This work starts from the introduction of regular integer OAM mode to the concentric OAM mode. The concentric OAM beam is the most straightforward OAM spectrum combination because there are only two OAM modes. The concentric SPP has been studied for helical filamentation [36], underwater communication [39], and high power amplification applications [40]. In this work, it's the first time, to our knowledge, that we derive the complete propagation form of the concentric SPP beams without applying the stationary phase approximation. The experiment result and the simulation

agree with each other well. The propagation induced interference pattern rotation was analyzed to be the consequence of the Gouy phase change. Furthermore, the multi-harmonic concentric SPP diffractive optics design has been well studied.

Following the integer OAM case, we analyzed the fractional OAM and the asymmetric Bessel Gaussian beam. The fractional OAM is inherently the coherent combination of integer OAM modes. Therefore, for each specific fractional OAM mode, there is an OAM spectrum to represent the combination. And the fractional OAM mode's spectrum is centered (or power averaged) at a fractional OAM value. Meanwhile, the OAM spectrum and the azimuthal distribution are a Fourier transform pair. Hence, given a uniform azimuthal distributed light field such as Gaussian or Gaussian rings or Laguerre Gaussian or Bessel Gaussian or Kummer beam or perfect vortex beam, as long as the OAM spectrum exists, the propagated fractional OAM mode will eventually evolve into an asymmetric azimuthal distribution. The asymmetric Bessel Gaussian beam and the azimuthal Gaussian perfect vortex beam are a Fourier transform pair. They propagate into each other no matter the initial OAM spiral phase is an integer or fractional. Moreover, if the initial OAM spiral phase is a fractional structure, the Fourier transform of which is still centered at the adjacent of the initial fractional OAM setting. The comparison of the beam with the famous asymmetric Bessel Gaussian beam is mentioned at the very beginning of this chapter.

Then how to generate the beam? We use log-polar diffractive optics to map a tilted elliptical Gaussian beam to an azimuthally distributed ring, and the Fourier transform of which is the asymmetric Bessel Gaussian beam. The log-polar optical coordinate transform

element has been well studied. But for the higher-order OAM mode generation or detection, there is always an unexpected distortion. The distortion comes from the linear phase tilt we introduced in the elliptical Gaussian beam. It's a dilemma because the linear phase is also the key to OAM mode generation. If there is no linear phase, the output charge will always be zero. On the other hand, the linear tilt also shifts the beam's location after a specific distance propagation or Fourier transform. The shifting is negligible when the tilt/OAM is small, but as the required charge number increases, the shifted beam's phase can not be well collimated by the second log-polar optic. The resulting junk phase distorted the beam tremendously. The issue becomes that the shift is there and can not be removed or compensated, only possibly limited or reduced to a negligible value. That means the ratio of lateral beam shift over beam size has to be small. The first way to reduce the shift ratio is to increase the refractive index between the two log-polar elements. Martin Lavery's alignment-free log-polar mode sorter is a perfect example of this case. Secondly, bear with the shift ratio of lower charge OAM mode, then use an OAM multiplication element to increase the lower charge to a higher charge. The charge number relation is preferably multiplication other than addition (traditional SPP). Because addition only shifts the OAM number in the OAM spectrum, but multiplication amplifies the OAM. Some may concern the addition only goes to one side of the OAM spectrum, say the positive OAM side, but reduces the negative OAM side. This problem is the OAM handedness issue. Both the flipping of the SPP side and mirror reflection imaging method could flip the OAM handedness. The to-date OAM amplification methods are all combined with Dammann grating design. The drawback of these methods is power efficiency always low. The last

one is what we proposed in this work, design a pair of log-polar optics to have a shorter optics separation and larger beam size. This method will lead to a paraxial approximation violation issue. Then the corresponding new log-polar design is proposed. We developed five metrics to evaluate the asymmetric OAM mode quality. According to these five metrics, the new design log-polar optics generated OAM performs much better than the traditional log-polar optics design.

Lastly, we demonstrated the fiber/collimator array method and the AOD method to generate higher-order Bessel Gaussian beams. The AOD method has the advantage of fast tuning OAM mode. And the OAM spectrum could be coded in the AOD's radio frequency signal. Most importantly, the AOD method OAM control is quicker and more power-efficient than SLM OAM mode tuning.

7.2 Future work

On the detection side, the average OAM, OAM density, OAM spectrum detection is the fundamental metrology in future research. Apparently, the best way is to reconstruct the phase front. Phase front reconstruction, such as the Shack-Hartmann wavefront sensor, and the phase-shifting interferometry, provide the wavefront information. All the relevant information, such as OAM density and spectrum, could be readily computed from it. But the phase front's spatial resolution is the bottleneck of the computation precision, which drives the price soaring for high accuracy high precision measurement. Other than the optical correlation method, the two cylindrical lens method [72] is an inexpensive, medium complicated method. This method's smart part is that a cylindrical lens pair transform the OAM into linear momentum and maps at the corresponding location at the back Fourier

plane. In the future, this method could be developed into a new phase front detection method. And also, combining with the optical correlation method, the OAM measurement's precision could be improved to a higher level.

On the generation side, high efficient low distortion OAM mode generation is expected. A high efficient OAM amplification mapping method, such as a high-efficient version of the circular sector polar transformation, will benefit the high power application. Geometric mapping or OAM mode shaping is easy, but high efficiently doing so is always a challenge. The new log-polar design generated asymmetric fractional Bessel Gaussian beam is a good starting point for this topic.

The generated beam's mathematical expression and electromagnetic property should be well studied. The interaction with the environment and the matter such as atmosphere, aerosol, water, marine water, typical conductive or dielectric particles, magnetic particles, should benefit a broad range of research spectrum.

Structure light's unique freedoms include both OAM mode and spatial polarization manipulation. The full Poincaré beam could be generated by a coherent (or partial coherent) combination of different laser modes with perpendicular polarization states. Polarization tailoring (full Poincaré beam) and OAM editing (fractional OAM) are two powerful tools to open multiple exciting applications in the future. The most exhilarating ones are quantum computation and quantum communication applications.

7.3 Major Contributions

1. We elaborated on the fractional OAM beam's average OAM conservation dilemma.

2. We first time to our knowledge, proposed a novel fractional vortex beam with exemplary average OAM conservation, an asymmetric fractional Bessel Gaussian beam.
3. We systematically compared the proposed asymmetric fractional Bessel Gaussian beam and the famous Kotlyar's asymmetric Bessel Gaussian beam.
4. We studied the fractional OAM's spectrum nature and the Fourie transform relation with the azimuthal distribution.
5. We derived the Fourier transform pair of concentric SPP beam and incomplete Kummer beam. We studied the complete propagation form of this group of beams. And we systematically analyzed the beam's unique properties.
6. We derived the Fourier transform pair of asymmetric fractional Bessel Gaussian beam and azimuthal Gaussian fractional perfect vortex beam. We studied the complete propagation form of this group of beams. And we systematically analyzed the beam's unique properties.
7. We first time to our knowledge, pointed out the log-polar geometric mapping method OAM mode generation's beam distortion reason. We analyzed the potential solution and proposed a new design.
8. We first time to our knowledge, derived the diffraction limit relation of the array pitch and the corresponding OAM interval.
9. We experimentally demonstrate the fiber/collimator array and the AOD method generating higher-order asymmetric fractional Bessel Gaussian beams.

10. The whole AOD HOBBIT system is teamwork. This dissertation's significant and innovative contribution is developing the imaging method instead of the original Fourier transform method to realize log-polar input functionality. The imaging method uses a minimum number of lenses, namely three, to efficiently shape the regular Gaussian beams into a group of overlapped tilted elliptical Gaussian beams. The log-polar optics transform these elliptical Gaussian beams into azimuthal Gaussian perfect vortex beam carrying corresponding OAM phase. Due to the OAM phase is continuously tunable, the asymmetric fractional Bessel Gaussian beams charge number spectrum, OAM phase, and transverse intensity distributions are easily manipulated at high speed. The fabricated diffractive log-polar optics' diffraction efficiency is as high as 91%.

APPENDIX

Appendix A

PUBLICATION LIST

Patent

1. Johnson, Eric G., Jerome Keith Miller, Richard Watkins, Kaitlyn Morgan, **Wenzhe Li**, and Yuan Li. "Tunable Orbital Angular Momentum System." U.S. Patent Application 16/725,293, filed June 25, 2020.

Refereed Journal Publications

1. **Wenzhe Li**, Kunjian Dai, Eric G. Johnson, J. Keith Miller, Caitie O' donnell "Multiple harmonic concentric spiral phase plate," *Opt. Continumm*, preparing
2. Kunjian Dai, **Wenzhe Li**, Kaitlyn S. Morgan, Yuan Li, J. Keith Miller, Richard J. Watkins, and Eric G. Johnson, "Second-harmonic generation of asymmetric Bessel-Gaussian beams carrying orbital angular momentum," *Opt. Express* 28, 2536-2546 (2020)
3. Richard J. Watkins, Kunjian Dai, Graham White, **Wenzhe Li**, J. Keith Miller, Kaitlyn S. Morgan, and Eric G. Johnson, "Experimental probing of turbulence using a continuous spectrum of asymmetric OAM beams," *Opt. Express* 28, 924-935 (2020)
4. F. Sanson A. K. Pandey, I. Papagiannouli, F. Harms, G. Dovillaire, E. Baynard, J. Demailly, O. Guilbaud, B. Lucas, O. Neveu, M. Pittman, D. Ros, M. Richardson, E. Johnson, **Wenzhe Li**, Ph. Balcou, and S. Kazamias, "Highly multimodal structure of high topological charge EUV vortex beams," *Opt. Lett*. 45, 4790-4793 (2020)
5. **Wenzhe Li**, Kaitlyn S. Morgan, Yuan Li, J. Keith Miller, Graham White, Richard J. Watkins, and Eric G. Johnson, "Rapidly tunable orbital angular momentum (OAM) system for higher order Bessel beams integrated in time (HOBBIT)," *Opt. Express* 27, 3920-3934 (2019)

6. Yuan Li, Kaitlyn Morgan, **Wenzhe Li**, J. Keith Miller, Richard Watkins, and Eric G. Johnson, "Multi-dimensional QAM equivalent constellation using coherently coupled orbital angular momentum (OAM) modes in optical communication," *Opt. Express* 26, 30969-30977 (2018)
7. K. Morgan, Yuan Li, **Wenzhe Li**, J. Keith Miller, Richard J. Watkins, Eric G. Johnson, "Multilevel quadrature amplitude multiplexing using coherently coupled orbital angular momentum modes," *Opt. Express* 26, 12180-12190 (2018)
8. F. Sanson, A. K. Pandey, F. Harms, G. Dovillaire, E. Baynard, J. Demailly, O. Guilbaud, B. Lucas, O. Neveu, M. Pittman, D. Ros, M. Richardson, E. Johnson, **Wenzhe Li**, Ph. Balcou, and S. Kazamias, "Hartmann wavefront sensor characterization of a high charge vortex beam in the extreme ultraviolet spectral range," *Opt. Lett.* 43, 2780-2783 (2018)
9. Yuan Li, **Wenzhe Li**, Zeyu Zhang, J. Keith Miller, Ramesh Shori, and Eric G. Johnson, "Concentric vortex beam amplification: experiment and simulation," *Opt. Express*, 24, 1658-1667 (2016)
10. Yuan Li, **Wenzhe Li**, J. Keith Miller, Eric G Johnson, "Multiplexing and Amplification of 2 μm Vortex Beams with a Ho: YAG Rod Amplifier," *IEEE Photonics Technology Letters*, 28(19), 2031-2034(2016)
11. Kaitlyn Morgan, J. Keith Miller, **Wenzhe Li**, Yuan Li, B Cochenour, Eric G. Johnson, "Free Space Propagation of Concentric Vortices through Underwater Turbid Environments," *Journal of Optics*, 18(10), 104004(2016)
12. Joshua Baghdady, J. Keith Miller, Kaitlyn Morgan, Matthew Byrd, Sean Osler, Robert Ragusa, **Wenzhe Li**, Brandon M. Cochenour, and Eric G. Johnson, "Multi-gigabit/s underwater optical communication link using orbital angular momentum multiplexing," *Opt. Express*, 24, 9794-9805 (2016)

Refereed Conference Proceedings

1. Kaitlyn S. Morgan, Yuan Li, **Wenzhe Li**, J. Keith Miller, Richard J. Watkins, and Eric G. Johnson. "Higher Order Bessel Beams Integrated in Time (HOBBIT) for

Underwater Sensing and Metrology." In *CLEO: Applications and Technology*, pp. ATh1K-7. Optical Society of America, 2019.

2. J. Keith Miller, Kaitlyn S. Morgan, **Wenzhe Li**, Yuan Li and Eric G. Johnson, "Data Agile Underwater Optical Communication Link using Flexible Data Formats and Orbital Angular Momentum Multiplexing," In *OCEANS 2018 MTS/IEEE Charleston, Charleston, SC, 2018*, pp. 1-4
3. Kaitlyn S. Morgan, Yuan Li, **Wenzhe Li**, Richard J. Watkins, J. Keith Miller and Eric G. Johnson, "Dynamic beam shaping exploiting orbital angular momentum for underwater structured light illumination," In *OCEANS 2018 MTS/IEEE Charleston, Charleston, SC, 2018*, pp. 1-4
4. Kaitlyn Morgan, Yuan Li, **Wenzhe Li**, J. Keith Miller, Richard J. Watkins and Eric G. Johnson, "Spatial Quadrature Amplitude Multiplexing using Coherently Coupled Beams with Orbital Angular Momentum," In *2018 IEEE Photonics Conference (IPC), Reston, VA, 2018*, pp. 1-2
5. Kaitlyn S. Morgan, Yuan Li, **Wenzhe Li**, J. Keith Miller, and Eric G. Johnson, "Multilevel Phase Shift Keying using coherently coupled beams with Orbital Angular Momentum," In *Imaging and Applied Optics 2018, OSA Technical Digest (Optical Society of America, 2018)*, paper PTu5F.2.
6. Yuan Li, **Wenzhe Li**, J. Keith Miller, Eric G. Johnson, Subhabrata Bera, Craig Nie, and J. A. Harrington, "Amplification of incoherent and coherently coupled higher order modes in a HO:YAG single crystal fiber," In *Conference on Lasers and Electro-Optics, OSA Technical Digest (online) (Optical Society of America, 2018)*, paper SW3M.7.
7. F. Sanson, A. K. Pandey, F. Harms, G. Dovillaire, E. Baynard, J. Demailly, O. Guilbaud, B. Lucas, O. Neveu, E. Papagionnouli, M. Pittman, D. Ros, M. Richardson, E. Johnson, **W. Li**, Ph. Balcou, S. Kazamias. "High-Charge XUV Vortex Beam: Generation and Hartmann Wavefront Sensor Characterization." In *International Conference on X-ray Lasers*, pp. 79-84. Springer, Cham, 2018

8. **Wenzhe Li**, J. Keith Miller, Indumathi R. Srimathi, Yuan Li, Kaitlyn S. Morgan, Eric G. Johnson, "Efficient 1550 nm Diffractive Log-Polar Element Based Orbital Angular Momentum Mode-division Multiplexing," In *Frontiers in Optics 2017, OSA Technical Digest (online) (Optical Society of America, 2017)*, paper JTu2A.37
9. J. Keith. Miller, Kaitlyn S. Morgan, **Wenzhe Li**, Yuan Li, Indumathi R. Srimathi, Joshua Baghdady, Joseph Kelly, Eric G. Johnson, "Underwater Optical Communication Link using Polarization Division Multiplexing and Orbital Angular Momentum Multiplexing," In *OCEANS 2017 - Anchorage, Anchorage, AK, 2017*, pp. 1-4
10. Kaitlyn S. Morgan, J. Keith Miller, **Wenzhe Li**, Yuan Li, Eric G. Johnson, "Higher Order Bessel Beams Integrated in Time (HOBBIT) for Free Space Underwater Sensing and Communication," In *OCEANS 2017 - Anchorage, Anchorage, AK, 2017*, pp. 1-4
11. **Wenzhe Li**, Yuan Li, J. Keith Miller, and Eric G. Johnson, "Multiple Wavelength Concentric Vortex Optics: λ = 1064 nm and 2090 nm", In *OSA Frontiers in Optics*, FF5G.5, 2016
12. Indumathi R. Srimathi, J. Keith Miller, **Wenzhe Li**, Kaitlyn S. Morgan, Joshua Baghdady, and Eric G. Johnson, "Diffractive Orbital Angular Momentum Demultiplexing Elements for Underwater Optical Communications", In *OSA Frontiers in Optics*, FTh4E.2, 2016
13. Joshua Baghdady, J. Keith Miller, Joseph Kelly, Indumathi R. Srimathi, **Wenzhe Li**, Eric G. Johnson, and Kaitlyn S. Morgan, "Underwater Optical Communication Link Using Wavelength Division Multiplexing, Polarization Division Multiplexing and Orbital Angular Momentum Multiplexing", In *OSA Frontiers in Optics*, FTh4E.4, 2016
14. Yuan Li, **Wenzhe Li**, J. Keith Miller, and Eric G. Johnson "Multiplexing and Amplification of 2 μm Vortex Beams", In *OSA Frontiers in Optics*, JTh2A.193, 2016

15. Yuan Li, **Wenzhe Li**, J. Keith Miller, and Eric G. Johnson "Pump Beam Engineering for Vortex Beam in a Ho:YAG Rod Amplifier", In *OSA Lasers Congress, Advanced Solid State Lasers*, AM5A.9, 2016
16. J. Keith Miller, Yuan Li, **Wenzhe Li**, Ramesh Shori, and Eric G. Johnson, "Pulsed Amplification of 2 μm Concentric Vortex Beams", In *OSA CLEO*, STu1M, 2016
17. Alex Sincore, Justin Cook, **Wenzhe Li**, Eric G. Johnson, Josh Bradford, Lawrence Shah, and Martin Richardson, "Beam Propagation of Gaussian and Annular Beams at 2 μm in the Presence of Thermal Lensing", In *OSA CLEO*, JTh2A, 2016
18. Kaitlyn Morgan, J. Keith Miller, **Wenzhe Li**, Yuan Li, B Cochenour, Eric G. Johnson, "Free Space Propagation of Concentric Vortices through Underwater Turbid Environments", In *OSA Propagation Through and Characterization of Atmospheric and Oceanic Phenomena*, W2A.3, 2016
19. Joshua Baghdady, Joseph Kelly, J. Keith Miller, Kaitlyn Morgan, **Wenzhe Li**, and Eric G. Johnson, "Underwater optical communication link using orbital angular momentum space division multiplexing", In *OCEANS 2016 MTS/IEEE Monterey*, 2016
20. Kaitlyn Morgan, J. Keith Miller, **Wenzhe Li**, Joshua Baghdady, and Eric G. Johnson, "Propagation and dynamic manipulation of coherent orbital-angular-momentum modes through underwater turbid environments", In *OCEANS 2016 MTS/IEEE Monterey*, 2016
21. Eric G. Johnson, Joshua Baghdady, Matthew Byrd, **Wenzhe Li**, Kaitlyn Morgan, Aaron Pung, and J. Keith Miller, "Space division multiplexing of blue lasers for undersea communications", In *Photonics Conference (IPC), 2015*, pp. 653-654. IEEE, 2015
22. Yuan Li, Zeyu Zhang, **Wenzhe Li**, J. Keith Miller, and Eric G. Johnson, "Simultaneous Amplification of Multiple 2 μm Vortex Beams," in *Advanced Solid State Lasers, OSA Technical Digest (online) (Optical Society of America, 2015)*, paper ATu2A.45.

23. Yuan Li, Zeyu Zhang, **Wenzhe Li**, J. Keith Miller, and Eric G. Johnson, "Ho:YAG Rod Amplifier For High Order Vortex Modes," In *Frontiers in Optics 2015, OSA Technical Digest (online) (Optical Society of America, 2015)*, paper FTu3G.3.

Non-Refereed Conference Proceedings

1. Eric G. Johnson, J. Keith Miller, Richard J. Watkins, Kaitlyn S. Morgan, **Wenzhe Li**, Kunjian Dai, Caitie O'Donnell, Graham White, "Higher-order Bessel beams integrated with time (HOBBIT) for dynamic structured light control," In *Proc. SPIE 11297, Complex Light and Optical Forces XIV*, 112970T (24 February 2020); https://doi.org/10.1117/12.2551312
2. Eric G. Johnson, J. Keith Miller, Richard J. Watkins, Indumathi R. Srimathi, Joshua Baghdady, **Wenzhe Li**, and Yuan Li, "Creation and exploitation of orbital angular momentum for maritime environments (Conference Presentation)," In *Proc. SPIE 10186, Ocean Sensing and Monitoring IX*, 1018602 (2017)
3. Joshua Baghdady, J. Keith Miller, Sean Osler, Kaitlyn Morgan, **Wenzhe Li**, Eric G. Johnson, and Brandon Cochenour, "Blue-light digital communication in underwater environments utilizing orbital angular momentum," In *SPIE Defense+ Security*, 98270G, 2016
4. Joshua Baghdady, Matthew Byrd, **Wenzhe Li**, Kaitlyn Morgan, Aaron Pung, J. Keith Miller, and Eric G. Johnson, "Spatial multiplexing for blue lasers for undersea communications", In *SPIE Defense+ Security*, 945905, 2015

REFERENCES

1. Allen, Les, Marco W. Beijersbergen, R. J. C. Spreeuw, and J. P. Woerdman. "Orbital angular momentum of light and the transformation of Laguerre-Gaussian laser modes." *Physical review A* 45, no. 11 (1992): 8185.
2. Berry, M. V. "Optical vortices evolving from helicoidal integer and fractional phase steps." *Journal of Optics A: Pure and Applied Optics* 6, no. 2 (2004): 259.
3. Leach, Jonathan, Eric Yao, and Miles J. Padgett. "Observation of the vortex structure of a non-integer vortex beam." *New Journal of Physics* 6, no. 1 (2004): 71.
4. Gbur, Greg. "Fractional vortex Hilbert's hotel." *Optica* 3, no. 3 (2016): 222-225.
5. Wang, Yangyundou, and Greg Gbur. "Hilbert's Hotel in polarization singularities." *Optics letters* 42, no. 24 (2017): 5154-5157.
6. Alexeyev, C. N., Yu A. Egorov, and A. V. Volyar. "Mutual transformations of fractional-order and integer-order optical vortices." *Physical Review A* 96, no. 6 (2017): 063807.
7. Berger, Bernd, Marius Kahlert, Daniel Schmidt, and Marc Assmann. "Spectroscopy of fractional orbital angular momentum states." *Optics Express* 26, no. 24 (2018): 32248-32258.
8. Li, Wenzhe, Kaitlyn S. Morgan, Yuan Li, J. Keith Miller, Graham White, Richard J. Watkins, and Eric G. Johnson. "Rapidly tunable orbital angular momentum (OAM) system for higher order Bessel beams integrated in time (HOBBIT)." *Optics Express* 27, no. 4 (2019): 3920-3934.
9. Pitchumani, Mahesh. "Additive lithography fabrication and integration of micro optics." (2006).
10. Raghu Srimathi, Indumathi. "Metaoptics for Spectral and Spatial Beam Manipulation." (2017).
11. Morgan, Kaitlyn S. "A Study on the Dynamic Manipulation of Structured Light Using Orbital Angular Momentum for Wireless Underwater Links." (2020).

12. Bryngdahl, Olof. "Geometrical transformations in optics." *JOSA* 64, no. 8 (1974): 1092-1099.
13. Bryngdahl, Olof. "Optical map transformations." *Optics Communications* 10, no. 2 (1974): 164-168.
14. Casasent, David, Shao-Feng Xia, Andrew J. Lee, and Jian-Zhong Song. "Real-time deformation invariant optical pattern recognition using coordinate transformations." *Applied optics* 26, no. 5 (1987): 938-942.
15. Saito, Yoshiharu, Shin-ichi Komatsu, and Hitoshi Ohzu. "Scale and rotation invariant real time optical correlator using computer generated hologram." *Optics Communications* 47, no. 1 (1983): 8-11.
16. Berkhout, Gregorius CG, Martin PJ Lavery, Johannes Courtial, Marco W. Beijersbergen, and Miles J. Padgett. "Efficient sorting of orbital angular momentum states of light." *Physical review letters* 105, no. 15 (2010): 153601.
17. Mirhosseini, Mohammad, Mehul Malik, Zhimin Shi, and Robert W. Boyd. "Efficient separation of the orbital angular momentum eigenstates of light." *Nature communications* 4, no. 1 (2013): 1-6.
18. Wan, Chenhao, Jian Chen, and Qiwen Zhan. "Compact and high-resolution optical orbital angular momentum sorter." *APL Photonics* 2, no. 3 (2017): 031302.
19. Ruffato, Gianluca, Michele Massari, and Filippo Romanato. "Compact sorting of optical vortices by means of diffractive transformation optics." *Optics Letters* 42, no. 3 (2017): 551-554.
20. Ruffato, Gianluca, Michele Massari, Giuseppe Parisi, and Filippo Romanato. "Test of mode-division multiplexing and demultiplexing in free-space with diffractive transformation optics." *Optics express* 25, no. 7 (2017): 7859-7868.
21. Ruffato, Gianluca, Michele Massari, and Filippo Romanato. "Multiplication and division of the orbital angular momentum of light with diffractive transformation optics." *Light: Science & Applications* 8, no. 1 (2019): 1-13.
22. Ruffato, Gianluca, Michele Massari, Marcello Girardi, Giuseppe Parisi, Mauro Zontini, and Filippo Romanato. "Non-paraxial design and fabrication of a compact

OAM sorter in the telecom infrared." *Optics Express* 27, no. 17 (2019): 24123-24134.

23. Kotlyar, V. V., A. A. Kovalev, R. V. Skidanov, and V. A. Soifer. "Asymmetric Bessel–Gauss beams." *JOSA A* 31, no. 9 (2014): 1977-1983.
24. Götte, Jörg B., Sonja Franke-Arnold, Roberta Zambrini, and Stephen M. Barnett. "Quantum formulation of fractional orbital angular momentum." *Journal of Modern Optics* 54, no. 12 (2007): 1723-1738.
25. Kotlyar, Victor V., Alexey A. Kovalev, and Alexey P. Porfirev. "Calculation of fractional orbital angular momentum of superpositions of optical vortices by intensity moments." *Optics express* 27, no. 8 (2019): 11236-11251.
26. Rego, Laura, Kevin M. Dorney, Nathan J. Brooks, Quynh L. Nguyen, Chen-Ting Liao, Julio San Román, David E. Couch et al. "Generation of extreme-ultraviolet beams with time-varying orbital angular momentum." *Science* 364, no. 6447 (2019): eaaw9486.
27. Sedeh, Hooman Barati, Mohammad Mahdi Salary, and Hossein Mosallaei. "Time-varying optical vortices enabled by time-modulated metasurfaces." *Nanophotonics* 1, no. ahead-of-print (2020).
28. Yao, Alison M., and Miles J. Padgett. "Orbital angular momentum: origins, behavior and applications." *Advances in Optics and Photonics* 3, no. 2 (2011): 161-204.
29. McLaren, Melanie, Thandeka Mhlanga, Miles J. Padgett, Filippus S. Roux, and Andrew Forbes. "Self-healing of quantum entanglement after an obstruction." *Nature communications* 5, no. 1 (2014): 1-8.
30. Litvin, Igor A., Liesl Burger, and Andrew Forbes. "Angular self-reconstruction of petal-like beams." *Optics Letters* 38, no. 17 (2013): 3363-3365.
31. A. S. Desyatnikov, Y. S. Kivshar, and L. Torner, “Optical vortices and vortex solitons,” *Prog. Opt*. 47, (2005): 291-391.

32. Lee, W. M., X-C. Yuan, and W. C. Cheong. "Optical vortex beam shaping by use of highly efficient irregular spiral phase plates for optical micromanipulation." *Optics letters* 29, no. 15 (2004): 1796-1798.
33. Huang, Hao, Giovanni Milione, Martin PJ Lavery, Guodong Xie, Yongxiong Ren, Yinwen Cao, Nisar Ahmed et al. "Mode division multiplexing using an orbital angular momentum mode sorter and MIMO-DSP over a graded-index few-mode optical fibre." *Scientific reports* 5, no. 1 (2015): 1-7.
34. Baghdady, Joshua, Keith Miller, Kaitlyn Morgan, Matthew Byrd, Sean Osler, Robert Ragusa, Wenzhe Li, Brandon M. Cochenour, and Eric G. Johnson. "Multi-gigabit/s underwater optical communication link using orbital angular momentum multiplexing." *Optics express* 24, no. 9 (2016): 9794-9805.
35. Vijayakumar, A., C. Rosales-Guzmán, M. R. Rai, J. Rosen, O. V. Minin, I. V. Minin, and A. Forbes. "Generation of structured light by multilevel orbital angular momentum holograms." *Optics Express* 27, no. 5 (2019): 6459-6470.
36. Barbieri, Nicholas, Zahra Hosseinimakarem, Khan Lim, Magali Durand, Matthieu Baudelet, Eric Johnson, and Martin Richardson. "Helical filaments." *Applied Physics Letters* 104, no. 26 (2014): 261109.
37. Barbieri, Nicholas, Matthew Weidman, Gregory Katona, Matthieu Baudelet, Zachary Roth, Eric Johnson, Georgios Siviloglou, Demetrios Christodoulides, and Martin Richardson. "Double helical laser beams based on interfering first-order Bessel beams." *JOSA A* 28, no. 7 (2011): 1462-1469.
38. Fisher, Matthew, Craig Siders, Eric Johnson, Oleksiy Andrusyak, Christopher Brown, and Martin Richardson. "Control of filamentation for enhancing remote detection with laser induced breakdown spectroscopy." In *Enabling Technologies and Design of Nonlethal Weapons*, vol. 6219, p. 621907. International Society for Optics and Photonics, 2006.
39. Morgan, K. S., J. K. Miller, B. M. Cochenour, W. Li, Y. Li, R. J. Watkins, and E. G. Johnson. "Free space propagation of concentric vortices through underwater turbid environments." *Journal of Optics* 18, no. 10 (2016): 104004.

40. Li, Yuan, Wenzhe Li, Zeyu Zhang, Keith Miller, Ramesh Shori, and Eric G. Johnson. "Concentric vortex beam amplification: experiment and simulation." *Optics Express* 24, no. 2 (2016): 1658-1667.
41. Faklis, Dean, and G. Michael Morris. "Spectral properties of multiorder diffractive lenses." *Applied Optics* 34, no. 14 (1995): 2462-2468.
42. Goodman, Joseph W. Introduction to Fourier optics. Roberts and Company Publishers, 2005.
43. Johnson, Eric G., Jared Stack, and Charles Koehler. "Light coupling by a vortex lens intograded index fiber." *Journal of Lightwave Technology* 19, no. 5 (2001): 753.
44. Kotlyar, Victor V., and Alexey A. Kovalev. "Family of hypergeometric laser beams." *JOSA A* 25, no. 1 (2008): 262-270.
45. Kotlyar, Victor V., Alexey A. Kovalev, and Eugeny G. Abramochkin. "Kummer laser beams with a transverse complex shift." *Journal of Optics* 22, no. 1 (2019): 015606.
46. Garcia-Gracia, Hipolito, and Julio C. Gutiérrez-Vega. "Diffraction of plane waves by finite-radius spiral phase plates of integer and fractional topological charge." *JOSA A* 26, no. 4 (2009): 794-803.
47. Kotlyar, Victor V., Alexey A. Kovalev, Roman V. Skidanov, Oleg Yu Moiseev, and Victor A. Soifer. "Diffraction of a finite-radius plane wave and a Gaussian beam by a helical axicon and a spiral phase plate." *JOSA A* 24, no. 7 (2007): 1955-1964.
48. Duan, Kailiang, and Baida Lü. "Nonparaxial analysis of far-field properties of Gaussian beams diffracted at a circular aperture." *Optics Express* 11, no. 13 (2003): 1474-1480.
49. Cui, Xianghan, Chaolin Wang, and Xinting Jia. "Nonparaxial propagation of vector vortex beams diffracted by a circular aperture." *JOSA A* 36, no. 1 (2019): 115-123.
50. Baddour, Natalie. "Operational and convolution properties of two-dimensional Fourier transforms in polar coordinates." *JOSA A* 26, no. 8 (2009): 1767-1777.

51. Gradshteyn, Izrail Solomonovich, and Iosif Moiseevich Ryzhik. *Table of integrals, series, and products*. Academic press, 2014.

52. Baumann, S. M., D. M. Kalb, L. H. MacMillan, and E. J. Galvez. "Propagation dynamics of optical vortices due to Gouy phase." *Optics Express* 17, no. 12 (2009): 9818-9827.

53. Gutiérrez-Vega, Julio C., and Carlos López-Mariscal. "Nondiffracting vortex beams with continuous orbital angular momentum order dependence." *Journal of Optics A: Pure and Applied Optics* 10, no. 1 (2007): 015009.

54. Huang, Kun, Hong Liu, Sara Restuccia, Muhammad Q. Mehmood, Sheng-Tao Mei, Daniel Giovannini, Aaron Danner, Miles J. Padgett, Jing-Hua Teng, and Cheng-Wei Qiu. "Spiniform phase-encoded metagratings entangling arbitrary rational-order orbital angular momentum." *Light: Science & Applications* 7, no. 3 (2018): 17156-17156.

55. Yang, Zhenshan, Xia Zhang, Chenglin Bai, and Minghong Wang. "Nondiffracting light beams carrying fractional orbital angular momentum." *JOSA A* 35, no. 3 (2018): 452-461.

56. Watkins, Richard J., Kunjian Dai, Graham White, Wenzhe Li, J. Keith Miller, Kaitlyn S. Morgan, and Eric G. Johnson. "Experimental probing of turbulence using a continuous spectrum of asymmetric OAM beams." *Optics Express* 28, no. 2 (2020): 924-935.

57. Götte, Jörg B., Kevin O'Holleran, Daryl Preece, Florian Flossmann, Sonja Franke-Arnold, Stephen M. Barnett, and Miles J. Padgett. "Light beams with fractional orbital angular momentum and their vortex structure." *Optics express* 16, no. 2 (2008): 993-1006.

58. Oemrawsingh, S. S. R., X. Ma, D. Voigt, A. Aiello, ER T. Eliel, and J. P. Woerdman. "Experimental demonstration of fractional orbital angular momentum entanglement of two photons." *Physical review letters* 95, no. 24 (2005): 240501.

59. Gbur, Greg, and Robert K. Tyson. "Vortex beam propagation through atmospheric turbulence and topological charge conservation." *JOSA A* 25, no. 1 (2008): 225-230.

60. Zeng, Jun, Xianlong Liu, Fei Wang, Chengliang Zhao, and Yangjian Cai. "Partially coherent fractional vortex beam." *Optics express* 26, no. 21 (2018): 26830-26844.

61. Fang, Yiqi, Qinghong Lu, Xiaolei Wang, Wuhong Zhang, and Lixiang Chen. "Fractional-topological-charge-induced vortex birth and splitting of light fields on the submicron scale." *Physical Review A* 95, no. 2 (2017): 023821.

62. Mair, Alois, Alipasha Vaziri, Gregor Weihs, and Anton Zeilinger. "Entanglement of the orbital angular momentum states of photons." *Nature* 412, no. 6844 (2001): 313-316.

63. Vaziri, Alipasha, Gregor Weihs, and Anton Zeilinger. "Superpositions of the orbital angular momentum for applications in quantum experiments." *Journal of Optics B: Quantum and Semiclassical Optics* 4, no. 2 (2002): S47.

64. Lee, W. M., X-C. Yuan, and K. Dholakia. "Experimental observation of optical vortex evolution in a Gaussian beam with an embedded fractional phase step." *Optics Communications* 239, no. 1-3 (2004): 129-135.

65. Kotlyar, V. V., A. A. Kovalev, and V. A. Soifer. "Asymmetric Bessel modes." *Optics Letters* 39, no. 8 (2014): 2395-2398.

66. Kotlyar, V. V., A. A. Kovalev, and A. P. Porfirev. "Orbital angular momentum of Gaussian optical vortices with displaced point of phase singularity." *JPhCS* 1096, no. 1 (2018): 012119.

67. Kotlyar, V. V., S. N. Khonina, A. A. Kovalev, V. A. Soifer, H. Elfstrom, and J. Turunen. "Diffraction of a plane, finite-radius wave by a spiral phase plate." *Optics letters* 31, no. 11 (2006): 1597-1599.

68. Kotlyar, Victor V., Anton A. Almazov, Svetlana N. Khonina, Victor A. Soifer, Henna Elfstrom, and Jari Turunen. "Generation of phase singularity through diffracting a plane or Gaussian beam by a spiral phase plate." *JOSA A* 22, no. 5 (2005): 849-861.

69. Ruffato, G., M. Massari, and F. Romanato. "Generation of high-order Laguerre–Gaussian modes by means of spiral phase plates." *Optics letters* 39, no. 17 (2014): 5094-5097.

70. Karimi, Ebrahim, Gianluigi Zito, Bruno Piccirillo, Lorenzo Marrucci, and Enrico Santamato. "Hypergeometric-gaussian modes." *Optics letters* 32, no. 21 (2007): 3053-3055.

71. Dudley, Angela, Igor A. Litvin, and Andrew Forbes. "Quantitative measurement of the orbital angular momentum density of light." *Applied optics* 51, no. 7 (2012): 823-833.

72. Alperin, Samuel N., Robert D. Niederriter, Juliet T. Gopinath, and Mark E. Siemens. "Quantitative measurement of the orbital angular momentum of light with a single, stationary lens." *Optics letters* 41, no. 21 (2016): 5019-5022.

73. Litvin, Igor A., Angela Dudley, and Andrew Forbes. "Poynting vector and orbital angular momentum density of superpositions of Bessel beams." *Optics Express* 19, no. 18 (2011): 16760-16771.

74. Dai, Kunjian, Wenzhe Li, Kaitlyn S. Morgan, Yuan Li, J. Keith Miller, Richard J. Watkins, and Eric G. Johnson. "Second-harmonic generation of asymmetric Bessel-Gaussian beams carrying orbital angular momentum." *Optics Express* 28, no. 2 (2020): 2536-2546.

75. Jack, B., M. J. Padgett, and S. Franke-Arnold. "Angular diffraction." *New Journal of Physics* 10, no. 10 (2008): 103013.

76. Yao, Eric, Sonja Franke-Arnold, Johannes Courtial, Stephen Barnett, and Miles Padgett. "Fourier relationship between angular position and optical orbital angular momentum." *Optics Express* 14, no. 20 (2006): 9071-9076.

77. Jha, A. K., B. Jack, E. Yao, J. Leach, R. W. Boyd, G. S. Buller, S. M. Barnett, S. Franke-Arnold, and M. J. Padgett. "Fourier relationship between the angle and angular momentum of entangled photons." *Physical Review A* 78, no. 4 (2008): 043810.

78. Franke-Arnold, Sonja, Stephen M. Barnett, Eric Yao, Jonathan Leach, Johannes Courtial, and Miles Padgett. "Uncertainty principle for angular position and angular momentum." *New Journal of Physics* 6, no. 1 (2004): 103.

79. Pinnell, Jonathan, Valeria Rodríguez-Fajardo, and Andrew Forbes. "How perfect are perfect vortex beams?" *Optics letters* 44, no. 22 (2019): 5614-5617.

80. Vaity, Pravin, and Leslie Rusch. "Perfect vortex beam: Fourier transformation of a Bessel beam." *Optics letters* 40, no. 4 (2015): 597-600.

81. Fontaine, Nicolas K., Roland Ryf, Haoshuo Chen, David T. Neilson, Kwangwoong Kim, and Joel Carpenter. "Laguerre-Gaussian mode sorter." *Nature communications* 10, no. 1 (2019): 1-7.

82. Krackhardt, Ulrich, Joseph N. Mait, and Norbert Streibl. "Upper bound on the diffraction efficiency of phase-only fanout elements." *Applied optics* 31, no. 1 (1992): 27-37.

83. Wen, Yuanhui, Ioannis Chremmos, Yujie Chen, Jiangbo Zhu, Yanfeng Zhang, and Siyuan Yu. "Spiral transformation for high-resolution and efficient sorting of optical vortex modes." *Physical review letters* 120, no. 19 (2018): 193904.

84. Hossack, W. J., A. M. Darling, and A. Dahdouh. "Coordinate transformations with multiple computer-generated optical elements." *Journal of Modern Optics* 34, no. 9 (1987): 1235-1250.

85. Stuff, M. A., and J. N. Cederquist. "Coordinate transformations realizable with multiple holographic optical elements." *JOSA A* 7, no. 6 (1990): 977-981.

86. Takashima, Satoru, Hirokazu Kobayashi, and Katsushi Iwashita. "Integer multiplier for the orbital angular momentum of light using a circular-sector transformation." *Physical Review A* 100, no. 6 (2019): 063822.

87. Wen, Yuanhui, Ioannis Chremmos, Yujie Chen, Yanfeng Zhang, and Siyuan Yu. "Arbitrary Multiplication and Division of the Orbital Angular Momentum of Light." *Physical Review Letters* 124, no. 21 (2020): 213901.

88. Ruffato, Gianluca, Marcello Girardi, Michele Massari, Erfan Mafakheri, Bereneice Sephton, Pietro Capaldo, Andrew Forbes, and Filippo Romanato. "A compact

diffractive sorter for high-resolution demultiplexing of orbital angular momentum beams." *Scientific reports* 8, no. 1 (2018): 1-12.

89. Malik, Muhammad Nouman, Ning Zhang, Veronica Toccafondo, Charalambos Klitis, Martin Lavery, Andrea Sgambelluri, Jiangbo Zhu et al. "Tunable Orbital Angular Momentum Converter Based on Integrated Multiplexers." *Journal of Lightwave Technology* (2020).
90. Morizur, Jean-François, Lachlan Nicholls, Pu Jian, Seiji Armstrong, Nicolas Treps, Boris Hage, Magnus Hsu, Warwick Bowen, Jiri Janousek, and Hans-A. Bachor. "Programmable unitary spatial mode manipulation." *JOSA A* 27, no. 11 (2010): 2524-2531.
91. Labroille, Guillaume, Bertrand Denolle, Pu Jian, Philippe Genevaux, Nicolas Treps, and Jean-François Morizur. "Efficient and mode selective spatial mode multiplexer based on multi-plane light conversion." *Optics express* 22, no. 13 (2014): 15599-15607.
92. Xiao, Xingguo, Yan Li, Donghao Zheng, Xinglin Zeng, Wei Li, and Jian Wu. "Programmable orbital angular momentum (OAM) mode multiplexer based on multi-plane light conversion (MPLC)." In *2018 Asia Communications and Photonics Conference (ACP)*, pp. 1-3. IEEE, 2018.
93. Durnin, J. J. J. M., J. J. Miceli Jr, and J. H. Eberly. "Diffraction-free beams." *Physical review letters* 58, no. 15 (1987): 1499.
94. Chagnon, Mathieu, Mohamed Osman, Qunbi Zhuge, Xian Xu, and David V. Plant. "Analysis and experimental demonstration of novel 8PolSK-QPSK modulation at 5 bits/symbol for passive mitigation of nonlinear impairments." *Optics express* 21, no. 25 (2013): 30204-30220.
95. Willner, Asher J., Yongxiong Ren, Guodong Xie, Zhe Zhao, Yinwen Cao, Long Li, Nisar Ahmed et al. "Experimental demonstration of 20 Gbit/s data encoding and 2 ns channel hopping using orbital angular momentum modes." *Optics Letters* 40, no. 24 (2015): 5810-5813.

96. Du, Jing, and Jian Wang. "High-dimensional structured light coding/decoding for free-space optical communications free of obstructions." *Optics Letters* 40, no. 21 (2015): 4827-4830.

97. Lei, Ting, Shecheng Gao, Zhaohui Li, Yangsheng Yuan, Yangjin Li, Meng Zhang, Gordon Ning Liu, Xiaogeng Xu, Jindong Tian, and Xiaocong Yuan. "Fast-switchable OAM-based high capacity density optical router." *IEEE Photonics Journal* 9, no. 1 (2017): 1-9.

98. Radwell, N., D. Brickus, T. W. Clark, and S. Franke-Arnold. "High speed switching between arbitrary spatial light profiles." *Optics express* 22, no. 11 (2014): 12845-12852.

99. Malik, Mehul, Malcolm O'Sullivan, Brandon Rodenburg, Mohammad Mirhosseini, Jonathan Leach, Martin PJ Lavery, Miles J. Padgett, and Robert W. Boyd. "Influence of atmospheric turbulence on optical communications using orbital angular momentum for encoding." *Optics express* 20, no. 12 (2012): 13195-13200.

100. Krenn, Mario, Robert Fickler, Matthias Fink, Johannes Handsteiner, Mehul Malik, Thomas Scheidl, Rupert Ursin, and Anton Zeilinger. "Communication with spatially modulated light through turbulent air across Vienna." *New Journal of Physics* 16, no. 11 (2014): 113028.

101. Ma, Cheng, Xiao Xu, Yan Liu, and Lihong V. Wang. "Time-reversed adapted-perturbation (TRAP) optical focusing onto dynamic objects inside scattering media." *Nature photonics* 8, no. 12 (2014): 931-936.

102. Xie, Ting, HuiHui Wang, Fei Yuan, Shengqian Chang, Peng Sun, Siman Zhang, Huaye Li, Siqi Liu, Chang Wang, and Zhenrong Zheng. "Arbitrary manipulation of micro-particles in three dimensions by steering of multiple orbital angular momentum modes." In *Optical Trapping and Optical Micromanipulation XIV*, vol. 10347, p. 103470Y. International Society for Optics and Photonics, 2017.

103. Lavery, Martin PJ, Fiona C. Speirits, Stephen M. Barnett, and Miles J. Padgett. "Detection of a spinning object using light's orbital angular momentum." *Science* 341, no. 6145 (2013): 537-540.

104. Lavery, Martin PJ, Stephen M. Barnett, Fiona C. Speirits, and Miles J. Padgett. "Observation of the rotational Doppler shift of a white-light, orbital-angular-momentum-carrying beam backscattered from a rotating body." *Optica* 1, no. 1 (2014): 1-4.

105. Zhou, Zhi-Yuan, Yan Li, Dong-Sheng Ding, Wei Zhang, Shuai Shi, and Bao-Sen Shi. "Optical vortex beam based optical fan for high-precision optical measurements and optical switching." *Optics letters* 39, no. 17 (2014): 5098-5101.

106. Cvijetic, Neda, Giovanni Milione, Ezra Ip, and Ting Wang. "Detecting lateral motion using light's orbital angular momentum." *Scientific reports* 5 (2015): 15422.

107. Strain, Michael J., Xinlun Cai, Jianwei Wang, Jiangbo Zhu, David B. Phillips, Lifeng Chen, Martin Lopez-Garcia et al. "Fast electrical switching of orbital angular momentum modes using ultra-compact integrated vortex emitters." *Nature communications* 5, no. 1 (2014): 1-7.

108. Cederquist, Jack, and Anthony M. Tai. "Computer-generated holograms for geometric transformations." *Applied optics* 23, no. 18 (1984): 3099-3104.

109. Mhlanga, T., A. Dudley, A. Mcdonald, F. S. Roux, M. Lavery, M. Padgett, and A. Forbes. "Efficient sorting of Bessel beams." In *Complex Light and Optical Forces VII*, vol. 8637, p. 86371C. International Society for Optics and Photonics, 2013.

110. Srimathi, Indumathi Raghu, Keith Miller, Wenzhe Li, Kaitlyn S. Morgan, Joshua Baghdady, and Eric G. Johnson. "Diffractive Orbital Angular Momentum Demultiplexing Elements for Underwater Optical Communications." In *Frontiers in Optics*, pp. FTh4E-2. Optical Society of America, 2016.

111. Li, Wenzhe, Keith Miller, Indumathi Raghu Srimathi, Yuan Li, Kaitlyn S. Morgan, and Eric G. Johnson. "Efficient 1550 nm Diffractive Log-Polar Element Based

Orbital Angular Momentum Mode-division Multiplexing." In *Laser Science*, pp. JTu2A-37. Optical Society of America, 2017.

112. Lightman, Shlomi, Gilad Hurvitz, Raz Gvishi, and Ady Arie. "Miniature wide-spectrum mode sorter for vortex beams produced by 3D laser printing." *Optica* 4, no. 6 (2017): 605-610.
113. Morgan, Kaitlyn S., Indumathi S. Raghu, and Eric G. Johnson. "Design and fabrication of diffractive optics for orbital angular momentum space division multiplexing." In *Advanced Fabrication Technologies for Micro/Nano Optics and Photonics VIII*, vol. 9374, p. 93740Y. International Society for Optics and Photonics, 2015.
114. Ruffato, G., M. Girardi, M. Massari, E. Mafakheri, P. Capaldo, and F. Romanato. "Compact diffractive optics for high-resolution sorting of orbital angular momentum beams." In *Laser Beam Shaping XVIII*, vol. 10744, p. 107440L. International Society for Optics and Photonics, 2018.
115. Akemann, Walther, Jean-François Léger, Cathie Ventalon, Benjamin Mathieu, Stéphane Dieudonné, and Laurent Bourdieu. "Fast spatial beam shaping by acousto-optic diffraction for 3D non-linear microscopy." *Optics express* 23, no. 22 (2015): 28191-28205.
116. Grinenko, A., M. P. MacDonald, C. R. P. Courtney, P. D. Wilcox, C. E. M. Demore, S. Cochran, and B. W. Drinkwater. "Tunable beam shaping with a phased array acousto-optic modulator." *Optics Express* 23, no. 1 (2015): 26-32.
117. Szulzycki, Krzysztof, Viktoriya Savaryn, and Ireneusz Grulkowski. "Generation of dynamic Bessel beams and dynamic bottle beams using acousto-optic effect." *Optics express* 24, no. 21 (2016): 23977-23991.
118. Barcelo-Chong, Arturo, Brian Estrada-Portillo, Arturo Canales-Benavides, and Servando Lopez-Aguayo. "Asymmetric Mathieu beams." *Chinese Optics Letters* 16, no. 12 (2018): 122601.

119. Ruffato, Gianluca, Michele Massari, and Filippo Romanato. "Diffractive optics for combined spatial-and mode-division demultiplexing of optical vortices: design, fabrication and optical characterization." *Scientific reports* 6 (2016): 24760.

120. Alperin, Samuel N., and Mark E. Siemens. "Angular momentum of topologically structured darkness." *Physical Review Letters* 119, no. 20 (2017): 203902.